ORGANO FUNCTIONALIZED MESOPOROUS MATERIALS: SYNTHESIS, CHARACTERIZATION AND CATALYTIC APPLICATION FOR FINE CHEMICAL SYNTHESES

A THESIS SUBMITTED TO THE

UNIVERSITY OF PUNE FOR THE DEGREE OF

DOCTOR OF PHILOSOPHY

IN CHEMISTRY

BY

S. SELVAKUMAR

UNDER THE GUIDANCE OF

Dr. A.P. SINGH

CATALYSIS DIVISION

NATIONAL CHEMICAL LABORATORY

PUNE 411008, INDIA

APRIL 2010

CERTIFICATE

Certified that the work incorporated in the thesis entitled: **"Organo Functionalized Mesoporous Materials: Synthesis, Characterization and Catalytic Application for Fine Chemical Syntheses ",** submitted by **Mr. S. Selvakumar,** for the Degree of ***Doctor of Philosophy*****,** was carried out by the candidate under my supervision at Catalysis Division, National Chemical Laboratory, Pune 411 008, India. Material that has been obtained from other sources is duly acknowledged in the thesis.

Date: **Dr. Anand Pal Singh**

Place: **(Research Supervisor)**

DECLARATION BY THE CANDIDATE

I hereby declare that the thesis entitled **"Organo Functionalized Mesoporous Materials: Synthesis, Characterization and Catalytic Application for Fine Chemical Syntheses"**, submitted for the Degree of ***Doctor of Philosophy*** to the University of Pune, has been carried out by me during the period from August 2004 to till date at Catalysis Division, National Chemical Laboratory, Pune 411008, India, under the supervision of Dr. A.P. Singh. The work is original and has not been submitted in part or full by me for any other degree or diploma to this or any other University.

Date: **S. Selvakumar**

Place:

Dedicated

to my

Parents, Brother, Sisters

ACKNOWLEDGEMENTS

It gives me immense pleasure to express my deep sense of gratitude to my research guide Dr. A.P. Singh, who has helped me a lot to learn and think more about chemistry. I thank him for an excellent and inspiring guidance, constant encouragement, sincere advice and unstinted support during all the times of my Ph.D. work.

I would like to sincerely thank Dr. N .M. Gupta for helping me in the last phase of my thesis by providing friendly discussions and suggestions and would also my earnest respect to Dr. Mrs. K. R. Kamble, Dr. B.L.V. Prasad, Dr. C.S. Gopinath and Dr. P. N. Joshi for their valuable support during my course of study.

I wish to convey my sincere gratitude to Dr. S.B. Halligudi for FT-IR analysis, Dr. Veda ramasamy, Dr. Selvaraj, Dr. Nandhini Devi for low angle XRD, Dr. T. Raja for TPD analysis, Dr. Shubhangi, Dr. Dongare for FT-IR, all the NMR group members for solid and liquid state NMR analysis, Dr. N.E. Jacob and Mr. R.K. Jha for N_2-sorption analysis, Ms. V. Samuel for XRD, Dr. (Mrs.) S.S. Deshpande for UV-Vis, Dr. Sainkar, Dr. Patil of CMC and Dr. A.A. Bhalekhar, Mr. Gaikwad for SEM analysis, Micro analysis laboratory staffs for elemental analysis, divisional scientists Dr. C.V.V Satyanarayana, Dr. D. Srinivas and Mr. Marimuthu from CMET. I would also like to thank Mr. Purushottaman, Mr. Madhu, Mr. Milind and all other scientific and nonscientific staff of the division for their valuable help and cooperation during my tenure as a research student.

I don't have words to express my feelings towards my friends and seniors Dr. M. Chidambaram, Dr. Thirumoorthy, Dr. Pradeep Kumar, Mr. Khaja Mohaideen Dr. Balakrishnan, Dr. C. Venkatesan, and Dr. P.S. Vijayakumar without their invariable help and regular scientific discussions; it would have not been possible for me to submit this thesis.

With much appreciation, I would like to mention the crucial role of my lab mates and friends Dr. Shylesh, Dr. Surendran, Dr. Srikant, Shital, Sheetal, Prinson, Rejeesh, Balke, Aneesh, Shoy, Priti, Sanjay, Rentona, Priyanka, Mahesh, Atul, Ramakanta, Pranjal, Anupam, Maithri, Rajeesh, Jijil, Deepa, Sumona, Mangesh Mahajan, Pankaj Thakuria, Hanmant Gurav, Dr. Amit Dubey, Dr. Prakash Prabhu, Dr. P.R. Selvakannan, Dr. Malli, Rama, Sreeja, R. Kannan, Dr. Prathap, Dr. Thirunavukarasu, Dr. Sankar, V. Nagaraj, S. Nagaraj, Vijayanand, Venky, Dharma, Mohan, Palani, Edwin, Lenin, Siva ranjani, Thussara, Senthil, Suresh, Sridhar Krishna, Palanichamy, and all other research scholars from catalysis division for such a friendly and cheerful working atmosphere, for their constant support, love and care throughout my stay in NCL.

I take this opportunity to acknowledge my college teachers Dr. A. Thamarai Selvan, Dr. A. Elangovan, Mr. K. Sethuraman, Mr. S. Narayanan and Mr. V. Subramanian who directed me in a proper way and taught me the value of education.

I am forever indebted to my parents, brother and sisters for their love, understanding and encouragement throughout my life. Their blessings and encouragement have always made me to take proper decision in all difficult periods.

Finally, my thanks are due to Council of Scientific and Industrial Research, Government of India, for awarding the senior research fellowships and Dr. S. Sivaram, Director, Dr. B. D. Kulkarni, Deputy Director, Dr. Sourav Pal, Dr. Pedireddy, Dr. P.A. Joy and all the Students Academic Committee (SAC) staffs, National Chemical Laboratory to carry out my research works, extending all infrastructural facilities and to submit this work in the form of a thesis for the award of Ph. D degree.

S. Selvakumar

CONTENTS

DESCRIPTION

CHAPTER 1. INTRODUCTION AND LITERATURE SURVEY

CHAPTER 4. METAL TRIFLATES IMMOBILIZED MESOPOROUS SBA-15 CATALYSTS

CHAPTER 5. BENZYLSULFONIC ACID FUNCTIONALIZED Zr-TMS CATALYSTS (Zr-TMS-BSA)

LIST OF FIGURES

LIST OF TABLES

LIST OF SCHEMES

LIST OF ABBREVIATIONS

AAS	Atomic Absorption Spectroscopy
AES	Atomic Emission Spectroscopy
APTS	3-Aminopropyltrimethoxy silane
CP MAS	Cross Polarization Magic Angle Spinning
BET	Brunauer-Emmett-Teller
BJH	Barrett-Joyner-Halenda
BTSE	1,2-Bis(triethoxysilyl)ethane
CMC	Critical Micelle Concentration
BE	Binding Energy
CTABr	Cetyltrimethylammonium bromide
DCM	Dichloromethane
SDPEN	(S,S)-DPEN or (S,S)-1,2-Diphenylethylenediamine
DNA	Deoxyribonucleic acid
DPEN	1,2-Diphenylethylenediamine
DTA	Differential Thermal Analysis
ee	enantiomeric Excess
EN	Ethylenediamine
FSM	Folded Sheet Materials
FTIR	Fourier Transform Infrared
GC	Gas Chromatography
GCMS	Gas Chromatography – Mass Spectroscopy
KCP	Kinetically Controlled Product
LCT	Liquid Crystal Template
MCM	Mobil's Crystalline Material
MPTS	3-Mercaptopropyltrimethoxy Silane
NMR	Nuclear Magnetic Resonance
ODA	Octadecylamine
PMO	Periodic Mesoporous Organosilica
SAED	Selected Area Electron Diffraction
SAMS	Self-Assembled Monolayers
SBA	Santa Barbara Amorphous
DDA	Dodecylamine
SEM	Scanning Electron Microscopy
SLC	Silicatropic Liquid Crystals
TCP	Thermodynamically Controlled Product
TEOS	Tetraethyl orthosilicate
TGA	Thermogravimetric Analysis
THF	Tetrahydrofuran
TOF	Turnover Frequency
TON	Turnover Number
TPD	Temperature Programmed Desorption
TPEN	N-[3-(trimethoxysilyl)propyl]-ethylenediamine

GHSV	Gram Hourly Space Velocity	UOF MN	Unified Organically Functionalized Mesoporous Network
HMM	Hybrid Mesoporous Material	UV-Vis	Ultraviolet-Visible
HMS	Hexagonal Mesoporous Silica	XPS	X-Ray Photoelectron Spectroscopy
HRTEM	High Resolution Transmission Electron Microscopy	XRD	X-Ray Diffraction
ICP-AES	Inductively Coupled Plasma – Atomic Emission Spectrometry	XRF	X-Ray Fluorescence

ABSTRACT

The present work aims at the design and development of siliceous as well as non siliceous mesoporous molecular sieves using fumed silica or TEOS as a siliceous source and zirconium tetra butoxide as a non-siliceous source by adopting suitable templating route to get high surface area with narrow pore size distribution. Further, the surface modification of the synthesized mesoporous materials were done by using various organic and organo silane groups, such as 3-chloro propyl trimethoxy silane, BISPICEN type chiral metal complexes, various metal triflates and benzyl sulfonic acid (BSA) by post synthetic route to develop new class of mesoporous catalysts for oxidation, acylation and condensation reactions.

The present work is comprised of **six chapters**.

CHAPTER I: INTRODUCTION

This chapter presents an over view of various physical and chemical aspects of mesoporous molecular sieve materials. The different characteristic properties of these materials such as shape selectivity, formation mechanisms, acidity and basicity etc., have been discussed. Detailed literature survey over synthesis aspects, characterization techniques, and different catalytic applications will be given. The scope and objectives of the present work will be outlined at the end of this chapter.

CHAPTER II: SYNTHESIS AND CHARACTERIZATION

In this chapter, synthesis of various types of mesoporous materials such as MCM-41, SBA-15 and mesoporous zirconia (Zr-TMS) and functionalization of these materials by various groups such as 3-chloropropyl trimethoxy silane, benzylsulfonic acid etc., have been discussed. Further, various physicochemical characterization techniques such as powder X-ray diffraction (XRD), atomic absorption spectroscopy (AAS), nitrogen sorption technique, FT-IR spectroscopy, X-ray photoelectron spectroscopy (XPS), elemental analysis, temperature programmed desorption (TPD) of ammonia, solid state

^{13}C CP/DD MAS NMR (cross polarization/dipolar decoupled nuclear magnetic resonance) spectroscopy, scanning electron microscopy (SEM), transmission electron microscopy (TEM), and thermo gravimetric analysis (TG-DTA) are discussed and their principles have also been discussed. Catalysis and analysis of products also discussed.

CHAPTER III: CHIRAL METAL COMPLEX IMMOBILIZED MESOPOROUS MCM-41 CATALYSTS

This chapter describes the synthesis of chiral metal complex functionalized mesoporous MCM-41 by post synthetic procedure. The calcined mesoporous MCM-41 materials have been modified by 3-chloropropyltrimethoxy silane followed by reaction with BISPICEN type chiral ligands. Further, the mesoporous catalysts synthesized during this investigation have been characterized by XRD, nitrogen sorption technique, FT-IR spectroscopy, elemental analysis, solid state ^{13}CMAS NMR spectroscopy, SEM, and thermo gravimetric analysis. The synthesized catalysts have been subjected to sulfoxidation reaction of various sulfides and further catalysts recycle study have also been demonstrated.

CHAPTER IV: METAL TRIFLATE IMMOBILIZED MESOPOROUS SBA-15

This chapter deals with the synthesis of different metal triflates supported over mesoporous SBA-15 materials. The catalyst was synthesized by treating the calcined SBA-15 with metal triflate solution. The synthesized catalysts have been analyzed by various physico chemical techniques and the total acidity of the catalysts was analyzed by ammonia TPD measurements. The nature of acid sites present in the catalysts was analyzed by insitu pyridine IR technique and the detailed study has been discussed. The activity of the catalysts was analyzed for Friedel Crafts acylation reaction of naphthalene with p-toluoyl chloride and effect of different parameters such as reaction time, temperature, molar ratio of the reactant etc have been discussed.

CHAPTER V: BENZYLSULFONIC ACID FUNCTIONALIZED MESOPOROUS ZIRCONIA (Zr-TMS-BSA) CATALYSTS

This chapter describes the synthesis of benzylsulfonic acid functionalized mesoporous zirconia via covalent route by post synthetic procedure. Surfactant free Zr-TMS material has been treated with benzyl alcohol and further with chlorosulfonic acid is functionalized over Zr-TMS-BS. The catalysts synthesized during this investigation have been characterized by XRD, surface area measurements, FT-IR spectroscopy, elemental analysis, TPD of ammonia, SEM, and TEM, analysis is discussed. The synthesized catalysts have been subjected to condensation reaction of phenol and substituted phenols with ethyl acetoacetate (EAA). Further, the catalytic reaction parameters, such as, activity of various catalysts, duration of run, influence of catalyst/condensation agent, reaction temperature, influence of molar ratios of reactants have also been demonstrated.

CHAPTER VI: SUMMARY AND CONCLUSIONS

This chapter summarizes the results obtained and the basic findings of the present study.

CHAPTER-1

INTRODUCTION AND LITERATURE SURVEY

1.1. CATALYSIS

An acceleration of the rate of a process or reaction, brought about by a catalyst, usually present in small quantities and unaffected at the end of the reaction is called catalysis. A catalyst permits reactions or processes to take place more effectively or under milder conditions than would otherwise be possible. Catalysts that speed the reaction are called positive catalysts. Catalysts that slow down the reaction are called negative catalysts or inhibitors. Substances that increase the activity of catalysts are called promoters and substances that deactivate catalysts are called catalytic poisons.

Porous materials have been extensively studied with regard to technical applications as catalysts and catalyst supports. According to the IUPAC definition, porous materials are divided into three classes depending on the pore size: microporous (pore size < 2 nm), mesoporous (2-50 nm), and macroporous (>50 nm) materials [1]. The synthesis of mesoporous molecular sieves called M41S is one of the most exciting discoveries in the field of materials synthesis. The discovery of hexagonally ordered mesoporous silicate structures by Mobil Corporation (M41S materials) and by Kuroda et al. (FSM-16 materials) pioneered a new era in material science [2]. These materials possess extremely high surface areas and easily accessible, well-defined mesopores, which broke pore size constraint of microporous zeolites. The M41S family is classified into three members: MCM-41, MCM-48 and MCM-50, with hexagonal 'honeycomb', cubic 'gyroid' and lamellar structures, respectively [2-4]. Recently, neutral nonionic surfactants (block copolymers) were used as templates to prepare mesoporous materials with large pores (HMS, SBA-11, -12, -15, -16 and FDU-1, -2, -5, etc.) [5-11] through hydrogen bonding or electrostatic interactions. The use of anionic surfactants produced only lamellar or disordered silica based mesophases. The synthesis of these materials opens new possibilities for preparing catalysts with uniform pores in the mesoporous region, which will allow the access to relatively larger organic molecules for catalytic transformations [12].

1.2. SYNTHESIS AND MECHANISM OF FORMATION OF MESOPOROUS MATERIAL

An ever growing interest in expanding the pore sizes of zeotype materials from micropore region to mesopores region in response to the increasing demands in both industrial and fundamental studies. Examples are treating heavy feeds, separating and selective synthesizing large molecules and intra zeolite fabricating technology [13, 14]. Zeolitic materials, typically have a surface area of ca. >700 $m^2 g^{-1}$, which

Table 1.1. Pore size definition of zeolites and molecular sieves

Pore size (Å)	Definition	Typical material	Ring size	Pore diameter (Å)
>500	Macroporous			
20-500	Mesoporous	MCM-41, Zr-TMS		15-100
<20	Microporous			
	Ultra-large pore	Cloverite	20	6.0 x 13.2
		JDF-20	20	6.2 x 14.5
		VPI-5	18	12.1
		$AlPO_4$-8	14	7.9 x 8.7
	Large pore	Faujasites	12	7.4
		Beta	12	
		Mordenite	12	6.7 x 7.0
		$AlPO_4$-5	12	7.3
		ZSM-12	12	5.5 x 5.9
	Medium pore	ZSM-48	10	5.3 x 5.6
		ZSM-5	10	5.3 x 5.6; 5.1 x 5.5
	Small pore	CaA	8	4.2
		SAPO-34	8	4.3

are not truly crystalline like microporous zeolites but because of rapid growth of the research on these materials make them to be classified as mesopore zeolites, with the majority of this surface inside the pores and accessible only through apertures of well-defined dimensions [15]. In 1992, researchers at Mobil Corporation discovered the M41S family of silicate/aluminosilicates mesoporous molecular sieves with exceptionally large uniform pore structures, which has resulted in a worldwide resurgence in this area [2, 16]. Three different mesophases in this family have been identified, i.e. lamellar [17], hexagonal and cubic phases [18], in which the hexagonal mesophase, MCM-41, possesses highly regular arrays of uniform-sized channels whose diameters are in the range of 15-100 Å depending on the templates used, the addition of auxiliary organic compounds (co-template) and the reaction parameters. The pores of this novel material are nearly as regular, yet considerably larger than those present in crystalline materials such as zeolites, thus offering new opportunities for applications in catalysis [19] and advanced composite materials [20].

The M41S family of mesoporous materials is synthesized using a silica source and different organic structure directing agents, *e.g.*, cationic surfactants containing long alkyl chain quaternary ammonium compounds containing 10–20 carbons, often followed with addition of co-surfactants. The dependence of surfactant/silica molar ratio in a ternary synthesis system containing tetraethylorthosilicate (TEOS, silica source), water and cetyltrimethylammonium ($C_{16}TMA^+$) cations (surfactant) at 100 °C on appearance of different phases of M41S family is summarized in Table 1.2.

A number of models have been proposed to rationalize the mechanism of formation of mesoporous materials by various synthesis routes. All these models are based on the role of surfactants in solution to direct the formation of silicate mesostructure. In solution, the surfactants have a hydrophilic head group and a long chain hydrophobic tail group within the same molecule, which will aggregate and self-organize in such a way so as to minimize the contact between the incompatible ends. Different types of interaction between the surfactant and the inorganic precursor under different synthesis conditions leads to different postulates for the mechanism of formation of mesoporous materials, which will be discussed briefly in this section.

1.2.1. Liquid Crystal Templating (LCT) Mechanism

The researchers of Mobil Corporation proposed a liquid crystal templating (LCT) mechanism to explain the formation of M41S type mesoporous materials [2, 16]. The mesostructure formation depends on the hydrocarbon chain length of the

Table 1.2. Effect of surfactant/silica molar ratio on emergence of different mesophases

Surfactant/Silica	Different phases of M41S type materials
< 1.0	Hexagonal (*p6mm,* MCM-41)
1.0-1.5	Cubic (*Ia3d,* MCM-48)
1.2-2.0	Thermally unstable materials
2.0	Cubic octamer $[(C_{16}TMA)SiO_{2.5}]_8$

surfactant tail group, [18] the effect of variation of the surfactant concentration and the additional organic swelling agents. The lowest concentration at which the surfactant molecules aggregate to form spherical isotropic micelles is called critical micelle concentration (CMC_1). Further increase in the surfactant concentration initiates aggregation of spherical into cylindrical or rod-like micelles (CMC_2). There are three main liquid crystalline phases with hexagonal, cubic and lamellar structures.

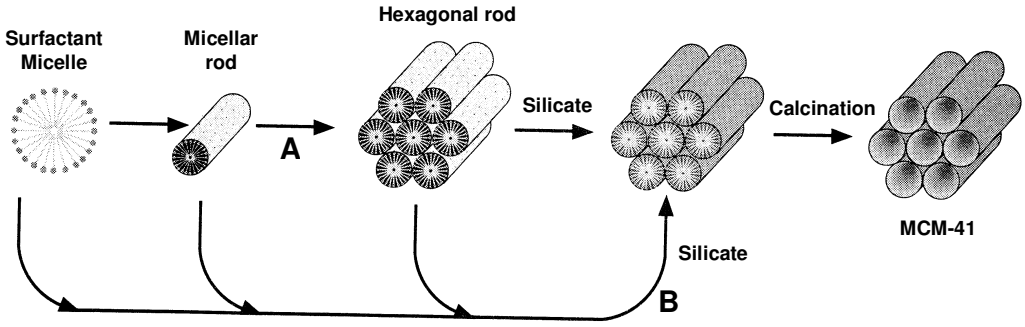

Scheme 1.1. Liquid crystal templating (LCT) mechanism proposed for the formation of MCM-41; (A) liquid crystal phase initiated and (B) silicate anion initiated. [Source: Ref. [18]]

The hexagonal phase is the result of hexagonal packing of cylindrical micelles, the lamellar phase corresponds to the formation of surfactant bilayers and the cubic phase may be regarded as a bicontinuous structure.

The Mobil researchers proposed two synthesis mechanisms [2, 16]. In the first route, the $C_nH_{2n+1}(CH_3)_3N^+$ surfactant species organize into lyotropic liquid crystal phase, which can serve as template for the formation of hexagonal MCM-41 structure. First the surfactant micelles aggregate into a hexagonal array of rods, followed by interaction of silicate or aluminate anions present in the reaction mixture with the surfactant cationic head groups. Thereafter condensation of the silicate species occurs, leading to the formation of an inorganic polymeric species. After combusting off the surfactant template by calcination, hexagonally arranged inorganic hollow cylinders are produced (Scheme 1.1). However, the drawbacks of this synthesis pathway was pointed out by Cheng et al. [21], according to whom the hexagonal liquid-crystal phase does not form below 40% of surfactant concentration.

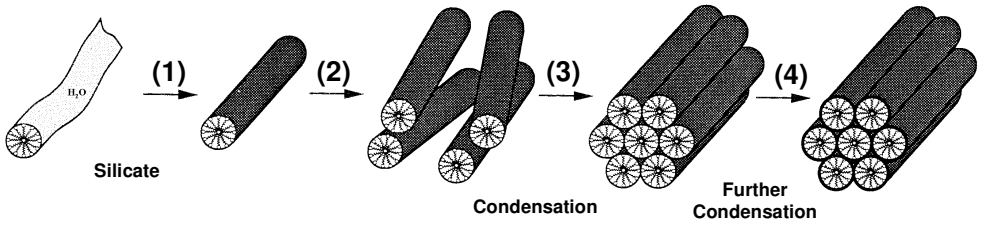

Scheme 1.2. Silicate rod assembly proposed for the formation of MCM-41; (1) and (2) random ordering of rod-like micelles and interaction with silicate species, (3) spontaneous packing of the rods, and (4) remaining condensation of silicate species on further heating. [Source: Ref. [22]]

It is known that MCM-41 may be formed at low surfactant concentrations (1 wt %) with respect to water content, and *in situ* ^{15}N NMR spectra indicated that the hexagonal liquid-crystalline phase was not present anytime during formation of MCM-41 [22].

In the second route, the hexagonal ordering is initiated by the presence of silicate species in the reaction mixture [2, 16]. Chen et al. explained that randomly distributed

surfactant micelles with rod-like morphology form initially, and their interaction with silicate oligomers generate randomly oriented surfactant micelles surrounded by two or three silica monolayers. The presence of rod-like micelles in solution was supported by isotropic *in situ* ^{15}N NMR [22]. Further condensation between silicate species on adjacent rods occurs on heating, initiating the long-range hexagonal ordering (Scheme 1.2).

1.2.2. Charge Density Matching

The 'charge density matching' model proposed by Stucky *et al*. suggested that condensation occurs between initially formed silicate species by the electrostatic interaction between the anionic silicates and the cationic surfactant head groups, [23, 26]. This eventually reduces the charge density and therefore, curvature was introduced into the layers to maintain the charge density balance with the surfactant head groups, which leads to transformation of the lamellar mesostructure into the hexagonal one (Scheme 1.3.A). Although this silica-initiated synthesis mechanism has been widely accepted, the presence of an intermediate lamellar species has been disputed.

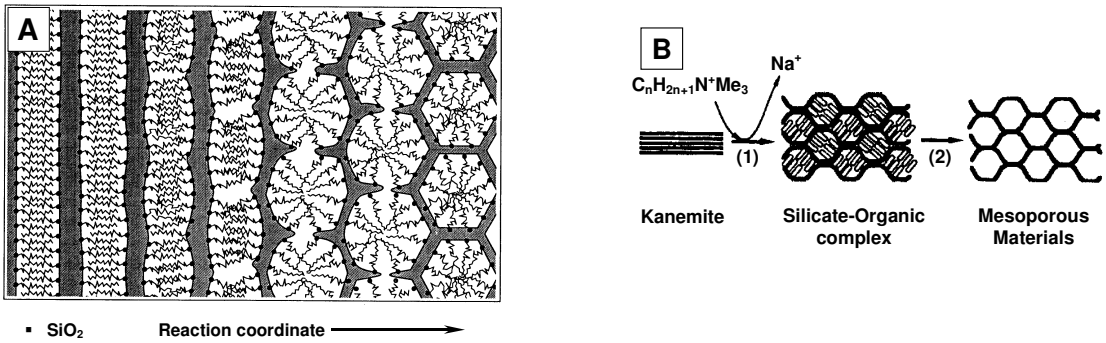

Scheme 1.3. Transformation of surfactant-silicate systems from lamellar to hexagonal mesophases; (A) hexagonal mesophase obtained by charge density matching, and (B) folding of kanemite silicate sheets around intercalated surfactant molecules. [Source: Refs. [23] [24] and [25]].

1.2.3. Folded Sheet Mechanism

The 'folded-sheet mechanism' postulated by Inagaki et al. indicated the presence of intercalated silicate phases in the synthesis medium of the reaction products (Scheme 1.3.B) [24]. The flexible silicate layers of kanemite fold around the surfactant cations, and cross-linking of the interlayer occurs by condensation of silanol groups on adjacent silicate sheets. On increase of pH, the amount of occluded $C_nH_{2n+1}(CH_3)_3N^+$ cations in kanemite increases resulting in expansion of the kanemite interlayers to form another class of regular hexagonal structure called FSM-16.

1.2.4. Silicatropic Liquid Crystals

Firouzi et al. have developed a model based on cooperative organization of inorganic and organic molecular species into 3D structured arrays [25, 27]. According to this model, the physicochemical properties of a particular system were not determined by the organic arrays having long-range preorganized order, but by the dynamic interplay among ion-pair inorganic and organic species, so that different phases can readily be obtained through small variation of controllable synthesis parameters. The exchange of silicate anions with the surfactant halide counter ions formed the 'silicatropic liquid crystal' (SLC) phase (Scheme 1.4), which exhibited very similar behavior to that of typical lyotropic systems and finally condensed irreversibly in to MCM-41.

1.2.5. Generalized Liquid Crystal Templating Mechanism

1.2.5.1. Ionic Route (Electrostatic Interaction)

Huo et al. proposed a generalized mechanism for the formation of mesostructures, which was based on specific types of electrostatic interaction between an inorganic precursor (I) and a surfactant head group (S) [28, 29].

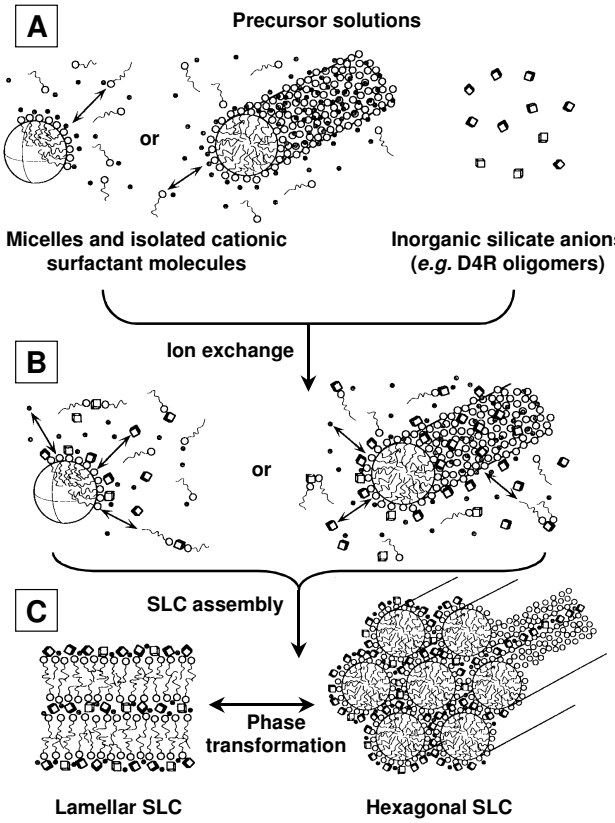

Scheme 1.4. Cooperative organization for the formation of silicatropic liquid crystal phase / silicate-surfactant mesophases; (A) organic and inorganic precursor solutions, (B) preliminary interaction of the two precursor solutions after mixing, and (C) multidentate interaction of the oligomeric silicate units with the surfactant molecules. [Source: Ref. [27], [28]]

In this concept, four different approaches were proposed to synthesize transition metal oxide mesostructures. The first route involves the charge density matching between surfactant cations and inorganic anions (will be referred to as S^+I^- hereafter).

The second route deals with the charge-reversed situation, *i.e.*, anionic surfactant and cationic inorganic species (S^-I^+). Both the third and fourth routes are counterion-mediated pathways. The third one demonstrates the assembly of cationic species *via* halide ions ($S^-X^+I^-$), while the fourth one depicts the assembly of anionic species *via* alkali metal ions ($S^+X^-I^+$). These synthesis strategies are acceptable for the formation of a

wide variety of lamellar, hexagonal or cubic mesophases. However, a general problem negotiated very often is the poor stability of the inorganic framework, which frequently collapses after removal of the surfactant.

1.2.5.2. Neutral Templating Route (Hydrogen Bonding Interaction)

Tanev and Pinnavaia proposed another route to synthesize hexagonal mesoporous silicas (HMS) having thicker pore walls, high thermal stability and smaller crystallite size but, having higher amounts of interparticle mesoporosity and lower degree of long-range ordering of pores than MCM-41 materials [5, 30, 31]. This route is essentially based on hydrogen bonding between neutral primary amines (S^0) and neutral inorganic precursors (I^0), wherein hydrolysis of tetraethyl orthosilicate (TEOS) in an aqueous solution of dodecylamine yields neutral inorganic precursor. Using the same approach, porous lamellar silicas with vesicular particle morphology have been synthesized with the aid of double headed alkylamines linked by a hydrophobic alkyl chain (α,ω-dialkylamine).

1.2.5.3. Ligand-Assisted Templating Route (Covalent Interaction)

Antonelli and Ying have proposed a ligand-assisted templating mechanism for the synthesis of hexagonally packed mesoporous metal oxide completely stable to surfactant removal. In a typical synthesis, the surfactant was dissolved in the metal alkoxide precursor before addition of water to allow nitrogen–metal covalent bond formation between the surfactant head group and the metal alkoxide precursor. The existence of this covalent interaction was confirmed by ^{15}N NMR spectroscopic studies. In this approach, the structure of the mesophases could be controlled by adjustment of the metal/surfactant ratio, which led to a new class of mesoporous transition metal oxides analogous to M41S family.

1.3. CONTROL OF CRYSTAL SIZES, PORE SIZES AND MORPHOLOGY

The past decade saw extensive research to control the crystal size, pore dimensions and pore sizes of ordered mesoporous materials, particularly for MCM-41

with unidirectional channels. The control of crystal size is of immense importance when these materials are to be used in catalytic processes. The length of the pores must be decreased as much as possible to overcome diffusion limitations, which is normally done by decreasing crystallite size. Wu et al. have synthesized thermally stable hexagonal mesoporous materials of smaller crystal sizes (~100 nm) by microwave heating of precursor gels at 150 ºC for not more than 1 h [32]. The fast and homogeneous condensation reactions occurring during microwave synthesis leads to smaller crystal sizes and high thermal stability.

The characteristic feature of the M41S type molecular sieves is the flexibility to synthesize these materials with different pore diameters ranging from 2–10 nm. This can be achieved by the following ways: (i) variation of the chain length of the hydrophobic alkyl group (8 to 22 carbon atoms) in the surfactant molecules [2], (ii) addition of organic swelling agents such as 1,3,5-trimethylbenzene [2], or alkanes of different chain length [33], which will increase the micellar size by solvation of the added hydrophobic molecules in the hydrophobic region of the micelles, and (iii) by adjusting the composition of the gel and the crystallization variables [34]. Sun and Ying have demonstrated the tailoring of pore sizes between 0.5 and 2 nm employing short-chain alkylamines as supramolecular templates, *via* the "ligand-assisted templating" route [35, 36].

The morphology of the mesoporous materials obtained by Beck et al. consisted of aggregates and loose agglomerates of small particles. However, well-defined morphologies like fibers, thin films, spheres, monoliths *etc*. of these mesoporous materials are required for a wide range of applications such as membranes for large molecule catalysis, separation, optical sensors, slow drug release systems, templates for the assembly of nanostructures, masks for high-resolution lithography, low dielectric constant films for microelectronics and other interface-controlled processes. Huo et al. [28] and Yang et al. [37] have synthesized mesoporous silica with highly curved morphologies (toroidal, disk-like, spiral and spheroidal shapes) in acidic medium *via* the $S^+X^-I^+$ route. Mesoporous fibers (length 50–1000 μm) have been prepared in oil-in-water emulsions [38] and in aqueous phase [39] under acidic conditions ($S^+X^-I^+$). Highly

oriented mesoporous free-standing films (diameter ≤10 cm, thickness ~10–500 mm) have been synthesized at the air-water [40] and oil-water [38] interfaces, on both mica [41] and the graphite [42] surfaces and by using dip- or spin-coating [43] methods. The syntheses of hollow (diameter 1–100 μm) [38] as well as hard (diameter 0.1–2 mm) [44] mesoporous silica spheres were achieved through emulsion biphasic chemistry, whereas monolithic periodic mesoporous silica (diameter 150–500 nm, interparticle pores on the order of particle size) was prepared by different systems using ionic [45] and neutral surfactants [46]. Another morphology with vesicle like hierarchical structures, consisting of one or more undulated silica sheets (thickness 3 nm, mesopore diameter 2.7–4.0 nm) running both parallel and orthogonal to the silica sheets, was prepared by Kim et al. using neutral gemini surfactants [47].

1.4. REMOVAL OF TEMPLATE

Removal of template plays a crucial role in the preparation of mesoporous materials. Depending on the preparative method template can be removed either by calcination [48] in air or by solvent extraction [49]. Calcination is the better method than removal by extraction techniques. This is due to the strong interaction between template and inorganic species in the case of direct pathways or mediated pathways where electrostatic interactions play a key role for the formation of meso-structure. The calcination has to be done in the flow of inert gases at the initial stages followed by the flow of air. This is due to maintain the crystallinity of the material. But extraction prefers when we need rich amount of hydroxyl groups in the catalysts [50].

1.5. SURFACE MODIFICATION OF MESOPOROUS MATERIALS

The application of pure mesoporous silicates or aluminosilicates as catalysts is rather limited because of the limitations in the nature of their active sites, leading to limited scope of the reactions they could accomplish. To utilize these mesoporous materials for several specific applications including catalysis and also sorption, ion exchange, sensing *etc*., the introduction of reactive organic functional groups by

modifying the inner surfaces of these materials, to form inorganic–organic hybrid materials, is essential [51]. The inorganic components of these inorganic–organic hybrid materials can provide mechanical, thermal or structural stability, while the organic components can introduce flexibility into the framework and can more readily be modified for specific applications [52]. The presence of large amount of silanol groups in the surfaces of M41S materials could be exploited for anchoring of desired organic functional groups by condensation with necessary alkoxysilane precursors [53]. These parent organic functional groups, with or without further modification, can facilitate anchoring of different types of catalytically reactive metal particles or organometallic complexes inside the mesoporous network [54]. Different methods for organic modification of mesoporous surfaces will be briefly highlighted in this section.

1.5.1. Grafting Methods

Grafting refers to post synthesis modification of the inner surface of mesoporous silica, where the organic functional groups are introduced as the terminal groups of an organic monolayer [55]. The large concentration of surface silanol [$(–SiO)_3Si–OH$)] groups present in mesoporous silica can be utilized as convenient moieties for anchoring of organic functional groups [56]. The surface modification with organic functional groups is generally carried out by silylation, as depicted in Scheme 1.5.

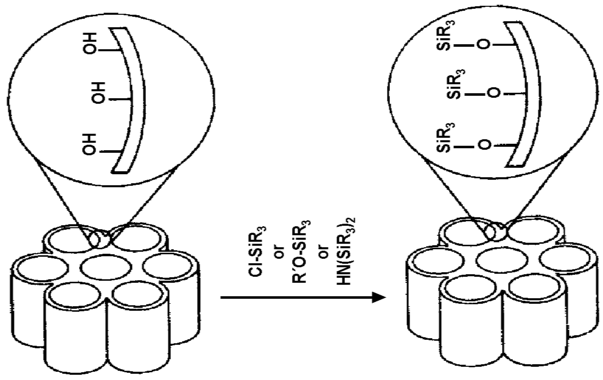

Scheme 1.5. Functionalization of inner walls of mesoporous silicates by grafting [Source: Ref. [51]]

The surfactant molecules from the mesopores are usually removed either by calcination or by extraction with appropriate solvents. At typical calcinations temperatures (~500 °C) several surface silanol groups are lost after condensation of unreacted silanol groups. However, it is necessary to maintain a large concentration of surface silanol groups after calcination, if a high coverage of organic functional groups on the surfaces is desired. This can be achieved by treatment of calcined mesoporous silica with boiling water [57] or steam [58], or by acid hydrolysis [59]. Solvent-extraction processes reduce the possibility of loss of surface silanol groups, although thermal treatments after extraction can increase the surface reactivity towards silylation.

1.5.1.1. Grafting with Passive Surface Groups

Organic functional groups with lower reactivity such as alkyl or phenyl groups could be grafted to alter the accessible pore volume of mesoporous silica, thereby enhancing the hydrophobicity of the surface and protecting towards hydrolysis. The pore diameters of ordered mesoporous materials could be adjusted by varying the alkyl chain length of the silylating agent or the quantity of the silylating agent [60]. The most commonly used surface modifying agents containing lower reactive functional groups are trimethylchlorosilane (Me_3SiCl) [61], and hexamethyldisilaxane [$(Me_3Si)_2NH$] [62].

1.5.1.2. Grafting with Reactive Surface Groups

Grafting of the mesopore surfaces with reactive functional groups like olefin, cyanide, thiol, amine, halide, epoxide *etc*. permits further functionalization of the surface. Further functionalization includes hydroboration [63] and bromination [62] of olefins (vinyl groups), hydrolysis of cyanides to carboxylic acids [64], oxidation of thiols to sulfonic acids [65, 66] alkylation and nucleophilic substitution of amines [67], and nucleophilic substitution of halides [68]. After the desired modification of the reactive functional groups, a rational design for anchoring of catalytically active transition metal complexes onto mesoporous network could be made [69].

1.5.1.3. Site-Selective Grafting

For grafting of organic functional groups, the external surface of the mesoporous materials are kinetically more accessible than the internal surface and is functionalized predominantly [70]. To minimize the grafting on the external surface, it is necessary to passivate the silanol groups on the external surface before functionalizing those on the internal surface. Shephard et al. have carried out the passivation of external surface with dichlorodiphenylsilane (Ph_2SiCl_2) first, and functionalization of internal surface with 3-aminopropyltrimethoxysilane [$(MeO)_3Si(CH_2)_3NH_2$] thereafter [71]. The existence of the amine functional groups almost entirely on the internal surface was confirmed by high-resolution transmission electron microscopy (HRTEM).

In a different approach, grafting of the external surface by Me_3SiCl was carried out on the as-prepared mesoporous material without the surfactant being removed from the mesopores [72]. Grafting occurred mainly on the external surface due to steric constraint of the surfactant. After solvent extraction of the surfactant the internal surface was functionalized with the desired organic group. An alternate pathway by Antochshuk and Jaroniec describes simultaneous grafting of Me_3SiCl and extraction of surfactant template, by refluxing as-synthesized MCM-41 material with neat Me_3SiCl [73]. Since the calcination step is not required in these two processes, larger numbers of surface silanol groups are likely to be present inside the mesopores.

1.5.2. Co-condensation Reactions

In the grafting methods, incorporation of organic groups is done by attachment of the organosiloxane precursor with surface Si atoms through Si–O–Si–C covalent bond formation (Scheme 1.6). Then Si–O can be cleaved at some reaction conditions as experienced by Price et al. [55]. Therefore, in some cases it would be desirable to have direct formation of a C–Si (surface) covalent bond. Thus, the "one-pot" co-condensation method, where condensation occurs between a tetraalkoxysilane and one or more trialkoxyorganosilanes through sol-gel chemistry, seems to have distinct advantages over the grafting methods (Scheme 1.6) [74].

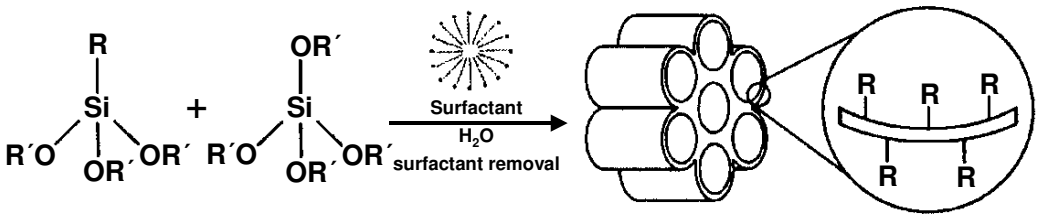

Scheme 1.6. Synthesis of organo-functionalized mesoporous silicates by co-condensation. [Source: Ref. [52]]

Several research groups have employed this method to prepare inorganic–organic hybrid mesoporous materials under a wide range of synthesis conditions [64, 75-78]. Usually the solvent extraction technique is used to remove the surfactant from the resultant materials. The co-condensation reactions proceed through different pathways, which will be discussed briefly in this section.

1.5.2.1. S^+I^- Pathway

This pathway refers to condensation between anionic silica precursors (I^-), obtained under basic conditions, initiated by cationic surfactant (S^+) micelles. The surfactants are normally extracted with acid-alcohol mixtures [22, 62]. It has been observed that the d_{100} spacing and the pore size of the channels are significantly reduced as the concentration of the trialkoxyorganosilanes increases, even when the same surfactant is used [70, 76]. Simultaneously, an increase in wall thickness has been observed, probably because of protrusion of organic groups into the channels. The decrease in cell dimensions may be attributed to the interaction between nonpolar organic groups and the surfactant tails, which drag the organic precursor further into the micelles. Functionalization with two or more organic groups is also possible in this pathway [79, 80]. However, the functional groups are randomly distributed in the resultant material, and their location cannot be controlled as precisely as done by the grafting processes mentioned earlier.

1.5.2.2. $S^+X^-I^+$ Pathway

In this pathway interaction of cationic silicate precursors (I^+), obtained under acidic conditions, occurs with the S^+X^- pair, where S^+ represents cationic surfactant species and X^- denotes anions generated from the acid [77, 81, 82]. Unlike the S^+I^- pathway, a simple extraction technique using pure solvent can be used to remove the surfactant.

1.5.2.3. S^0I^0 Pathway

This mechanism deals with a weak interaction between a neutral silica precursor (I^0) and neutral surfactant micelles (S^0) [77, 83, 84]. In this case also, surfactant removal can be achieved by extraction with pure solvent. The pore volume and surface area do not vary systematically with increasing concentration of the organosilane, but smaller pore sizes have been obtained with increasing the same [84].

1.5.2.4. N^0I^0 Pathway

In this pathway, non-ionic surfactants (N^0) like alkylpoly ethyleneoxide are used as the template, and the syntheses are carried out at neutral P^H [85, 86]. Worm-like channel structures have been obtained in this method. The cell dimensions usually get reduced with higher loading of organic functional groups [85].

1.6. ORGANO-FUNCTIONALIZED MESOPOROUS MATERIALS

The mesoporous MCM-41 materials add a new dimension due to their large and variable pore diameters. Grafting of functional organosilanes by using surface hydroxyl groups as anchor points has been widely used in the field of catalysis. Important applications of these modified and functionalized systems are heterogeneous catalysis and photocatalysis involving bulky grafted catalysts and/or the conversion of large substrates. Other potential applications include ion exchange and separations, removal of heavy metals, chromatography, stabilization of quantum wires, stabilization of dyes, and polymer composites [12, 65]. The introduction of functional organic groups is usually

performed through attachment of silane-coupling agents to mesoporous walls of previously synthesized and calcined materials. The functional group is either directly incorporated in the silane-coupling agent or it is grafted onto it in a second or further reaction step. Co-condensation of reactive species during the mesopores synthesis is a method to incorporate functionality into the walls of the channel system [52, 87]. Macquarrie et al. and Brunel et al. have explained the covalent attachment of basic functional groups such as amino group on the MCM-41 surface which can be either used as base catalysts or used as an anchor point for asymmetric ligands assembly [67, 68, and 88]. Surface modification techniques are enjoying a renewed interest, and it is clear that the pore walls of mesoporous materials are easily modified with either purely inorganic or with hybrid, semi-organic functional groups and can be successfully used as catalysts for green chemistry [89, 90].

1.7. MESOPOROUS SILICA AS SUPPORT OR HOST FOR THE HETEROGENIZATION OF HOMOGENEOUS CATALYSTS

Materials with well-defined pores belong to the most interesting class of compounds, because they can be converted into organic-inorganic hybrid nanocomposites by various surface modifications. The microporous and organized mesoporous materials obtained after the hydrothermal synthesis are in fact a nonporous organic-inorganic hybrid since the organic structure director (template or surfactant) is usually trapped in the cavities of the solid. Hence, to obtain completely porous solid and to introduce reactive organic functional groups inside the channels of ordered materials, it is necessary to remove the entrapped organic species from the assynthesized samples. The commonly employed method for the removal of surfactant consist of calcining the materials, in a flow of air, typically >400 °C. However, the high-cost template reactant is destroyed and such treatments further cause damage to the porous materials, since during calcination high local temperature and water formation may occur, and therefore extra framework sites may be formed [91]. An alternative method involves the removal of the template by

mild treatments such as liquid extraction using acidic solutions, alcohols or a mixture of both [30, 92].

This method is especially effective for mesoporous materials where the framework surfactant interactions are weak (electrostatic, van der Waals or hydrogen bonding interactions) and because of the larger pore sizes. An added advantage of this method is that under acidic extraction conditions, exchange of sodium ions for protons is also achieved simultaneously with the removal of surfactants. Moreover, the mild route for the removal of templates helps in the reuse of the organic templates for a subsequent synthesis with similar textual properties [93]. The materials obtained after the removal of surfactant groups contains ordered pore channels with abundant silanols sites. These mesoporous hosts can be utilized for the synthesis of organic-inorganic hybrid mesoporous materials having reactive functional groups and have stimulated fundamental research interests in the inclusion of metals and metal complexes inside the mesoporous channels [94]. During the last few years, organic-inorganic hybrid mesoporous materials constitutes an emerging area in the field of materials science and had shown its impact in a wide range of heterogeneous catalysis reactions [95].

However, the main problem encountered in heterogenized catalysts is that the bonds between metal and ligand are often broken and reformed during catalytic reactions, leading to leaching of the metal from the catalyst in the product, thus decreasing the reaction rate and activity [96]. Hence the nature of interaction between the homogenous catalyst and the support surface decides the overall stability and reusability of the heterogenized catalysts and in general, if the anchoring is covalent, it can be robust enough to withstand the harsh conditions of the catalytic reactions. The most common immobilization techniques used for this purpose include grafting or tethering, physical entrapment, ship-in-a-bottle synthesis and supported liquid phase catalysis [54, 97]. Earlier, the supports used to tether the homogeneous catalyst are the organic polymers, which are soluble in the reaction media. The advantage of this support is that the active sites are distributed through out the reaction solution and hence the catalyst architecture is similar to that of the homogeneous catalyst that it is trying to mimic [98]. Insoluble supports are preferable than the homogeneous supports because of several reasons i.e.

they are readily recovered, they have potential applications in flow process and they do not need extra solvents for precipitation. Insoluble organic polymers are effective supports, but the polymer had to be carefully chosen and tuned so as to avoid swelling and to ensure that the homogeneous complex catalyst is tightly bound with the support not merely occluded inside. In contrast to the insoluble organic polymers, inorganic silica materials like amorphous silica gels or mesoporous silicas did not swell or dissolve in organic solvents. However, because of the lack of ordered pore channels, amorphous silica gels are unable to provide the size/shape specificity properties. Hence the immobilization of various homogeneous metal catalysts over solid organic-inorganic hybrid mesoporous supports as a mean of 'heterogenization' has particular significance. Heterogenization of useful homogenous catalysts or active centers will improve the overall efficiency of the catalytic process due to: (i) it is easier to separate the catalyst from the liquid by simple filtration, where the homogenous catalyst often leads to complicated and laborious extraction or distillation requirements, (ii) often the catalysts can be regenerated and recycled, (iii) confinement of the catalyst in the mesopores provides a means of introducing the size/shape selectivity and thus a greater specificity to a desired reaction. Moreover, if the functional groups or the catalytic active site was attached firmly to the solid support, the leaching problem, usually encountered in liquid phase reactions, can be greatly reduced.

1.8. ZIRCONIA IN CATALYSIS

Over the last ten years, the zirconia used as catalyst or catalytic support and attracted much attention this is due to the high thermal stability, remarkable mechanical strength, easy availability, high melting point, low thermal conductivity, high corrosion resistance, amphoteric behavior and unique properties of the surface [3, 99-102]. Zirconia exhibits several crystalline modifications: monoclinic, that is thermally stable at the temperature below 1172 °C, tetragonal, stable at the temperature range 1172-2347 °C, cubic, stable above 2347 °C and rhombic, stable at a high pressure. However, tetragonal and cubic zirconia can be prepared at low temperatures (in the range of 550-750 °C) in

the form of highly dispersed metastable phase. Zirconia can be prepared by precipitation as well as sol-gel method [103].

Doping of other elements will also affect the catalytic properties of zirconia. High surface area zirconia is widely used as a catalytic support of novel methods or oxygen censor electrolytes in automobile exhaust emission control system. Doping of zirconium with small amounts of rare earth elements may tailor its properties for better catalytic performance.

1.9. MESOPOROUS ZIRCONIA IN CATALYSIS

After the discovery of the MCM-41 type materials, various researchers put forward an idea of non-silica-based mesoporous oxides. Titanium [104, 105] zirconium [106-119] niobium [120], tantalum [121], aluminum [122], hafnium [123], tin [124], and manganese [125] have been synthesized using ionic or neutral templates as structure directing agents, although most of them were comprised of mainly non-porous framework walls, which would limit their thermal and hydrothermal stability and greatly compromise their usefulness in catalytic application. Stucky et al. then synthesized mesoporous metal oxides with a semi crystalline framework by block copolymer templating materials [126].

Transition metal oxides are widely used as industrial catalysts and as catalysts supports. Unfortunately they usually have poorly defined pore structures. The synthesis of mesoporous silica partially substituted by titanium and zirconium has been attempted to circumvent the difficulty of preparing stable mesoporous titania and zirconia. Zirconium oxide is of particular interest because it contains both acidic and basic surface sites. Further, we have chosen zirconium as the metal species because it has only one stable oxidation state and exhibit pronounced polyoxo ion chemistry in aqueous solutions [129]. These are critical for some reactions that need bifunctional catalysts. The search for zirconium oxide as supports for various catalysts has received keen interest in the past decade. In the recent years SO_4^{2-}/ZrO_2 has attracted attention as it catalyzes various industrially important reactions such as: isomerization; condensation; Friedel-Crafts acylation reactions; etc [130]. However, its non-uniform pore size, low porosity, and

small surface area limit its potential application for catalyzing reactions of bulky molecules. Despite these limitations zirconia has a high melting point, low thermal conductivity, high corrosion resistance, and amphoteric behavior, all of which can be useful properties for a support material. Parvulescu et al. studied extensively the synthesis of mesoporous zirconium oxide using cationic surfactant and claimed that the synthesis occurred via a scaffolding mechanism [131]. The possibility of obtaining such material with a mesoporous texture has made this oxide even more interesting.

The zirconium based mesoporous materials were first reported by Hudson and Knowels, using cationic surfactant by adopting the scaffolding mechanism, where the preparation of mesoporous zirconium (IV) oxide samples was obtained by surfactant exchanged hydrous zirconium (IV) oxide [106].

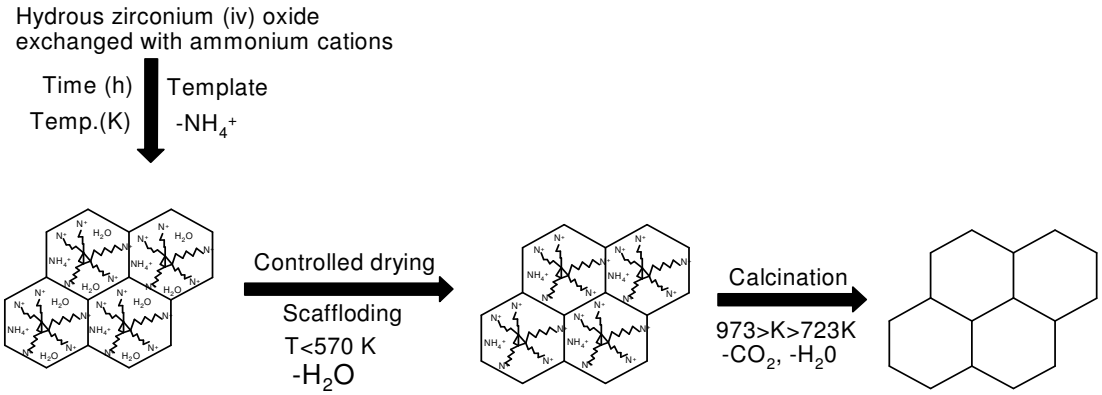

Scheme 1.7. Synthesis of mesoporous zirconia using zirconium (IV) oxide with cationic surfactant via scaffolding mechanism [Source. Ref. [106]].

The scaffolding mechanism was proposed by Ciesla et al. [107, 108] where they observed the formation of porous zirconium oxo phosphate by a surfactant-assisted synthesis, leading to zirconia compounds with high surface areas and regular pore systems, in which either zirconium sulfate or zirconium propoxide is used as zirconia source with cationic surfactant to obtain sulfate containing material. Blin et al. [109]

studied the kinetics of the synthesis mechanism by using cationic surfactant with zirconyl chloride as zirconia source.

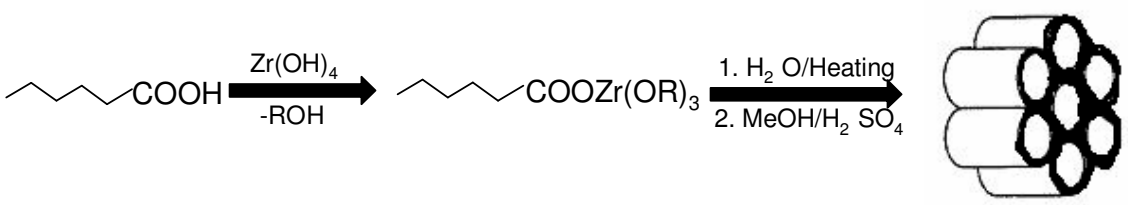

Scheme 1.8. Synthetic strategy for mesoporous zirconia. In the first step the metal alkoxide is combined with the carboxylic acid prior to addition of water. After addition of water and aging form ambient to 150 °C over several days the mesostructure is obtained. [Source: Ref. [111]]

There are so many reports available for synthesis of mesoporous zirconia and modified mesoporous zirconia by using different types of surfactant and different zirconia precursor etc., . Ulagappan et al. [110] reported the preparation of lamellar and hexagonal forms of mesoporous zirconia by the neutral amine route. They further reported that they found the lamellar form of mesoporous zirconia turned in to hexagonal form upon removal of template. Antonelli [111] used long chain carboxylic acid surfactant for the mechanistic study of sulfated mesoporous zirconia (Scheme 1.8). Reddy and Sayari [112] studied the formation of nanoporous zirconium oxide using cationic template at acidic pH via supramolecular templating approach. Zhao et al. [113] reported metal doped mesoporous zirconia using anionic surfactants with various Al/Zr ratios. Pacheco et al. [114] studied the formation of mesoporous zirconia from anionic and neutral surfactants.

Huang et al. [116] demonstrated synthesis of mesoporous sulfated zirconium dioxide with partially tetragonal wall structure and successfully tested in n-butane isomerization and alkylation of 1-naphthol reactions. Wong and Ying [115] studied the mesostructured zirconium oxide formation by using variety of head (anionic and nonionic) and tail group chain length (1-18 carbons). They proposed two types of interaction between the surfactants and zirconium source (Scheme 1.9). Chen et al. [117]

studied the metal oxide containing ordered porous zirconium oxide and tailoring of the pore size of mesoporous sulfated zirconia.

McIntosh and Kydd [118] studied the tailoring the pore size of mesoporous sulfated zirconia via liquid crystal templating mechanism using neutral template. Larsen et al. [119] synthesized mesoporous sulphated zirconia by adopting template-assisted mechanism and they used these materials as a catalyst as well as catalyst support. Porous zirconia is attracting increasing interest on account of its use as a catalyst support or membrane partially because it is chemically more stable. Usually it has been prepared through a template-assisted mechanism.

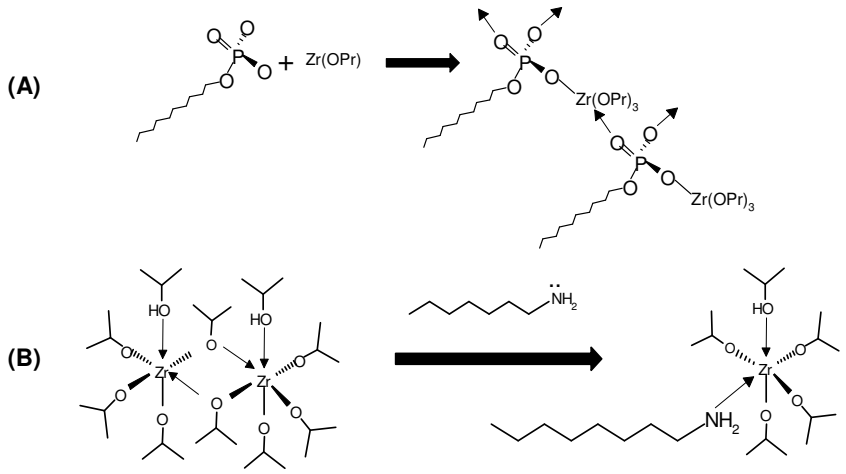

Scheme 1.9. Representative schematic drawings of (A) the anionic amphiphile-zirconium n-propoxide interaction, and (B) the nonionic amphiphile-zirconium isopropoxide interaction. [Source: Ref. [115].

After the formation of pore structure, the template was removed by extraction or calcination at 550 °C. If the temperature is going above 600 °C zirconia starts to transform from the metastable (tetragonal) phase to the stable monoclinic phase. This phase transformation is accompanied by a dramatic change in pore structure of zirconia. At temperatures lower than phase transformation temperature, the pore structure of zirconia also changes, but to a lesser extent, as a result of sintering and grain growth. Metal oxides like yttria, ceria, magnesia or lanthana can stabilize the tetragonal phase

through doping. It is further know that the catalytic efficiency of metal oxides can be improved by doping the metal oxide with a metal [127] and functionalizing the acidic organo-species over support materials [128].

1.10. REFERENCES

[1] K. S. W. Sing, D. H. Everett, R. A. W. Haul, L. Moscou, R. A. Pierotti, J. Rouquerol, T. Siemieniewska, *Pure Appl. Chem., 57,* **1985**, 603.

[2] C. T. Kresge, M. E. Leonowicz, W. J. Roth, J. C. Vartuli, J. S. Beck, *Nature, 359,* **1992**, 710.

[3] A. Corma, *Chem. Rev.,* 97, **1997**, 2373.

[4] T. Linssen, K. Cassiers, P. Cool, E. F. Vansant, *Adv. Colloid Interface Sci., 103,* **2003**, 121.

[5] P. T. Tanev, T. J. Pinnavaia, *Science, 267,* **1995**, 865.

[6] S. A. Bagshaw, E. Prouzet, T. J. Pinnavaia, *Science, 269,* **1995**, 1242.

[7] D. Zhao, Q. Huo, J. Feng, B. F. Chmelka, G. D. Stucky, *J. Am. Chem. Soc., 120,* **1998**, 6024.

[8] C. Yu, B. Tian, J. Fan, G. D. Stucky, D. Zhao, *J. Am. Chem. Soc., 124,* **2002**, 4556.

[9] D. Zhao, J. Feng, Q. Huo, N. Melosh, G. H. Fredrickson, B. F. Chmelka, G. D. Stucky, *Science, 279,* **1998**, 548.

[10] S. Shen, Y. Li, Z. Zhang, J. Fan, B. Tu, W. Zhou, D. Zhao, *Chem. Commun*., **2002**, 212.

[11] X. Liu, B. Tian, C. Yu, F. Gao, S. Xie, B. Tu, R. Che, L.-M. Peng, D. Zhao, *Angew. Chem., Int. Ed.,* 41, **2002**, 3876.

[12] K. Moller, T. Bein, *Chem. Mater.,* 10, **1998**, 2950.

[13] G.A. Ozin, C. Gil, *Chem. Rev.,* 89, **1989**, 1749.

[14] M.E. Davis, R.F. Loba, *Chem. Mater.,* 4, **1992**, 756.

[15] X.S. Zhao, G. Q. Lu, G. J. Millar, *Ind. Eng. Chem. Res.,* 35, **1996**, 2075.

[16] J.S. Beck, J.C. Vartulli, W.J. Roth, M.E. Leonowicz, C.T. Kresge, K.D. Schmitt, C.T.W. Chu, D.H. Olson, E.W. Sheppard, S.B. McCullen, J.B.Higgins, J.L. Schlenker, *J. Am. Chem. Soc.,* 114, **1992**, 10834.

[17] M. Dubois, Th. Gulik-krzywicki, B. Cabane, *Langmuir,* 9, **1993**, 673.

[18] J.C. Vartulli, K.D. Schmitt, C.T. Kresge, W.J. Roth, M.E. Leonowicz, S.B. McCullen, S.D. Hellring, J.S. Beck, J.L. Schlenker, D.H. Olson, E.W. Sheppard, *Chem. Mater.,* 6, **1994**, 2317.

[19] A. Corma, A. Martinez, *Adv. Mater.*, 7, **1995**, 137.

[20] C. Huber, K. Moller, T. Bein, *J. Chem. Soc., Chem. Commun.*, **1994**, 2619.

[21] C. F. Cheng, H. He, W. Zhou, J. Klinowski, *Chem. Phys. Lett.,* 244, **1995**, 117.

[22] C-Y. Chen, S.L. Burkett, H-X. Li, M.E. Davis, *Micropor. Mater.*, 2, **1993**, 27.

[23] G.D. Stucky, A. Monnier, F. Schuth, Q. Huo, D.I. Margolese, D. Kumar, R.S. Maxwell, M. Krishnamurthy, P. Petroff, A. Firouzi, M. Janicke, B.F. Chmelka, *Mol. Cryst. Liq. Cryst.*, 240, **1994**, 187.

[24] S. Inagaki, Y. Fukushima, K. Kuroda, *J. Chem. Soc., Chem. Commun.*, **1993**, 680.

[25] A. Firouzi, D. Kumar, L. M. Bull, T. Besier, P. Sieger, Q. Huo, S. A. Walker, J. A. Zasadzinski, C. Glinka, J. Nicol, D. I. Margolese, G. D. Stucky, B. F. Chmelka, *Science*, 267, **1995**, 1138.

[26] A. Monnier, F. Schuth, Q. Huo, D. Kumar, D.I. Margolese, R.S. Maxwell, G.D. Stucky, M. Krishnamurthy, P. Petroff, A. Firouzi, M. Janicke, B.F. Chmelka, *Science*, 261, **1993**, 1299.

[27] A. Firouzi, F. Atef, A. G. Oertli, G. D. Stucky, B. F. Chmelka, *J. Am. Chem. Soc.,* 119, **1997**, 3596.

[28] Q. Huo, D.I. Margolese, U. Ciesla, P. Feng, P. Sieger, R. Leon, P. Petroff, F.Schuth, G.D. Stucky, *Nature*, 368, **1994**, 317.

[29] Q. Huo, D.I. Margolese, U. Ciesla, D.G. Demuth, P. Feng, T.E. Gier, P.Sieger, A. Firouzi, B.F. Chmelka, G.D. Stucky, *Chem. Mater.*, 6, **1994**, 1176.

[30] P.T. Tanev, T.J. Pinnavaia, *Chem. Mater.*, 8, **1996**, 2068.

[31] P.T. Tanev, T.J. Pinnavaia, *Science,* 271, **1996**, 1267.

[32] C.G. Wu, T. Bein, *J. Chem. Soc., Chem. Commun.*, **1995**, 925.

[33] N. Ulagappan, C.N.R. Rao, *Chem. Commun.*, **1996**, 2759.

[34] D. Khushalani, A. Kuperman, G. A. Ozin, K. Tanaka, J. Garces, M. M. Olken, A. Kuperman, *Adv. Mater.*, 7, **1996**, 842.

[35] D. M. Antonelli, J. Y. Ying, *Angew. Chem. Int. Ed.*, 35, **1996**, 426.

[36] T. Sun, J. Y. Ying, *Nature,* 389, **1997**, 704.

[37] H. Yang, N. Coombs, G. A. Ozin, *Nature,* 386, **1997**, 692.

[38] S. Schacht, Q. Huo, I. G. V. Martin, G. D. Stucky, F. Schuth, *Science*, 273, **1996**, 768.

[39] Q. Huo, D. Zao, J. Feng, K. Weston, S.K. Burratto, G.D. Stucky, S. Schacht, F. Schuth, *Adv. Mater.*, 9, **1997**, 974.

[40] H. Yang, N. Coombs, I. Sokolov, G. A. Ozin, *Nature*, 381, **1996**, 589.

[41] H. Yang, A. Kuperman, N. Coombs, S. M. Afara, G. A. Ozin, *Nature*, 379, **1996**, 703.

[42] I. A. Aksay, M. Trau, S. Manne, I. Honma, N. Yao, L. Zhou, P. Fenter, P. M. Eisenberger, S. M. Gruner, *Science*, 273, **1996**, 892.

[43] M. Ogawa, *Chem. Commun.,* **1996**, 1149.

[44] Q. Huo, J. Feng, F. Schuth, G.D. Stucky, *Chem. Mater.*, 9, **1997**, 14.

[45] G.S. Attard, J.C. Glyde, C.G. Goltner, *Nature*, 378, **1995**, 366.

[46] M. T. Anderson, J. E. Martin, J. G. Odinek, P. P. Newcomer, J. P. Wilcoxon, *Micropor. Mater.*, 10, **1997**, 13.

[47] S. S. Kim, W. Zhang, T. J. Pinnavaia, *Science*, 282, **1998**, 1302.

[48] F. Kleitz, W. Schmidt, F. Schüth, *Micropor. Mesopor. Mater.*, 65, **2003**, 1.

[49] A. Doyle, B. K. Hodnett, *Micropor. Mesopor. Mater.*, 58, **2003**, 251.

[50] W.J. Hunks, G.A. Ozin, *Adv. Fun. Mater.*, 15, **2005**, 259.

[51] A. Stein, B.J. Melde, R.C. Schroden, *Adv. Mater.*, 12, **2000**, 1403.

[52] A.P. Wight, M.E. Davis, *Chem. Rev.*, 102, **2002**, 3589.

[53] X. Feng, G. E. Fryxell, L. -Q. Wang, A. Y. Kim, J. Liu, K. M. Kemner, *Science*, 276, **1997**, 923.

[54] D. E. De Vos, M. Dams, B. F. Sels, P. A. Jacobs, *Chem. Rev.*, 102, **2002**, 3615.

[55] P.M. Price, J.H. Clarck, D.J. Macquarrie, *J. Chem. Soc., Dalton Trans.,* **2000**, 101.

[56] K. Moller, T. Bein, *Stud. Surf. Sci. Catal.*, 117, **1998**, 53.

[57] J. Liu, X. Feng, G. E. Fryxell, L. -Q. Wang, A. Y. Kim, M. Gong, *Adv. Mater.*,

10, **1998**, 161.

[58] K. K. Unger, Porous Silica – Its Properties and Use as Support in Column Liquid Chromatography, Vol. 16, Elsevier, Amsterdam, **1979**.

[59] L. Mercier, T. J. Pinnavaia, *Environ. Sci. Tech.*, 32, **1998**, 2749.

[60] T. Kimura, S. Saeki, Y. Sugahara, K. Kuroda, *Langmuir*, 15, **1999**, 2794.

[61] J. S. Beck, D. C. Calabro, S. B. McCullen, B. P. Pelrine, K. D. Schmitt, J. C. Vartuli, *Method for Functionalizing Synthetic Mesoporous Crystalline Material,* Mobil Oil Corporation, USA, **1992**.

[62] R. Anwander, I. Nagl, M. Widenmeyer, G. Engelhardt, O. Groeger, C. Palm, T. Roser, *J. Phys. Chem. B*, 104, **2000**, 3532.

[63] M. H. Lim, C. F. Blanford, A. Stein, *J. Am. Chem. Soc.*, 119, **1997**, 4090.

[64] M. H. Lim, C. F. Blanford, A. Stein, *Chem. Mater.*, 10, **1998**, 467.

[65] W. M. van Rhijn, D. E. De Vos, B. F. Sels, W. D. Bosaert, P. A. Jacobs, *Chem. Commun.,* **1998**, 317.

[66] D. Margolese, J.A. Melero, S.C. Christiansen, B.F. Chmelka, G.D. Stucky, *Chem. Mater.,* 12, **2000**, 2448.

[67] J. H. Clark, D. J. Macquarrie, *Chem. Commun.*, **1998**, 853.

[68] D. Brunel, *Micropor. Mesopor. Mater.*, 27, **1999**, 329.

[69] P. Sutra, D. Brunel, *Chem. Commun.*, **1996**, 2485.

[70] M. H. Lim, A. Stein, *Chem. Mater.*, 11, **1999**, 3285.

[71] D. S. Shephard, W. Zhou, T. Maschmeyer, J. M. Matters, C. L. Roper, S. Parsons, B. F. G. Johnson, M. J. Duer, *Angew. Chem. Int. Ed.*, 37, **1998**, 2719.

[72] F. De Juan, E. Ruiz-Hitzky, *Adv. Mater.,* 12, **2000**, 430.

[73] V. Antochshuk, M. Jaroniec, *Chem. Commun.,* **1999**, 2373.

[74] C. Sanchez, F. Ribot, *New. J. Chem.* 18, **1994**, 1007.

[75] S. L. Burkett, S. D. Sims, S. Mann, *Chem. Commun.,* **1996**, 1367.

[76] S. D. Sims, S. L. Burkett, S. Mann, *Mater. Res. Soc. Symp. Proc.* 8, **1996**.

[77] D. J. Macquarrie, *Chem. Commun.,* **1996**, 1961.

[78] Q. Huo, D. I. Margolese, G. D. Stucky, *Chem. Mater.,* 8, **1996**, 1147.

[79] P. Mukherjee, S. Laha, D. Mandal, R. Kumar, *Stud. Surf. Sci. Catal.,*129, **2000**, 283.

[80] S. R. Hall, C. E. Fowler, B. Lebeau, S. Mann, *Chem. Commun.,* **1999**, 201.

[81] F. Babonneau, L. Leite, S. Fontlupt, *J. Mater. Chem.,* 9, **1999**, 175.

[82] V. Goletto, V. Dagry, F. Babonneau, *Mater. Res. Soc. Symp. Proc.,* 576, **1999**, 229.

[83] L. Mercier, T. J. Pinnavaia, *Chem. Mater.,* 12, **2000**, 188.

[84] M. Koya, H. Nakajima, *Stud. Surf. Sci. Catal.,* 117, **1998**, 243.

[85] R. Richer, L. Mercier, *Chem. Commun.,* **1998**, 1775.

[86] J. Brown, R. Richer, L. Mercier, *Micropor. Mesopor. Mater.,* 37, **2000**, 41.

[87] C.E. Fowler, S.L. Burkett, S. Mann, *J. Chem. Soc., Chem. Commun.,* **1997**,1769.

[88] D.J. Macquarrie, D.B. Jackson, *J. Chem. Soc., Chem. Commun.,* **1997**, 1781.

[89] X.S. Zhao, G.Q. Lu, A.K. Whittakar, G.J. Millar, *J. Phys. Chem. B*, 101, **1997**, 6525.

[90] K. A. Koyano, T. Tatsumi, Y. Tanaka, S. Nakata, *J. Phys. Chem. B*, 101, **1997**, 9436

[91] J. Patarin, *Angew. Chem. Int. Ed.,* 43, **2004**, 1.

[92] S. Hitz, R. Prins, *J. Catal.,* 168, **1997**, 194.

[93] H. Lee, S. I. Zones, M. E. Davis, *Nature,* 425, **2003**, 385.

[94] (a) N. Husing, *Angew. Chem. Int. Ed.,* 43, **2004**, 3216. (b) C-H. Lee, T-S. Lin, CY. Mou, *J. Phys. Chem. B,* 107, **2003**, 2543. (c) C. D. Nunes, M. Pillinger, A.A. Valente. J. Rocha, A. D. Lopes, I. S. Goncalves, *Eur. J. Inorg. Chem.,* **2003**, 3870. (d) L. L. Welbes, A. S. Borovik, *Acc. Chem. Res.,* 38, **2005**, 765. (e) A. Taguchi, F. Schuth, *Microporous Mesoporous Mater.,* 77, **2004**, 1. (f) C. T.Fischel, R. J. Davis, J. M. Garcer, *J. Catal.,* 163, **1996**, 141. (g) R. Ryoo, C. H. Ko, J. M. Kim, R. Howe, *Catal. Lett.,* 37, **1996**, 29.

[95] (a) J. Jamis, J. R. Anderson, R. S. Dickson, E. M. Campi, W. R. Jackson, *J. Organomet. Chem.,* 627, **2001**, 37. (b) K. Mukhopadhyay, B. R. Sarkar, R. V.Chaudhari, *J. Am. Chem. Soc.,* 124, **2002**, 9692. (c) C. Baleizao, B. Gigante,

M.J. Sabatier, H. Garcia, A. Corma, *Appl. Catal. A. Gen.,* 288, **2002**, 279. (d) S.Xiang, Y. Zhang, Q. Xin, C. Li, *Angew. Chem. Int. Ed.,* 41, **2002**, 821. (e) A. Poppl, P. Baglioni, L. Kevan, *J. Phys. Chem.,* 99, **1995**, 14156. (f) W.Bohlmann, K. Schandert, A. Poppl, H. C. Semmelhack, *Zeolites,* 19, **1997**, 297.

[96] D. J. Cole Hamilton, *Science*, 299, **2003**, 1702.

[97] (a) W. F. Maier, J. A. Marten, S. Klein, J. Heilmann, R. Parton, K.Vercruysse, P. A. Jacobs, *Angew. Chem. Int. Ed.,* 35, **1996**, 180. (b) N. A. Herron, *Inorg. Chem.,* 25, **1986**, 4714.

[98] C. A. McNamara, M. J. Dixon, M. Bradley, *Chem. Rev.,* 102, **2002**, 3275.

[99] K. Tanabe, T. Yamaguchi, *Stud. Surf. Sci. Catal.*, 44, **1989**, 99.

[100] K. Tanabe M. M. Ono, H. Hattori, *Stud. Surf. Sci. Catal.*, 51, **1989**, 219.

[101] B.H. Davis, R. A. Keogh, R. Srinivasan, *Catal. Today*, 20, **1994**, 219.

[102] X. Song, A. Sayari, *Catl. Rev.-Sci. Eng.,* 38, **1996**, 329.

[103] K. Tanabe, T. Yamaguchi, *Catal.Today*, 20, **1994**, 185.

[104] D.M. Antonelli, J.Y. Ying, *Angew. Chem., Int. Ed. Engl.,* 34, **1995**, 2014.

[105] H. Yoshitake, T. Sugihara, T. Tatsumi, *Chem. Mater.,* 14, **2002**, 1023.

[106] J.A. Knowles, M.J. Hudson, *J. Chem. Soc., Chem. Commun.* **1995**, 2083. *J. Mater. Chem.*, 6, **1996**, 89.

[107] U. Ciesla, S. Schacht, G.D. Stucky, K.K. Unger, F. Schuth, *Angew. Chem.* Int. Ed. Engl., 35, **1996**, 541.

[108] U. Ciesla, M. Froba, G.D. Stucky, K.K. Unger, F. Schuth, *Chem. Matet.,***1999**, 11, 227.

[109] J.L. Blin, R. Flamant, B.L. Su, *Inter. J. Inorg. Mater.*, 3, **2001**, 959.

[110] N. Ulagappan, V.N. Raju, C.N.R. Rao, *Chem. Commun.,* **1996**, 2243.

[111] D.M. Antonelli, *Adv. Mater.*, 11, **1999**, 487.

[112] J. S. Reddy, A. Sayari, *Catal. Lett.*, 38, **1996**, 219.

[113] E. Zhao, S.E. Hardcastle, G. Pacheco, A. Garcia, A.L. Blumenfeld, J.J.Fripiat, *Micropor. Mesopor. Mater.,* 31, **1999**, 9.

[114] G. Pacheco, E. Zhao, A. Garcia, A. Sklyarov, J. Fripiat, *Chem. Commun.*, **1997**,

491.

[115] M.S. Wong, J.Y. Ying, *Chem. Mater.*, 10, **1998**, 2067.

[116] Y.Y. Huang, T.J. McCarthy, W.M.H. Sachtlet, *Appl. Catal. A: Gen.*, 148, **1996**, 135.

[117] H-R. Chen, J-L. Shi, W-H. Zhang, M-L. Ruan, D-S. Yan, *Micropor. Mesopor. Mater.,* 47, **2001**, 173.

[118] D.J. McIntosh, R.A. Kydd, *Micropor. Mesopor. Mater.*, 37, **2000**, 281.

[119] G. Larsen, E. Lotero, M. Nabity, L.M. Petkovic, D.S. Shobe, *J. Catal.,* 164, **1996**, 246.

[120] Lee, D.L. Lu, J.N. Kondo, K. Domen, *J. Am. Chem. Soc.,* 124, **2002**, 11256.

[121] D.M. Antonelli, J.Y. Ying, *Chem. Mater.,* 8, **1996**, 874.

[122] S.A. Bagshaw, T.J. Pinnavaia, *Angew. Chem. Int. Ed. Engl.,* 35, **1996**, 1102.

[123] P. Liu, J. Liu, A. Sayari, *Chem. Commun.,* **1997**, 577.

[124] K.G. Servin, T.M. AbdeFattah, T.J. Pinnavaia, *Chem. Commun.,* **1998**, 1471.

[125] Z. Tian, W. Tong, J. Wang, N. Duan, V.V. Krishnan, S.L. Suib, *Science,* 276, **1997**, 926.

[126] P. Yang, D. Zhao, D.I. Margolese, B.F. Chmelka, G.D. Stucky, *Nature*, 396, **1998**, 152.

[127] J.B. Miller, E.I. Ko, *Catal. Today,* 35, **1997**, 269.

[128] M. Chidambaram, D. Curulla-Ferre, A.P. Singh, B.G. Anderson, *J. Catal*. 220, **2003**, 442.

[129] C.J. Brinker, G.W. Xcherer, *Sol-gel Science,* academic Press, New York, **1990**.

[130] G. D. Yadav, J. J. Nair, *Mircopor. Mesopor. Mater.*, 33, **1999**, 1.

[131] V.I. Parvulescu, H. Bonnemann, V. Parvulescu, B. Endruschar, A.Ch.W. Rufinska, B. Tesche, G. Poncelet, *Appl. Catal. A: Gen.,* 214, **2001**, 273.

CHAPTER-2

SYNTHESIS METHODOLOGIES AND CHARACTERIZATION TECHNIQUES

2.1. INTRODUCTION

After the discovery of M41S family of mesoporous silicates and aluminosilicate materials by Mobil scientists in 1992 [1, 2] mesoporous materials has become the most popular member of the group due to their unique textural features and simple synthesis procedures. The most interesting feature of mesoporous materials are its regular pore system, which consists of a hexagonal array of unidimentional or parallel mesopore channels. Such pore structures are known to serve as ideal hosts where the mesopore channels assist in the transport of reactants or products without much diffusional resistance, and at the same time they provide a large surface area to enhance the number of the reaction sites. The pore diameter of mesoporous materials can be varied systematically by use of surfactants with different chain lengths and pore expanders like trimethyl benzene (TMB).

The catalytic properties of the mesoporous materials can be adjusted by the incorporation of different metals into the mesoporous framework [3-5]. Further, the diversity in the catalytic properties can be broadened by the grafting of organosilanes which contain organic functional groups onto the internal pore surfaces [6-8] or incorporating them during the synthesis process. An advantage of the organic-inorganic hybrid mesoporous materials is that they do not swell or dissolve in organic solvents and they have other advantages such as their superior mechanical and thermal stabilities [9-11]. Moreover, the leaching of active sites can also be avoided as the organic moieties are covalently attached to inorganic supports.

In the preceding chapter, the synthesis procedure of various mesoporous supports such as MCM-41, SBA-15, mesoporous zirconia (Zr-TMS) and their surface modification by different routes have been reviewed. This chapter will present the experimental data regarding (i) the synthesis of mesoporous MCM-41, SBA-15, mesoporous Zr-TMS (ii) surface modification of these materials by different organic functional groups, *viz*., chloropropyl trimethoxy silane, chiral ligands, benzyl alcohol, chlorosulfonic acid etc., through grafting and co-condensation routes, and (iii) the different characterization technique used to confirm the proper heterogenization of these groups over mesoporous support.

2.2. MATERIALS

2.2.1. Primary Chemicals

1. Zirconium (IV) butoxide [Zr $(C_4H_9O)_4$, 80 wt% solution in 1-butanol, Aldrich, USA]
2. Tetramethyl ammonium hydroxide [$(CH_3)_4$-N-OH, TMAOH, 25 wt% aqueous solution, Loba Chemie, India]
3. N-cetyl-N, N, N trimethyl ammonium bromide [$C_{16}H_{33}$-N-$(CH_3)_3$Br, CTMABr, 25 wt% aqueous solution, Loba Chemie, India]
4. Acetyl acetone [$CH_3COCH_2COCH_3$, acac, 98%, Merck, India]
5. Benzyl alcohol [$C_6H_5CH_2OH$, 99%, Lancaster, UK]
6. Ethoxytrimethylsilane [C_2H_5O-Si-$(CH_3)_3$, ETMS, 98%, Sigma-Aldrich, USA]
7. Chlorosulphonic acid [Cl-SO_3H, CSA, 98%, Spectrochem, India]
8. P123 [EO-PO-EO, MW~ 5800, Sigma-Aldrich, USA]
9. 3-(mercaptopropyl) trimethoxysilane [$(CH_3O)_3$-Si-$(CH_2)_3SH$, 3-MPTS, 95%, Alrdich, USA]
10. Sodium hydroxide [NaOH, 97%, Merck, India]
11. Metal triflates (Zn, Ce, La & Y)

2.2.2. Solvents

1. Cyclohexane [C_6H_{12}, 99%, Thomas Baker, India]
2. Benzene [C_6H_6, 99.7%, S.d. Fine, India]
3. Acetone [CH_3COCH_3, 99.5%, S.d. Fine, India]
4. Dry toluene [C_6H_5-CH_3, 99.5%, Thomas Baker, India]
5. Dichloromethane [CH_2Cl_2, 99.5%, Merck, India]
6. Chloroform [$CHCl_3$, Merck, India]
7. Diethyl ether [C_2H_5-O-C_2H_5, 98%, Sisco, India]
8. Methanol [CH_3OH, 99.8%, Merck, India]
9. Hydrochloric acid [HCl, 35%, Merck, India]

2.2.3. Chemicals used for catalytic reactions

1. Styrene [C_8H_8, 99 %, Aldrich, USA]
2. Thioanisole [C_7H_8S, 99 % Aldrich, USA]
3. Naphthalene [$C_{10}H_8$, 99 %, S.d. Fine-Chem. Ltd, India]
4. Resorcinol [$C_6H_6O_2$, 99 %, S.d. Fine-Chem. Ltd, India]
5. 1-Naphthol [$C_{10}H_8O$, 99 % Aldrich, USA]
6. 3-Methoxy phenol [$C_7H_8O_2$, 96 %, S.d. Fine-Chem. Ltd, India]
7. Acetone [CH_3COCH_3, 99.5%, S.d. Fine-Chem. Ltd, India]
8. Nitrobenzene [$C_6H_5NO_2$, 98 %, Sisco Research Laboratory, India]
9. Ethylacetoacetate [$CH_3COCH_2COOC_2H_5$, 98 %, Merck, India]
10. Ethylene glycol [$HOCH_2$-CH_2OH, 99 %, S.d. fine-Chem. Ltd, India]
11. *p*-toluoyl chloride [C_7H_7COCl, 98 %, Aldrich, USA]
12. Glycerol [$HOCH_2$-$CHOH$-CH_2OH, 99+ %, Aldrich, USA]
13. *p*-formaldehyde [$(CH_2O)n$, 95 %, Thomas Baker, India]

2.3. SYNTHESIS

2.3.1. Synthesis of parent and organo-functionalized MCM-41

The Si-MCM-41 was prepared from the gel with the following composition. SiO_2: CTMABr: NaOH: H_2O 1: 0.19:0.4:78. In a typical synthesis, cetyltrimethylammonium bromide (CTMABr) was added to the solution of NaOH in H_2O, under stirring and the mixture was further stirred for 1h. To this mixture, calculated amount of fumed silica was added slowly. The gel mixture was stirred for 6h and pH was adjusted to 10.7-10.9 by addition of 0.1 M HCl solution. Finally the mixture was transferred into a Teflon-lined autoclave and kept at 100° C under static conditions for 72 h. The solid material obtained was then filtered, washed well with distilled water till the filtrate shows a neutral pH, and then air-dried. The surfactant of the as-synthesized mesoporous sample was removed by calcination in air at 540° C for 10h.

Surface modification of MCM-41 material was achieved by a post synthesis grafting method. One gram of calcined MCM-41 material was suspended in 50 mL of dry

toluene and allowed to stir for 15 min at room temp. Then 2.5 mmol of chloropropyl trimethoxy silane (3-ClPTS) was added slowly and then the mixture was stirred overnight at reflux temperature under inert atmosphere. The material was filtered, washed with toluene, soxhlet extracted with dichloromethane (DCM) for 12 h, and then dried under vacuum. The material obtained is designated as Cl-MCM-41. The free –OH groups present in Cl-MCM-41 were protected by adding 1.5 mmol of methyl trimethoxy silane to a stirred suspension of 1g of Cl-MCM-41 in dry toluene (50mL), followed by stirring for 12 h at reflux temp under inert atmosphere. Then the material was filtered, washed with toluene and soxhlet extracted with DCM for 24 h. The final material was named –OH protected Cl-MCM-41.

2.3.2. Grafting of (1S, 2S)-N, N'-bis-pyridin-2-ylmethyl-cyclohexane-1, 2-diamine (L_2Me) ligand inside the Cl-MCM-41

The ligand, L_2Me, was introduced into the inner surfaces of MCM-41 by adding a solution of 0.1g of L_2Me in 10 mL of dry CH_2Cl_2 to a stirred suspension of –OH protected Cl-MCM-41 (1g) in dry toluene (30 ml). This mixture was refluxed for 24 h in inert atmosphere, filtered, and washed with toluene and then with CH_2Cl_2 followed by soxhlet extraction, with 1:1 mixture of DCM: diethyl ether for about 24h. The final material is called as L_2Me-MCM-41. The final proportion of the anchored ligand over Cl-MCM-41 is 7% wt. of the solid.

2.3.3. Synthesis of siliceous SBA-15

The synthesis of mesoporous SBA-15 was carried out hydro thermally under the autogeneous pressure of an autoclave. The polymer surfactant P123 was used as a template and hydrochloric acid served as a mineralizer. The following was the gel composition.

0.043 TEOS: 4.4 g P_{123} M_{avg} = 5800 [EO_{20}-PO_{70}-EO_{20}]: 8.33 H_2O: 0.24 HCl

Typically, 4.4 g of tri block co-polymer dispersed in 30 g distilled water was stirred for 1.5 h. To the resultant solution, 120 g of 2M HCl was added under stirring and

the stirring was continued for 2 h. Finally 9 g of TEOS was added drop wise and the mixture was maintained at 40 °C for 24 h with continuous stirring. The mass was submitted to a hydrothermal treatment (100 °C, 48 h) under static condition. The precipitate was filtered, washed with distilled water, dried in an oven (90 °C, 12 h) and then calcined in air (500 °C, 6 h) to remove the template completely.

The catalysts were prepared by soaking of calcined SBA-15 sample in acetonitrile solution of a metal triflate powder, accompanied with continuous stirring for 8-10 h. The excess of acetonitrile was evaporated to dryness under reduced pressure, followed by complete drying at 120 °C. The functionalized samples are designated in the text as Zn-Tf (30)/SBA, where the number in the parentheses represents the triflate loading in mol %.

2.3.4. Synthesis of Zr-TMS material

The synthesis of Zr-TMS was carried out using the following gel composition and procedure:

0.1 Zr $(OC_4H_9)_4$:0.05 acac: 0.025 CTMABr: 0.02 TMAOH: 8.5 H_2O

In a typical synthesis of Zr-TMS, zirconium (IV) butoxide and acetyl acetone was mixed well by stirring at room temperature. Then the mixture was slowly added to an aqueous solution of CTMABr and TMAOH, which are well dissolved in required amount of water. After further stirring the resulting synthesis gel was refluxed at 90 °C for about 50 h. The solid product was recovered, washed with deionised water and acetone, and dried. The surfactant was removed from the synthesized material by solvent extraction under reflux condition. The solid product was recovered by filtration, washed with deionised water and acetone, and dried. The procedure adopted here is the modified procedure of already reported by Hudson and Knowles [12].

2.3.5. Synthesis of Zr-TMS-BSA catalysts

Functionalization of benzyl alcohol over Zr-TMS was carried out by etherification reaction using cyclohexane as solvent at 80 °C for 10 h. To protect the unloaded hydroxyl

groups, after modification with benzyl alcohol, desired amount of material was degassed at 80 °C for 2 h and dry toluene was added. Then an excess of ethoxytrimethylsilane was added and the suspension was refluxed at 70 °C under nitrogen atmosphere for 12 h. Further, sulphonation of the resulting material was done with the appropriate amount of chlorosulphonic acid using chloroform as solvent at 70 °C for 3 h. Thus the material obtained was washed with chloroform and soxhlet extraction was done with a mixture of 1:1 diethyl ether and dichloromethane and dried at 50 °C for 6 h.

2.4. PHYSICOCHEMICAL CHARACTERIZATION

The inorganic–organic hybrid mesostructured materials can be characterized by various techniques, which provide important information about different physicochemical features. The most extensively used techniques can be categorized into the following.

1. Spectroscopic techniques:

(a) Powder X-ray diffraction (XRD), (b) Fourier transform infrared (FTIR) spectroscopy, (c) FT-Raman spectroscopy, (d) Solid state nuclear magnetic resonance (NMR) spectroscopy, (e) X-ray photoelectron spectroscopy (XPS), (f) Atomic absorption and emission spectrometry (AAS and AES).

2. Microscopic techniques:

(a) Scanning electron microscopy (SEM), (b) Transmission electron microscopy (TEM).

3. Volumetric techniques:

(a) Porosity measurements by nitrogen (N_2) adsorption (BET method), (b) Acidity measurements by pyridine or ammonia (NH_3) adsorption and *insitu pyridine* IR.

4. Gravimetric techniques:

(a) Thermo gravimetric analyses (TGA), (b) Differential thermal analysis (DTA).

2.4.1. X-Ray diffraction

It is well recognized that X-ray diffraction, based on wide-angle elastic scattering of X-rays, has been the single most important tool to determine the structure of the materials characterized by long-range ordering. The X-ray diffraction patterns are

obtained by measurement of the angles at which an X-ray beam is diffracted by the sample. Bragg's equation relates the distance between two *hkl* planes (*d*) and the angle of diffraction (2θ) as: $n\lambda = 2d\sin\theta$, where λ = wavelength of X-rays, *n* = an integer known as the order of reflection (*h*, *k* and *l* represent Miller indices of the respective planes) [13]. From the diffraction patterns, the uniqueness of mesoporous structure [14], phase purity [15], degree of crystallinity and unit cell parameters of the semi crystalline hybrid materials can be determined.

The identification of phase is based on the comparison of the set of reflections of the sample with that of pure reference phases distributed by International Center for Diffraction Data (ICDD). Unit cell parameter (a_0) of a cubic lattice can be determined by the following equation: $a_0 = d_{hkl}\sqrt{(h^2 + k^2 + l^2)}$, where *d* = distance between two consecutive parallel lattice planes having Miller indices *h*, *k* and *l* [13].

X-ray diffraction broadening analysis has been widely used to characterize supported metal crystallites in the nanoscale. The average size of the nanoparticles can be estimated using the Debye-Scherrer equation: $D = k\lambda / \beta\cos\theta$, where *D* = thickness of the nanocrystal, *k* is a constant, λ = wavelength of X-rays, β = width at half maxima of (111) reflection at Bragg's angle 2θ [16]. In this study, all the synthesized catalysts were characterized by a Rigaku Miniflex instrument using Cu K_α radiation (30 kV, 15 mA), λ=1.5404 Å between 1.5 to 60° (2θ) with a scan rate of 4°/min.

2.4.2. Chemical composition by CHN-S analysis

Analysis of the organic content, carbon and sulfur present in the catalysts was estimated using a Carlo-Erba CHN analyzer (EA1108 Elemental Analyzer).

2.4.3. Fourier transforms infrared spectroscopy

Fourier transforms infrared (FT-IR) spectroscopy deals with the vibration of chemical bonds in a molecule at various frequencies depending on the elements and types of bonds. After absorbing electromagnetic radiation the frequency of vibration of a bond increases leading to transition between ground state and several excited states. The

energy corresponding to these transitions corresponds to the infrared region (4000–400 cm^{-1}) of the electromagnetic spectrum. The term Fourier transform (FT) refers to a recent development in the manner in which the data are collected and converted from an interference pattern to an infrared absorption spectrum that is like a molecular "fingerprint" [17].

In the case of porous zirconia, the FTIR spectra in the 750–750 cm^{-1} region provides information about the structural details including isomorphous substitution in framework, whereas the bands in the 3000–4000 cm^{-1} region allows to determine different Brönsted and Lewis acid sites [18]. In this study, all the synthesized catalysts FT-IR spectra were obtained in a range of 400 to 4000 cm^{-1} on a Shimadzu FTIR 8201 PC using a Diffuse Reflectance scanning disc technique.

2.4.4. FT-Raman spectroscopy

In contrast to infrared spectroscopy, where we have been concerned with the absorption of infrared light, Raman spectroscopy depends on the frequency of the light scattered by molecules as they undergo rotations and vibrations. When monochromatic light of frequency υ_0 is directed at a cell containing a dust-free transparent substance, most of the light passes through unaffected. Some of the light, however (~0.1%) is scattered by the sample molecules in all directions. The scattered radiation contains photons which have the same frequency υ_0 as the incident light (elastic scattering), but in addition the emergent radiation contains other frequencies (due to inelastic scattering) such as $(\upsilon_0-\upsilon_1)$ and $(\upsilon_0+\upsilon_1)$. The lines of lower frequency than the incident light $(\upsilon_0-\upsilon_1)$ are known as stokes lines, while the high-frequency lines $(\upsilon_0+\upsilon_1)$ are termed as anti-stokes lines. Normally, an intense monochromatic source of light in the visible region is employed as the incident or exciting radiation. Raman scattered light is due to rotations and vibrations of the compounds under investigation. Since the wavenumber position of the exciting line is approximately 20000 cm^{-1}, the Raman scattered light will have frequencies which are displaced from 20000 cm^{-1} by amounts which lie somewhere in the range ±10-4000cm^{-1}. The exact wavenumber displacements, $\Delta\upsilon$, will depend upon the

rotational and vibrational energies of the particular compound causing the Raman scattering. The same displacement will occur on the either side of the exciting line.

Raman spectra may be obtained from solids, liquids, gases and solutions. All Raman spectrometers consist basically of four units- a source, sample optics, a monochromator, and a detector/electronics/recorder system [19, 20]. In the present work a Bruker RFS/100S FT-Raman spectrometer. A Nd-YAG laser (1064 cm^{-1}; 50 mW) was used as an excitation source.

2.4.5. Cross-polarization magic angle spinning NMR spectroscopy

Nuclear magnetic resonance (NMR) spectroscopy is one of the most powerful tools to investigate structure and dynamics of a molecular system in liquid phase. Atomic nuclei consisting of odd number of protons and/or neutrons possessing a nuclear spin $I \neq 0$ and consequently a magnetic moment $\mu = \gamma\hbar I$ (γ = gyromagnetic ratio), when placed in a magnetic field of strength B_0, Zeeman interaction results in quantized orientations of the nuclear magnetic moments [21]. The nucleus can adopt $2I + 1$ Eigen states with energies $E(m) = -m\gamma\hbar B_0$, where m = (I, I–1,…., –I). Transitions between neighboring energy states ($\Delta m = \pm 1$) can be induced by electromagnetic radiation (energy $E = h\nu$) of frequency $\nu_0 = \gamma B_0/2\pi$.

The chemical shift interaction arises from secondary local magnetic fields induced by the interaction of the electrons surrounding the nucleus. The induced local field opposes B_0 and hence shields the nucleus under observation. The shielding is spatially anisotropic due to the nonspherical electron distribution around the nucleus [22].

With the advent of sophisticated solid-state NMR techniques, it has become possible to obtain NMR spectra of solids with spectral resolution comparable to that of liquids [23]. Modern high-resolution solid-state NMR spectroscopy allows to elucidate the chemical and structural environment of several atoms (*e.g.* ^{13}C, ^{27}Al, ^{29}Si, ^{31}P, ^{51}V *etc*.) in a solid matrix like that of porous materials [24]. The most popular technique to get high-resolution NMR spectra with narrow line width is the magic angle spinning

(MAS), where the solid sample is fast rotated about an axis inclined at a "magic" angle θ = 54°44' to the direction of B_0 [25].

Cross-polarization (CP) technique does not affect the line width of the spectra, but is applied to improve the sensitivity, *i.e.*, the signal to noise ratio (SNR) of the spectra of nuclei with low natural abundance (*e.g.* ^{13}C, ^{29}Si, ^{31}P *etc.*), and to monitor the spatial proximity of nuclei [25]. CP involves indirect excitation of the less abundant nucleus through magnetization transfer from an abundant spin system (*e.g.* ^{1}H).

Bruker DRX-500 and DSX-300 NMR spectrometers were used. The resonance frequencies of ^{29}Si and ^{13}C were 59.6 and 75.5 MHz, respectively. The chemical shifts were determined using tetraethyl orthosilicate (δ=82.4 ppm from TMS) and adamantane (δ =28.7 ppm from TMS) as the reference compounds for ^{29}Si and ^{13}C, respectively.

2.4.6. X-Ray photoelectron spectroscopy

XPS is based on the photoelectric effect. Routinely used X-ray sources are Mg Kα (*hv* = 1253.6 eV) and Al Kα (*hv* = 1486.3 eV). In XPS one measures the intensity of photoelectrons N (E) as a function of their kinetic energy E_k. Because a set of binding energies is characteristic for an element, XPS can be used to analyze the composition of samples. Binding energies are not only element specific but contain chemical information as well: the energy levels of core electrons depend on the chemical state of the atom. Photoelectron peaks are labeled according to the quantum numbers of the level from which the electron originates. An electron coming from an orbital with main quantum number *n*, orbital quantum number *l* (0, 1, 2, 3,.. indicated as *s, p, d, f*,..) and spin quantum number *s* (+1/2 or –1/2) is indicated as nl_{l+s}. Almost all photoelectrons used in the laboratory XPS have kinetic energy in the range of 0.2 to 1.5 keV, and probe the outer layer of the catalyst.

X-ray photoelectron spectra (XPS) were obtained using a VG Microtech Multilab-ESCA-3000 spectrometer equipped with a twin anode of Al and Mg. All the measurements are made on as received powder samples using Mg Kα X-ray at room temperature. Base pressure in the analysis chamber was 4 x 10-10 Torr. Multichannel detection system with nine channels is employed to collect the data. The overall energy

resolution of the instrument is better than 0.7 eV, determined from the full width at half maximum of 4f7/2 core level of gold surface. The errors in all BE (binding energy) values were with in ±0.1 eV.

2.4.7. Atomic absorption and emission spectrometry

The principle of atomic absorption is based on energy absorbed during transitions between electronic energy levels of an atom. When some sort of energy is provided to an atom in ground state by a source such as a flame (temperature ranging from 2100–2800 °C), outer-shell electrons are promoted to a higher energy excited state. The radiation absorbed as a result of this transition between electronic levels can be used for quantitative analysis of metals and metalloids present in solid matrices, which have to be dissolved by appropriate solvents before analysis. The basis of quantitative analysis depends on measurement of radiation intensity and the assumption that radiation absorbed is proportional to atomic concentration. Analogy of relative intensity values for reference standards is used to determine elemental concentrations [26].

Atomic emission spectrometry (AES) is similar to atomic absorption spectrometry (AAS). In both the cases the sample must be atomized in order to obtain usable absorption spectra. However, in contrast to AAS, in AES the sample is heated at a very high temperature (8000–10000 °C), where the atoms in the sample are excited to higher energy levels. When the excited atoms are relaxed and fall back to the ground energy level, radiations are emitted. Measurement of the intensities of the emission forms the basis of quantitative determination [27]. Here, all the synthesized catalysts were studied by Varian Spectra AA220.

2.4.8. Scanning electron microscopy

Scanning electron microscopy (SEM) is an important tool for morphological characterization of mesoporous molecular sieve materials. A scanning electron microscope can generate an electron beam scanning back and forth over a solid sample. The interaction between the beam and the sample produces different types of signals

providing detailed information about the surface structure and morphology of the sample. When an electron from the beam encounters a nucleus in the sample, the resultant coulombic attraction leads to a deflection in the electron's path, known as Rutherford elastic scattering. A fraction of these electrons will be completely backscattered, reemerging from the incident surface of the sample. Since the scattering angle depends on the atomic number of the nucleus, the primary electrons arriving at a given detector position can be used to produce images containing topological and compositional information [28].

The high-energy incident electrons can also interact with the loosely bound conduction band electrons in the sample. However, the amount of energy given to these secondary electrons as a result of the interactions is small, and so they have a very limited range in the sample. Hence, only those secondary electrons that are produced within a very short distance from the surface are able to escape from the sample. As a result, high-resolution topographical images can be obtained in this detection mode [29]. Here, all the synthesized catalysts were studied by JEOL-JSM-5200 scanning microscopy.

2.4.9. Transmission electron microscopy

Transmission electron microscopy (TEM) is typically used for high resolution imaging of thin films of a solid sample for microstructural and compositional analysis. The technique involves: (i) irradiation of a very thin sample by a high-energy electron beam, which is diffracted by the lattices of a crystalline or semi crystalline material and propagated along different directions, (ii) imaging and angular distribution analysis of the forward-scattered electrons (unlike SEM where backscattered electrons are detected), and (iii) energy analysis of the emitted X-rays [30]. The topographic information obtained by TEM in the vicinity of atomic resolution can be utilized for structural characterization and identification of various phases of mesoporous materials, *viz*., hexagonal, cubic or lamellar [31]. TEM also provides real space image on the atomic distribution in the bulk and surface of a nanocrystal. A JEOL JEM-1200EX instrument with 120 kV of acceleration voltage was used to probe the materials.

2.4.10. Porosity measurements by N_2 adsorption

Despite of some theoretical limitations, the Brunauer-Emmett-Teller (BET) method continues to be the most widely used method for the evaluation of surface area, pore volumes and pore size distributions of porous solids from N_2 physisorption isotherm data. The BET equation can be represented as follows,

$$\frac{p}{v(p_0 - p)} = \frac{1}{v_m c} + \frac{c-1}{v_m c}\frac{p}{p_0}$$

where v = volume of N_2 adsorbed by the sample under pressure p, p_0 = saturated vapor pressure at the same temperature, v_m = volume of N_2 adsorbed when the surface is covered with a unimolecular layer, and c = constant for a given adsorbate [32].

The equation suggests that the plot of $\frac{p}{v(p_0 - p)}$ versus $\frac{p}{p_0}$ should be linear, and from the intercept $\frac{1}{v_m c}$ and slope $\frac{c-1}{v_m c}$, the values of v_m and c can be determined as follows: $v_m = (\text{slope} + \text{intercept})^{-1}$.

Thus the specific surface area (S) of a sample can be determined as follows,

$$S = \frac{N_0 v_m A}{22414 m}$$

where N_0 = Avogadro number, m = amount of solid adsorbent, A = cross-section of the gas molecules (16.2 $Å^2$ for N_2), and S is expressed in $cm^2\ g^{-1}$ unit.

Several computational procedures are available for the derivation of pore size distribution of mesoporous samples from physisorption isotherms. Most popular among them is the Barrett-Joyner-Halenda (BJH) model, which is based on speculative emptying of the pores by a stepwise reduction of p/p_0, and allowance being made for the contraction of the multilayer in those pores already emptied by the condensate [34]. The mesopores size distribution is usually expressed as a plot of $\Delta V_p/\Delta r_p$ versus r_p, where V_p = mesopore volume, and r_p = pore radius. It is assumed that the mesopores volume is completely filled at high p/p_0. N_2 adsorption-desorption was conducted by NOVA 1200 (Quantachrome) at –196°C. For this particular measurement, before analysis the samples were oven-dried at 100 °C and evacuated at 180 °C for 3 h under vacuum and then the

adsorption-desorption was conducted by passing nitrogen into the sample, which was kept under liquid nitrogen.

2.4.11. Thermal analyses

The thermoanalytical techniques, *viz*., thermogravimetric analysis (TGA) and differential thermal analysis (DTA) have been widely used to establish the thermal stability of ordered mesoporous silica. Both TGA and DTA provide important information about the following: (i) temperature programmed desorption (TPD) and removal of physisorbed water below 150 °C, (ii) oxidative decomposition of the occluded organic materials, accompanied by one or several exotherms within 150 °C and 600 °C, and (iii) dehydroxylation occurring from condensation of adjacent silanol groups to form siloxane bonds at or above 600 °C [35]. Further, DTA can also detect any phase transitions if occur. Thermal analysis of all the samples were carried out by Mettler Toledo 851^e using an alumina pan under a nitrogen (80ml/min) atmosphere from ambient to 1000°C with the increasing rate of 20 K/min.

2.4.12. Acidity measurement

The acidity and the acid strength distribution of the zeolites were measured by the temperature programmed desorption (TPD) of ammonia [36-38]. The sample 20-30 mesh size (~ 1.0 g) was activated in a flow of N_2 at 200 °C for 6 h and cooled to room temperature. NH_3 gas (25 ml/min) was then passed continuously for a period of 30 min, and then the physically adsorbed NH_3 was desorbed by passing N_2 for 15 h (15 ml/min). Acid-strength distribution was obtained by raising the temperature with a ramping rate of 10 °C /min, from 30 to 300 °C in a number of steps in a flow of N_2 (10 ml/min). The NH_3 evolved was trapped in HCl solution and titrated with a standard NaOH solution. The higher the temperature required for desorption the stronger is the acidity of that portion of acid sites. It gives quantitative (total number of acid sites either Brönsted or Lewis) information about acid sites.

2.4.12.1. Temperature programmed desorption of measurement

The process of ammonia adsorption–desorption on catalysts is widely applied for the determination of surface acidity. The amount of ammonia adsorbed at high temperature is usually taken as a measure of acidity. Ammonia was used as adsorbate because all acid sites on the catalyst surface are accessible for NH_3 molecules, and the molecules are more selectively adsorbed in the presence of sites of different strengths. In a typical run, 0.1 g of the catalyst sample was dehydrated at 250 °C for 2 h under He flow (30 mL/min) and then cooled down to 100 °C before being exposed to ammonia. The sample was flushed again for 6 h by He to desorbs any physisorbed ammonia. A desorption profile was then recorded by increasing the catalyst temperature from 100 to 900 °C at a ramp rate of 10 °C/min in the flow of 30 mL/min helium.

2.4.12.2. Pyridine IR studies

The nature of the acid sites in different samples was monitored by recording the transmission - mode IR spectra of adsorbed pyridine vapor. A Thermo Nicolet (model Nexus 870) FTIR equipped with a high-pressure high-temperature stainless steel cell, fitted with water-cooled CaF_2 windows and described previously in detail, was utilized for this purpose. Self-supporting wafers (~50 mg) of 25 mm diameter, placed in a sample holder block, were in direct contact with a chromel-alumel thermocouple. For acidity measurements, the samples were heated in situ for 8-10 h at 550-575 K under vacuum (~1×10^{-3} Torr) and then exposed at 400 K to multiple doses of pyridine (~1.0 μmol each) for a saturation coverage. A gas mixture comprising of nitrogen + pyridine vapor was utilized for this purpose. The gas pressure in the IR cell was monitored with the help of digital capacitance manometer. IR spectra were plotted at 400 K after equilibrating a sample for 15-20 min subsequent to each pulse injection. Spectra were also recorded at room temperature after post-exposure cooling of the sample to room temperature followed by pumping. A total of 300 scans were co-added for plotting of the each spectrum at a resolution of 4 cm^{-1}. The numbers given in the parentheses in some of the IR spectra represent the relative absorbance values for comparison.

2.5. CATALYSIS

The commercialization of quite a few homogeneous catalytic systems consisting of transition metal complexes is difficult due to some inherent shortcomings, *viz.*, (i) complicated work-up of the reaction mixture, (ii) preparation of the pure products not contaminated with catalysts or constituents thereof, (ii) isolation of the valuable catalyst or its constituents, which can be achieved only with high technical complexity and expenditure [39]. The most feasible way to circumvent this problem is to "*heterogenize*" the homogeneous catalyst, by means of immobilization, anchoring, or encapsulation on an inorganic (zeolites or mesoporous materials) [40] or organic (polymeric) [41] solid support.

The concept of heterogenization provides the prospective for extending the benefits of heterogeneous catalysis to homogeneous systems. These benefits include easier separation of catalyst and reaction products leading to shorter work up times, improved process efficiency, the potential for reactivation and reuse of the supported catalyst comprising of expensive ligands. However, the prime requirement of the heterogenization approach is to maintain the stability of the heterogenized complex, such that it does not decompose or leach out from the solid matrix to the liquid phase during the course of reaction, and at the same time retains high activity, selectivity and original configuration.

Anhydrous AR grade chemicals were used without further purification. The liquid phase reaction was carried out in a 50 ml two necked flask attached to a condenser and a septum. The temperature of the reaction vessel was maintained using an oil bath. The reaction mixture was magnetically stirred and heated to the required temperature at atmospheric pressure. The product samples were withdrawn at regular intervals of time and analyzed periodically on a gas-chromatograph (HP 6890) equipped with a flame ionization detector and a capillary column (5 μm thick cross-linked methyl silicone gum, 0.2 mm x 50 m long). The products were also identified by injecting authentic samples and GCMS (Shimadzu 2000 A) and ^{1}H and ^{13}C-NMR (Bruker AC200) analysis.

Finally, the percentage conversion of reactant is defined as the total percentage of reactant transformed. The rate of reactant conversion (TOF) was calculated as the moles

of reactant converted per second per mol of active site. The selectivity to a product is expressed as the amount of a particular product divided by the amount of total products and multiplied by 100.

Reactions carried out by using the synthesized catalysts.

1. Liquid phase oxidation of thioanisole and styrene with different oxidant such as H_2O_2, TBHP, PHIO etc., using chiral metal complex supported MCM-41 catalysts.
2. Liquid phase acylation of naphthalene with p-toluoyl chloride using metal triflate supported mesoporous SBA-15 catalysts.
3. Liquid phase Pechmann condensation of phenolic compound with ethyl acetoacetate using Zr-TMS-BSA catalysts.

2.6. ANALYSIS OF PRODUCTS

2.6.1. Gas Chromatography

Gas chromatography – specifically gas-liquid chromatography involves a sample being vaporized and injected onto the head of the chromatographic column. The sample is transported through the column by the flow of inert, gaseous mobile phase. The column itself contains a liquid stationary phase which is adsorbed onto the surface of an inert solid. The carrier gas must be chemically inert. Commonly used gases are Nitrogen, Helium, Argon and Carbon-dioxide. For optimum column efficiency, the sample should not be too large and should be introduced onto the column as a plug of vapor. Micro-syringe is used to inject sample through a rubber septum into a flash vaporizer port at the head of the column.

Two types of column are present Packed and Capillary columns. For precise work, column temperature must be controlled within tenths of a degree. Many detectors are used in Gas chromatography.

Different detectors give different selectivity. Flame ionization detector (FID), Thermal conductivity detector, Electron Capture detector, Flame photometric detector,

Photo ionization detector, Nitrogen – Phosphorous detector, Hall electrolytic conductivity.

Flame ionization detector is a useful general detector for the analysis of organic compounds, has high sensitivity, large linear response range, low noise, Robust, easy to use but destroys the sample.

2.6.2. Gas chromatography/Mass spectrometry (GC/MS)

GC/MS is a GC detector that is very expensive but very powerful version of the mass spectrometer. When coupled to a GC the detection system itself is often referred to as the mass selective detector or more simply the mass detector. This powerful analytical technique belongs to the class of hyphenated analytical instrumentation (since each part had a different beginning and can exist independently) and is called gas chromatography/mass spectrometry (GC/MS).

The power of this technique lies in the production of mass spectra from each of the analytes detected instead of merely an electronic signal that varies with the amount of analyte. These data can be used to determine the identity as well as the quantity of unknown chromatographic components with an assuredness simple unavailable by other techniques.

Major components of the GC/MS. Ionization source, Mass separator- (1) Quadrapole and (2) Ion trap, Ion detector.

2.6.3. Liquid State NMR

NMR (Nuclear Magnetic Resonance) spectra arise from the spinning of nucleus. It is widely used as one of an armory of instrumental techniques available for structure analysis.

Modern NMR spectroscopy is frequently divided into several categories;

1. High resolution mode on homogenous solutions.
2. High power mode on highly relaxing nuclei which exhibit very broad lines, or polymers etc.

3. The study of solids using eg Magic angle spinning techniques.
4. NMR 3D imaging to resolutions of ~ 1 mm.

The types of information accessible *via* high resolution NMR include;

1. Functional group analysis (chemical shifts)
2. Bonding connectivity and orientation (J coupling),
3. Through space connectivity (Over Hauser effect)
4. Molecular Conformations, DNA, peptide and enzyme sequence and structure.
5. Chemical dynamics (Line shapes, relaxation phenomena).

The number of peaks in the low-resolution spectrum depends on the number of different environments that the hydrogen atoms have in the molecule. There are four aspects of an NMR spectrum that will allow us to determine the identity of the molecule.

1. The number of NMR signals
2. The position of each signal relative to a reference signal
3. The relative area under each signal
4. The spin coupling or spin-spin splitting pattern of each signal

2.7. CONCLUSIONS

In this chapter, synthesis of various types of mesoporous materials such as MCM-41, SBA-15 and zirconia (Zr-TMS) and functionalization of these materials by various groups such as 3-chloropropyl trimethoxy silane, benzylsulfonic acid etc., have been discussed. Further, various physicochemical characterization techniques and their principles have been elaborately demonstrated to conclude that the synthesized catalysts are in good textural and active nature. Catalysis and analysis of products also discussed.

2.8. REFERENCES

[1] C.T. Kresge, M.E. Leonowicz, W.J. Roth, J.C. Vartuli, J. S. Beck, *Nature,* 359, **1992**, 710.

[2] J. S. Beck, J. C. Vartuli, W. J. Roth, M. E. Leonowicz, C. T. Kresge, K. D. Schmitt, C. T. W. Chu, D. H. Olson, E. E. Sheppard, S. B. McCullen, J. B. Higgins, J. L. Schlenker, *J. Am. Chem. Soc.,* 114, **1992**, 10834.

[3] A. Corma, M. T. Navarro, J. P. Pariente, *J. Chem. Soc., Chem. Commun.,* **1994,** 147.

[4] P. T. Tanev, M. Chibwe, T. J. Pinnavaia, *Nature,* 368, **1994,** 321.

[5] S. Shylesh, A. P. Singh, *J. Cata.,* 228, **2004**, 333.

[6] Brunel, D., Cauvel, A., Fajula, F. & DiRenzo, F. In *Studies in Surface Science and Catalysis* 97 (eds Bonneviot, L., et al.) 173 – 180 (Elsevier, Amsterdam, 1995).

[7] Diaz, J. J., Balkus, K. J. Jr, Bedioui, F., Kurshev, V. & Kevan, L. *Chem. Mater.,* 9, **1997**, 61.

[8] C. W. jones, K. Tsuji and Mark. E. Davis, *Nature,* 393, **1998**, 52.

[9] T. Asefa, M.J. Maelachlan, N. Coombs, G. A. Ozin, *Nature,* 402, **1999**, 867.

[10] S. Inagaki, S. Guan, Y. Fukushima, T. Ohsuna, O. Terasaki, *J. Am. Chem. Soc.,* 121, **1999**, 9611.

[11] R. J. P. Corriu, D. Leclereq, *Angew. Chem.,* 108, **1996**, 1524.

[12] W. H. Bragg, W. L. Bragg, *The Crystalline State*, *Vol. 1*, McMillan, New York, **1949**.

[13] S. Biz, M. Occelli, *Catal. Rev. -Sci. Eng.,* 40, **1998**, 329.

[14] G. Bergeret, *Handbook of Heterogeneous Catalysis*, *Vol. 2*, Eds: G. Ertl, H. Knozinger, J. Weitkamp, Wiley-VCH, Weinheim, **1997**, P. 464.

[15] R. C. Rau, *Advances in X-Ray Analysis*, *Vol. 5*, Ed: W. M. Mueller, Sir Isaac Pitman and Sons, Ltd., London, **1962**, P. 104.

[16] P. R. Griffiths, J. A. De Haseth, *Fourier Transform Infrared Spectrometry*, John Wiley and Sons, Inc., New York, **1986**.

[17] C. C. Freyhardt, M. Tsapatsis, R. F. Lobo, K. J. Balkus, M. E. Davis, *Nature,* 381 **(1996)** 295.

[18] D.A. Long, *Raman Spectroscopy,* McGraw-Hill International Book Company, **1977**.

[19] B.P. Straughan, S. Walker, *Spectroscopy,* Chapman and Hall, London, Vol.2, **1976**.

[20] F. A. Rushworth, D. P. Tunstall, *Nuclear Magnetic Resonance*, Gordon and Breach Science, Publishers Ltd., London, **1973**.

[21] W. W. Paudler, *Nuclear Magnetic Resonance: General Concepts and Applications*, John Wiley and Sons Inc., New York, **1987**.

[22] M. Mehring, *High Resolution NMR Spectroscopy in Solids*, Springer-Verlag, Berlin, **1976.**

[23] G. Engelhardt, D. Michel, *High-Resolution Solid-State NMR of Silicates and Zeolites*, John Wiley and Sons Ltd., Chichester, **1987**.

[24] G. Engelhardt, in: *Handbook of Heterogeneous Catalysis*, *Vol. 2*, Eds: G. Ertl, H. Knozinger, J. Weitkamp, Wiley-VCH, Weinheim, **1997**, P. 525.

[25] J. W. Robinson, *Atomic Absorption Spectroscopy*, Marcel Dekker, New York, **1975**.

[26] G. L. Moore, *Introduction to Inductively Coupled Plasma Atomic Emission Spectrometry*, Elsevier, Amsterdam, **1988**.

[27] G. Lawes, *Scanning Electron Microscopy And X-Ray Microanalysis*, John Wiley and Sons Ltd., Chichester, **1987**.

[28] D. E. Newbury, D. C. Joy, P. Echlin, C. E. Fiori, J. I. Goldstein, *Advanced Scanning Electron Microscopy and X-Ray Microanalysis*, Plenum Press, New York, **1986**.

[29] J. R. Fryer, *Chemical Applications of Transmission Electron Microscopy*, Academic Press, San Diego, **1979**.

[30] V. Alfredsson, M. Keung, A. Monnier, G. D. Stucky, K. K. Unger, F. Schuth, *J. Chem. Soc., Chem. Commun.,* **1994**, 921.

[31] Z. L. Wang, in: *Characterization of Nanophase Materials*, Ed: Z. L. Wang, Wiley-VCH, Weinheim, **2000**, Chapter 3, P. 37.

[32] S. Brunauer, P. H. Emmett, E. Teller, *J. Am. Chem. Soc.,* 60, **1938**, 309.

[33] E. P. Barrett, L. G. Joyner, P. P. Halenda, *J. Am. Chem. Soc.,* 73, **1951**, 373.

[34] C. -Y. Chen, H. -X. Li, M. E. Davis, *Microporous Mater.,* 2, **1993**, 17.

[35] M. Chamumi, D. Brunel, F. Fajula, P. Geneste, P. Moreau, J. Solof, *Zeolites,* 14, **1994**, 283.

[36] A.P. Singh, D. Bhattacharya, *Catal. Lett.*, 32, **1995**, 327.

[37] A.P. Singh, D. Bhattacharya, S. Sharma, *Appl. Catal. A: Gen.,* 150, **1997**, 53.

[38] J. Manassen, *Catalysis, Progress in Research*, Eds: F. Basolo, R. E. Burwell Jr., Plenum Press, New York, **1973**, P. 177.

[39] D. E. De Vos, M. Dams, B. F. Sels, P. A. Jacobs, *Chem. Rev.,* 102, **2002**, 3615.

[40] P. Ermert, *Solid-Supported Combinatorial and Parallel Synthesis of Small-Molecular-Weight Compound Libraries*, Eds: D. Obrecht, J. M. Villalgordo, Elsevier, Oxford, **1998**, P. 44.

CHAPTER-3

CHIRAL METAL COMPLEX IMMOBILIZED MESOPOROUS MCM-41 CATALYSTS

3.1. INTRODUCTION

Immobilization of catalysts on inorganic matrices has been a great area of research for academic and industrial points of view, as this method affords an ideal combination of the advantages of homogeneous catalysts and avoids their disadvantages related to handling and reusability of the catalyst [1]. In this field, only few iron complexes have been designed for heterogeneous catalysts for oxidation catalysis [2] whereas Mn salen and metalloporphyrins have been widely studied [3]. The emergence of new non-heme iron catalysts for alkanes, alkenes and sulfides oxidation by H_2O_2 during the recent years prompted us to graft tetradentate pyridine/amine ligands, derivated from BISPICEN ligand (BISPICEN = *N*,*N*'- bis(2-pyridylmethyl)-1,2-ethanediamine) into a mesoporous phase [4]. Among them, a few have been found enantioselective for transformations of alkenes into epoxides and cis diols [5] and sulfides into sulfoxides [6]. Their main interest resides into their easy accessibility even though their enantioselectivity was moderate in most cases and suffer of a lack of stability. After the discovery of M41S family of mesoporous silicates and aluminosilicate materials by Mobil scientists in 1992 [7, 8], MCM-41 has become the most popular member of the group due to their unique textural features and simple synthesis procedures. The most interesting feature of MCM-41 is its regular pore system, which consists of a hexagonal array of unidimentional, hexagonally shaped pores. The pore diameter of MCM-41 can be varied systematically between 2-10 nm by use of surfactants with different chain lengths and pore expanders like trimethyl benzene (TMB). The catalytic properties of the MCM-41 materials can be adjusted by the incorporation of different metals into the MCM-41 framework [9-11]. Further, the diversity in the catalytic properties can be broadened by the grafting of organosilanes which contain organic functional groups onto the internal pore surfaces [12-14] or incorporating them during the synthesis process. An advantage of there organic-inorganic hybrid mesoporous materials is that they do not swell or dissolve in organic solvents and they have other advantages such as their superior mechanical and thermal stabilities [15-17]. Moreover, the leaching of active sites can also be avoided as the organic moieties are covalently attached to inorganic supports.

Accordingly, we report in this work our attempt to graft Fe and Ru metal complexes of N,N'-bis(2-pyridylmethyl)-N-methyl-(1*S*,2*S*)-1,2-cyclohexanediamine (L_2Me), a version of the BISPICEN ligand, and some of its derivatives into MCM-41 phases and their catalytic properties for sulfides oxidations by H_2O_2. The immediate goals of our study were (i) to evaluate the heterogenization method of the L_2Me ligand over mesoporous MCM-41 support, (ii) the effect of the support on the conversion and oxidation of methyl phenyl sulfide by hydrogen peroxide, and (iii) to determine the extent of the increased stability of the catalysts with regard to the homogeneous catalysts as well as their recycling properties.

3.2. EXPERIMENTAL

3.2.1. Synthesis of parent and organo-functionalized MCM-41

The Si-MCM-41 was prepared from the gel with the following composition. SiO_2: CTMABr: NaOH: H_2O 1: 0.19:0.4:78. In a typical synthesis, cetyltrimethylammonium bromide (CTMABr) was added to the solution of NaOH in H_2O, under stirring and the mixture was further stirred for 1h. To this mixture, calculated amount of fumed silica was added slowly. The gel mixture was stirred for 6 h and pH was adjusted to 10.7-10.9 by addition of 0.1 M HCl solution. Finally the mixture was transferred into a Teflon-lined autoclave and kept at 100° C under static conditions for 72 h. The solid material obtained was then filtered, washed well with distilled water till the filtrate shows a neutral pH, and then air-dried. The surfactant of the as-synthesized mesoporous sample was removed by calcination in air at 540° C for 10h.

Surface modification of MCM-41 material was achieved by a post synthesis grafting method (Scheme 3.2A). One gram of calcined MCM-41 material was suspended in 50 mL of dry toluene and allowed to stir for 15 min at room temp. Then 2.5 mmol of chloropropyl trimethoxy silane (3-ClPTS) was added slowly and then the mixture was stirred overnight at reflux temperature under inert atmosphere. The material was filtered, washed with toluene, soxhlet extracted with dichloromethane (DCM) for 12 h, and then dried under vacuum. The material obtained is designated as Cl-MCM-41. The free –OH

groups present in Cl-MCM-41 were protected by adding 1.5 mmol of methyl trimethoxy silane to a stirred suspension of 1g of Cl-MCM-41 in dry toluene (50 mL), followed by stirring for 12 h at reflux temp under inert atmosphere. Then the material was filtered, washed with toluene and soxhlet extracted with DCM for 24 h. The final material was named –OH protected Cl-MCM-41 (Scheme 3.2B).

3.2.2. Synthesis of L_2Me and $L_2(Me)_2$

The L_2Me ligand was synthesized for anchoring on the solid phase and subsequent complexation with Ru and Fe whereas the ligand $L_2(Me)_2$ was synthesized to prepare the homogeneous complexes of Ru- and Fe for comparison. The following synthetic steps were adapted from the published literature (Scheme 3.1) for the syntheses of L_2Me and $L_2(Me)_2$ [18].

3.2.2.1. Synthesis of (1S, 2S)-N, N'-Bis (2-pyridinylmethyl)-1, 2-cyclohexane diimine [L_1]

To a stirred solution of 2-pyridylcarboxaldehyde (1 g , 9.34 mmol) in methanol (25 mL), (1*S*, 2*S*)-(+)-1,2-cyclohexanediamine (485 mg, 4.25 mmol) in methanol (25 mL) was added slowly under argon at 0°C using a syringe pump. The mixture was stirred for 1 h at ambient temperature, followed by addition of anhydrous sodium sulfate, and was stirred further for another 15 min. The mixture was filtered and the solvent was removed under reduced pressure resulting in a yellow powder. It was then re-crystallized from acetonitrile. Fine yellow crystals of the ligand **L_1** (1.14 g, 3.9 mmol, 92% yield) were obtained. ^{1}H-NMR (300MHz, $CDCl_3$, δ (ppm)): 8.61 (d, 2H, Py, J = 4.2 Hz); 8.38 (s, 2H, C**H**=N); 7.95 (d, 2H, Py, J = 7.8 Hz); 7.71 (ddd, 2H, Py, J = 7.4 Hz); 7.29 (ddd, 2H, Py, J = 7.5 Hz, J =4.3 Hz); 3.6 (m, 2H, Cy**H**N); 1.93 (m, 6H, Cy**H**), 1.65 (m, 2H, Cy**H**)

3.2.2.2. Synthesis of (1S, 2S)-N, N'-Bis (2-pyridinylmethyl)-1, 2-cyclo hexane diamine [L_2]

To a stirred solution of **L_1** (0.3473 g, 1.19 mmol) in methanol at 0 °C was added sodium borohydride (0.1786 g, 4.76 mmol) in portions over a period of 30 min. The mixture was refluxed for 1 h, and then cooled to ambient temperature followed by addition of 2 mL of distilled water. The solvent was removed under reduced pressure leading to a white solid. The solid was dissolved in 20 mL of dichloromethane, washed successively two times with 10 mL of aqueous saturated solution of sodium bicarbonate, twice with 10 mL of distilled water and finally with 10 mL of aqueous saturated sodium chloride solution. The aqueous layer was again extracted with 10 mL of dichloromethane. The combined organic layer was slowly evaporated under reduced pressure, resulting in yellow oil **L_2** (300 mg, 1.014 mmol, 85% yield). ^{1}H-NMR (300 MHz, $CDCl_3$, δ (ppm)): 8.58 (d, 2H, Py, J = 5 Hz, J = 1.2 Hz); 7.68 (ddd, 2H, Py, J = 7.7 Hz, J = 1.3 Hz); 7.6 (d, 2H, Py, J = 7.7 Hz); 7.2 (ddd, 2H, Py, J = 7.7 Hz, J = 5Hz); 4.1 and 3.91 (d, 2 * 2H, Ha & Hb, J = 14.09 Hz), 2.7 (s, 2H, N**H**); 2.4 (m, 2H, Cy**H**); 2.2 (m, 2H, Cy**H**); 1.77 (m, 2H, Cy**H**); 1.23 (m, 4H, Cy**H**).

3.2.2.3. Synthesis of (1S, 2S)-N-methyl-N, N'-Bis (2-pyridinylmethyl)-1, 2-cyclo hexanediamine (L_2Me) and (1S, 2S)-N, N'- Dimethyl-N, N'-Bis (2-pyridinyl methyl)-1, 2-cyclohexanediamine [$L_2(Me)_2$]

The diamine L_2 (0.4291 g, 1.45 mmol) was dissolved in 37% formaldehyde (2.7 mL) and the resulting solution was stirred at 20 °C for 10 min. Aqueous 90% formic acid (3.3 mL) was then added and the mixture was stirred and thermally treated at 90 °C for 48 h. The mixture was then cooled to 20 °C and pH was adjusted to 12 by addition of aqueous sodium hydroxide (3M) with constant cooling. The aqueous layer was extracted with diethyl ether (2 x 50 mL) and the combined organic layers were dried (anhy. Na_2SO_4), filtered and evaporated to give an oil, which was purified by column chromatography (Al_2O_3, ethyl acetate/hexane/triethylamine 10: 4: 1) to afford the title product, viz., dimethylated **$L_2(Me)_2$** (0.308g, 0.95 mmol, 66% yield) and a second

product , the monomethylated **L_2Me** (0.122 g, 0.4 mmol, 27% yield), as clear oil. ^{1}H-NMR (300MHz, $CDCl_3$, δ (ppm)): **$L_2(Me)_2$** : 8.55 (d, 2H, Py, J = 4.8 Hz); 7.63 (m, 4H, Py); 7.17 (m, 2H, Py); 3.98 & 3.86 (d, 2*2H, CH_2, 14.7 Hz); 2.71 (m, 2H), 2.33 (s, 6H, 2* CH_3); 2.02 (m, 2H); 1.81 (m, 2H); 1.26 (m, 4H). **L_2Me**: 8.43 (d, 2H, Py, J = 4.2 Hz); 7.56 (m, 3H, Py);7.23 (m, 1H, Py); 7.07 (m, 2H, Py); 3.97 (d, 1H, CH_2, J = 14.1 Hz); 3.78 & 3.73 (ddd, 2H, CH_2, J = 4.5 Hz, J = 4.8 Hz); 3.54 (d, 1H, CH_2, J = 14.4 Hz); 2.43 (m, 2H); 2.24 (m, 1H); 2.15 (s, 3H, CH_3); 1.89 (m, 1H); 1.76 (m, 1H); 1.67 (m, 1H), 1.17 (m, 5H).

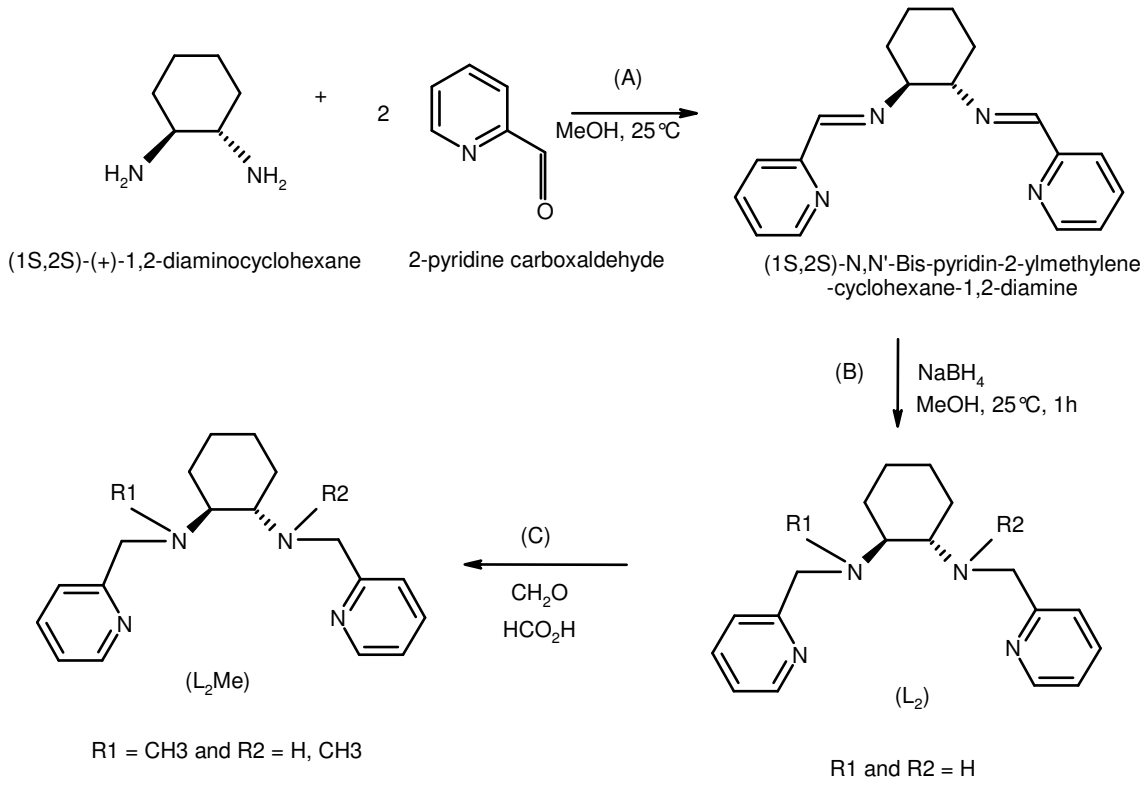

Scheme 3.1. Synthesis of chiral ligand (A) Synthesis of [L] (1S,2S)-N,N'-Bis-pyridin-2-ylmethylene-cyclohexane-1,2-diamine (B) Synthesis of [L_2] (1S,2S)-N,N'-Bis-pyridin-2-ylmethyl-cyclohexane-1,2-diamine (C) Synthesis of (1S,2S)-N-methyl-N,N'-Bis-pyridin-2-ylmethyl-cyclohexane-1,2-diamine [L_2(Me)] or (1S, 2S)-N, N'- Dimethyl-N, N'-Bis(2pyridinylmethyl)- 1,2-cyclohexanediamine ($L_2(Me)_2$)

3.2.3. Synthesis of homogeneous complex Fe-L_2 $(Me)_2(CF_3SO_3)_2$

A solution of the ligand **$L_2(Me)_2$** (69 mg, 0.212 mmol) and iron triflate (93 mg, 0.212 mmol) in 15 mL of dry acetonitrile was stirred and heated under argon atmosphere for 2 h. The mixture was then cooled to ambient temperature and the solvent was removed under inert atmosphere leading to an oily residue. The residue was then treated with dry diethyl ether to give a stable, brownish yellow powder of Fe-$L_2(Me)_2(CF_3SO_3)_2$ (70 % yield). The complex was characterized using ^{1}H NMR and EI-MS. Data agreed with the one reported by Que et al. [19].

^{1}H-NMR (300MHz, CD_3CN, δ (ppm)): 106.16 (vb); 102.53 (vb); 98.31 (vb); 92.36 (vb); 88.5 (b); 76.5 (b); 53.75 (s); 51.25 (s); 48.06 (sh); 46.8 (s), 32.63 (vb); 29.66 (vb); 21.99 (vb); 17.25 (s); 8.9 (s); 7.9 (s); 6.25 (s); 5.16 (s); -3.14 (s); -12.89 (s); -31.34(b) ESI-MS : m/z 529.3 [$L_2(Me)_2$ Fe $(CF_3SO_3)]^+$

3.2.4. Synthesis of homogeneous Ru-$L_2(Me)_2Cl_2$. DMSO

Synthesis of the ruthenium complex was adapted from a literature procedure [20]. The complex was prepared by the reaction of the ligand **$L_2(Me)_2$** (50 mg, 0.17 mmol) and *trans*-$RuCl_2(DMSO)_4$ (81 mg, 0.17 mmol) in toluene (10 mL) at 110 °C for 22 h. The formed precipitate was filtered and was recrystallized from acetone by ether diffusion leading to a green powder (40 mg, 70 μmol, 75 % yield).

^{1}H-NMR (300MHz, CD_2Cl_2, δ (ppm)): 9.1-9.3 (m, py-H); 8.25 (d, py-H); 7.3-8.0 (m, py-H); 4.9 (d, CH_2); 4.7 (d, CH_2); 4.3-4.45 (m, CH_2); 3.1-3.6 (m); 3.4 (s, 2N-CH_3); 2.15-2.9 (m); 1.5-2.0 (m); 1.2 (t). ESI-MS: m/z 539.1 [$L_2(Me)_2$ RuCl(DMSO)]$^+$, 461.31 [$L_2(Me)_2$ RuCl]$^+$ UV-Vis [λ max, nm (ε , $M^{-1}cm^{-1}$) in CH_2Cl_2]: 639 (1058); 476 (1054); 362 (4078); 246 (6564).

3.2.5. Grafting of (1S, 2S)-N, N'-bis-pyridin-2-ylmethyl-cyclohexane-1, 2-diamine (L_2Me) ligand inside the Cl-MCM-41

The ligand, **L_2Me**, was introduced into the inner surfaces of MCM-41 by adding 0.1g of **L_2Me** in a stirred suspension of –OH protected Cl-MCM-41 (1g) in dry toluene

(30 ml). This mixture was refluxed for 24 h in inert atmosphere, filtered, and washed with toluene and then with CH_2Cl_2 followed by soxhlet extraction, with 1:1 mixture of DCM: diethyl ether for about 24h. The final material is called as L_2Me-MCM-41 (scheme 3.2C). The final proportion of the anchored ligand over Cl-MCM-41 is 7% wt. of the solid.

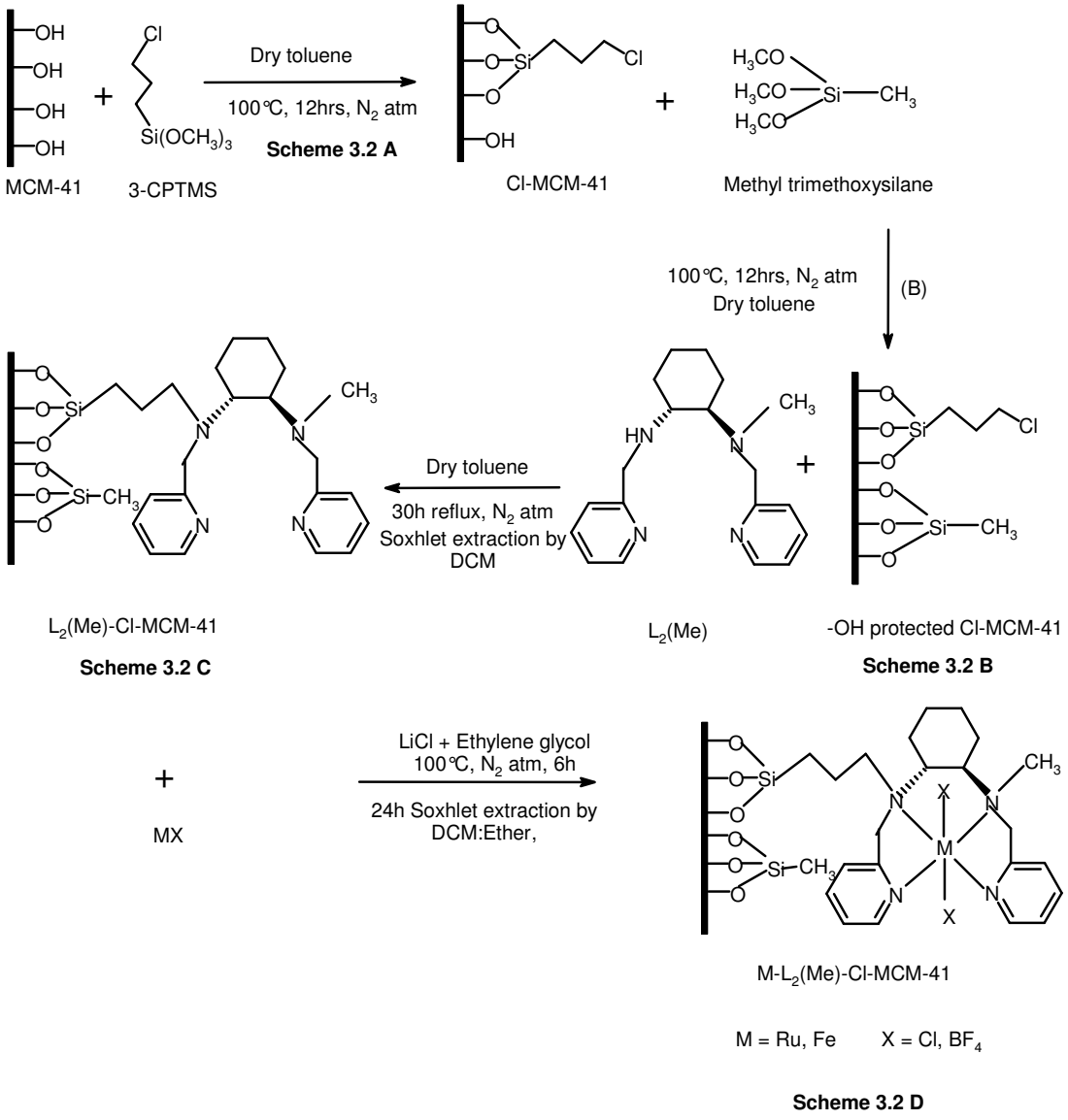

Scheme 3.2. Functionalization of MCM-41 and heterogenization of ligand (A) Silylation of calcined MCM-41 (B) Free –OH protection (C) Heterogenization of ligand (D) Metal insertion.

3.2.6. Complexation of Ru and Fe in the L_2Me-MCM-41

3.2.6.1. Complexation of Ru with L_2Me-MCM-41

Ruthenium was inserted into the L_2Me moiety by adding 1g of L_2Me-MCM-41 to a stirred solution of 0.2g of $RuCl_3.3H_2O$ and 0.22 g of LiCl in of ethylene glycol (15 mL). The mixture was heated to about 110° C for about 6 h in inert condition and soxhlet extracted with 1:1 mixture of ethanol: ether. The final yellow green material was called Ru-L_2Me-MCM-41.

3.2.6.2. Complexation of Fe with L_2Me-MCM-41

Iron was inserted into the L_2Me moiety by adding 1g of L_2Me-MCM-41 to a stirred solution of 0.2 g of $Fe(BF_4)_2$ in a Schlenk tube under argon atmosphere at room temperature. The mixture was stirred for 2 h and the solvent was then removed. The resulting light yellow powder was washed with methanol until the solution was totally colorless. The final material was called Fe-L_2Me-MCM-41.

3.2.7. Reactivity: Oxidation of sulfide catalyzed by Fe(II) and Ru(II) complexes

Oxidation reactions were carried out in a 5 mL flask equipped with a magnetic stirrer. The flask was charged with 3 mL of a solution or suspension of the catalyst (0.007 mmol) in methanol and stirred for 15 min, and then methyl phenyl sulfide (1 mmol) and the oxidant (2.5 mmol of 30 % H_2O_2 or PhIO or TBHP) were added under stirring. An internal standard (20μL of a 1M solution of benzophenone in acetonitrile) was added to the reaction mixture. Chemical yield and enantiomeric excess were measured by GC/MS.

3.3. CHARACTERIZATION OF THE CATALYSTS

Synthesized catalysts were characterized by X-ray diffraction using a Rigaku Miniflex powder diffractometer on finely powdered samples using Cu-Kα radiation and 15 kV 10 mA. The XRD patterns were recorded for 2 theta between 1.5° and 10°, at a scan rate of 2°/min. Adsorption of nitrogen was carried out at 77 K using a NOVA 1200

(Quantachrome) apparatus for analyzing surface areas and pore-size distributions of the synthesized catalysts. Specific surface areas were calculated following the BET procedure. Pore-size distribution was obtained by using the BJH pore analysis applied to the desorption branch of the nitrogen adsorption/desorption isotherms. FTIR spectra of solid samples were taken in the range of 4000 – 400 cm^{-1} on a Shimadzu FTIR 8201 instrument. Thermogravimetric analyses (TGA and DTA)
were performed using a Diamond TG/DTA instrument, from 30°C to 1000°C at a heating rate of 10 °C/min under airflow. Ruthenium and iron contents in the catalysts were determined using a GBC Avanta Ver 1.32 AAS instrument. Analyses of the organic content present in the catalysts were carried out using a Carlo-Erba C, H, and N analyzer. UV-vis spectra were recorded by a JASCO spectrometer equipped with a diffuse reflectance attachment, using $BaSO_4$ as the reference. The scanning electron microscope (SEM) photographs of the samples were obtained using a JEOL-JSM-5200 instrument. XPS of the samples were recorded using a VG Microtech multilab ESCA 3000 spectrometer equipped with a twin anode of Al and Mg. All the measurements were made on as-received powder samples using Mg-K_α X-ray at room temperature. Base pressure in the analysis chamber was 4 X 10^{-10} Torr. A Multi channel detection system with nine channels was employed to collect the data. The overall energy resolution of the instrument was better than 0.7 eV, determined from the full width at half maximum of the $4f_{7/2}$ core level of a gold surface. The errors in all BE values were within ± 0.1 eV. Surface analysis by XPS spectra was carried out in terms of the binding energy (BE) values of various elements present in the catalyst supports after necessary C 1s correction, which was the major element in our system. EPR experiments at 4 K were performed with a Band X Bruker EMX 300 equipped with an OXFORD cryostat. Solution 300 MHz 1H NMR spectra were recorded on a DPX300 Brüker spectrometer. Gas chromatography (GC) equipped with a MS detector was performed on a Perkin-Elmer Autosystem XL instrument, using a SE 30 column. Enantiomeric excess were measured using a chiral capillary column Lipodex-E.

3.4. RESULTS AND DISCUSSION

3.4.1. X-ray diffraction (XRD)

Figure 3.1. shows the powder X-ray diffraction (XRD) patterns of calcined MCM-41, OH protected Cl-MCM-41, Ru-L_2Me-MCM-41 and Fe-L_2Me-MCM-41 materials. The typical hexagonal phase of MCM-41 [main (100) peak with weak (110), (200), and (210) reflections] is clearly visible in calcined MCM-41 [21]. Due to partial loss of space correlation of the pores, the reflection almost disappeared (indices 210) after the post synthesis modification. This kind of resultant disorder in the silica meso structure has been commonly observed in the studies of silylation of the mesoporous silicas. However, the retention of the characteristic peaks [(100), (110) and (200)] indicates that the meso structure is retained after incorporation of organic functional groups, ligand and metals. Moreover, a slight decrease in the peak intensities was observed in the case of the metal complex loaded samples, which might be due to partial filling of the void space due to the presence of metal complexes inside the mesopores.

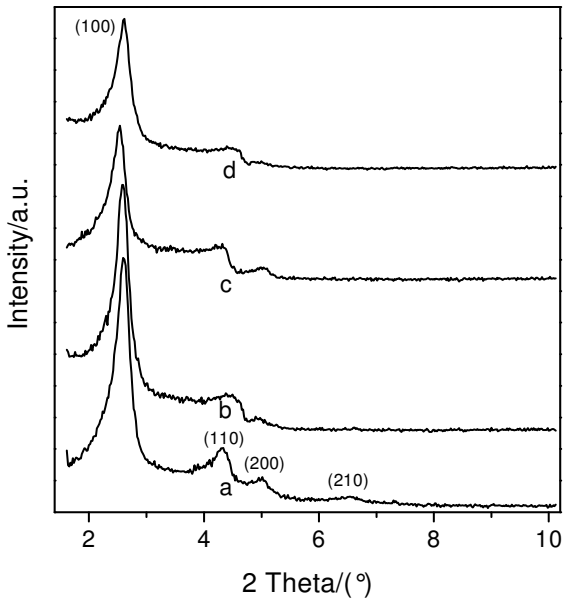

Fig. 3.1. XRD patterns of (a) calcined MCM-41 (b) –OH protected Cl-MCM-41 (c) Ru-L_2Me-MCM-41 (d) Fe-L_2Me-MCM-41.

A comparison of unit cell parameter (a_0) values (calculated from XRD patterns) of the functionalized MCM-41 and those with anchored metal complexes is presented in Table 3.1.

3.4.2. FT IR spectra

Fig. 3.2. Shows the FT IR spectra of the as-synthesized, calcined, and –OH protected Cl-MCM-41, the neat ligand (L_2Me), Fe-L_2Me-MCM-41 and Ru-L_2Me-MCM-41. The strong and broad band in the region of 3600 to 3200 cm^{-1} corresponds to the hydrogen bonded Si-OH groups present in the mesoporous samples and a sharp peak at 3743 cm^{-1} corresponds to the free silanol group [22]. All the MCM-41 samples, except calcined MCM-41, show bands in the region of 2800 to 2900 cm^{-1} corresponding to the C-H stretching frequency of the surfactant in the case of as-synthesized MCM-41, chloropropyltrimethoxy and methyl triethoxy groups in the case of –OH protected Cl-MCM-41 and with the ligand moiety in the case of Fe-L_2Me-MCM-41 and Ru-L_2Me-MCM-41.

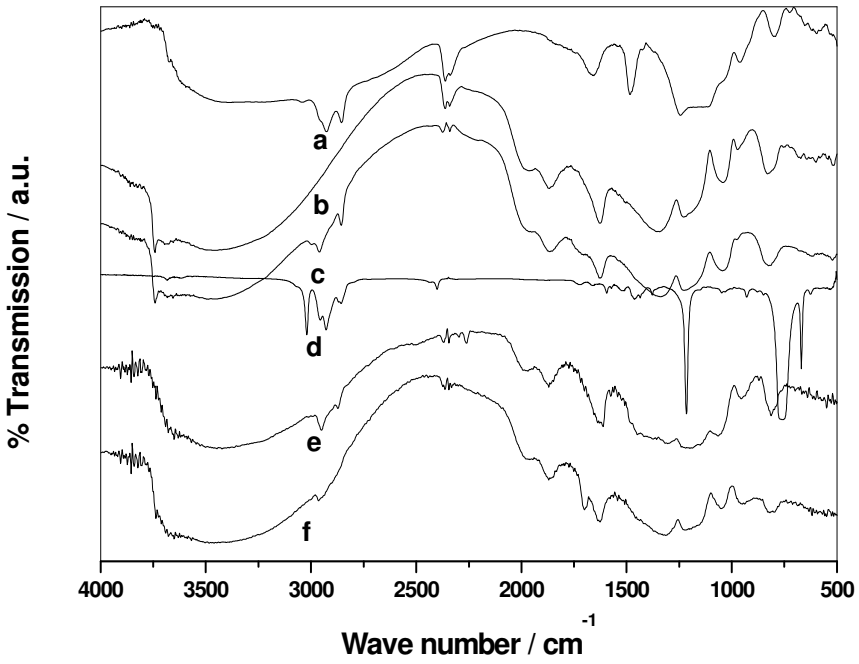

Fig. 3.2. FTIR spectrum of the (a) as synthesized MCM-41 (b) calcined MCM-41 (c) –OH protected Cl-MCM-41 (d) neat ligand (L_2Me) (e) Ru-L_2Me-MCM-41 (f) Fe-L_2Me-MCM-41.

The band at 1080 cm^{-1} and 800 cm^{-1} is assigned to the asymmetric and symmetric Si-O-Si vibrations of MCM-41 respectively and the band at 970 cm^{-1} is assigned to the asymmetric Si-OH vibration [23]. The IR spectrum of the neat ligand L_2Me shows C-H stretching bands in the region of 3020 to 2855 cm^{-1} and a sharp C-N stretching vibration of tertiary amine at 1218 cm^{-1}. The band between the regions 1430 – 1665 cm^{-1} corresponds to the ring stretching vibration of the ligand. The C=N stretching band of the heterocyclic ring appears along with the C=C band near 1592 cm^{-1} [24]. However in the heterogenised catalyst because of low loading of ligands all the major characteristic bands (C-N and C=N bands) were overlapped with the Si-O-Si stretching bands of mesoporous material [Fig. 3.2e & f] and are hardly indiscernible.

3.4.3. Nitrogen sorption studies

Incorporation or anchoring of organic groups or metal in the framework position and/or into the wall of mesoporous materials usually results in a progressive decrease in their surface area [25, 26]. N_2 sorption studies of all catalysts exhibited type IV behavior, characteristics of mesoporous material [27, 28] according to the IUPAC classification. The BET surface area, pore volume and pore diameter of all catalysts are shown in Table. 3.1.

The decrease in surface area and pore volume of functionalized MCM-41 is attributed to the functionalization of organic moieties onto mesoporous wall. Before the functionalization, the position of inflection in the $P/P_0 = 0.2 – 0.4$ region depends on the diameter of the mesopores and its moderate sharpness indicates the uniformity of the pore size distributions Fig. 3.3. (A). After the functionalization with chloropropyltrimethoxysilane the position of inflection is in the $P/P_0 = 0.2 - 0.4$ region Fig. 3.3 (B). The pore size distribution curve of metal complex grafted catalysts shows one small extra pore corresponds to the less ordered structure. The position of inflection (P/P0) is also changed considerably (shown in Fig. 3.3 (C & D)). These results indicate that the mesoporosity of MCM-41 samples was decreasing during each treatment, which may be attributed to the anchoring of various moieties on the inner pore walls of MCM-41.

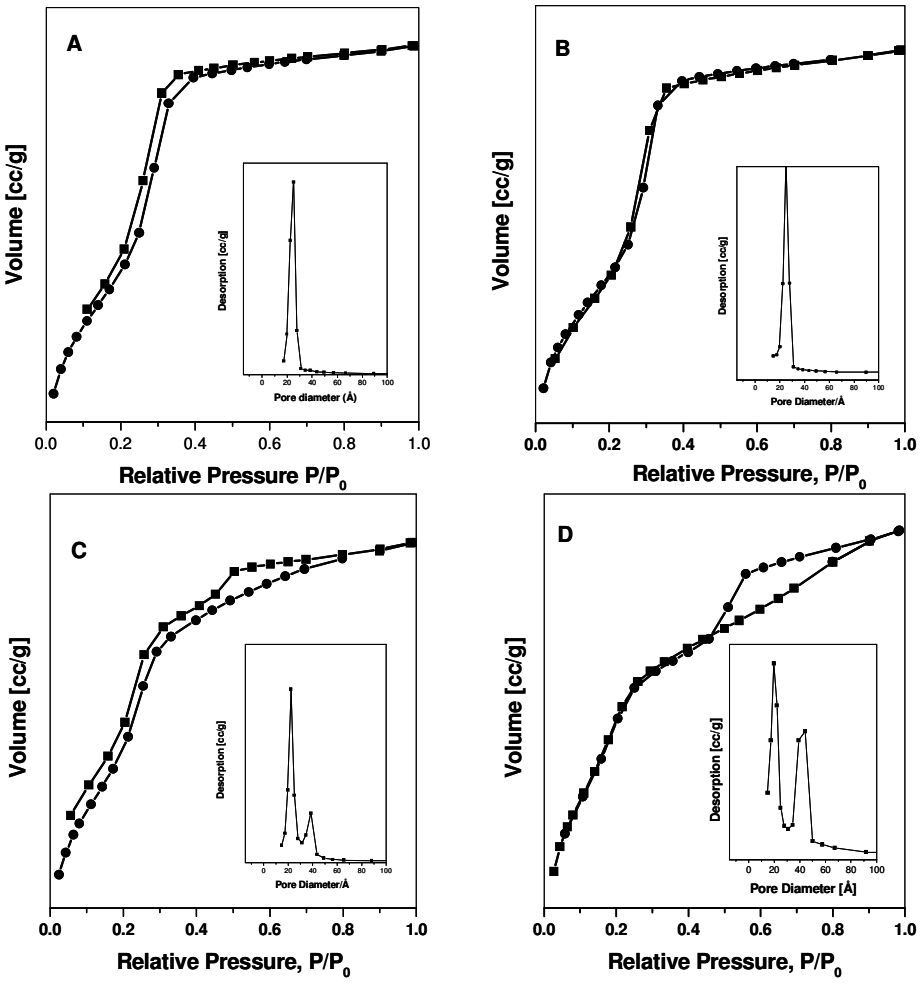

Fig. 3.3. Nitrogen adsorption-desorption isotherms and pore – size distribution (inset) of (A) Calcined (B) Cl-MCM-41 (C) Ru-L_2Me-MCM-41 (D) Fe-L_2Me-MCM-41

3.4.4. Thermal analysis

Fig. 3.4. shows the TGA-DTG pattern of as-synthesized, calcined, and -OH protected Cl-MCM-41, the neat ligand (L_2Me), Ru-L_2Me-MCM-41 and Fe-L_2Me-MCM-41. The TGA curve of as-synthesized MCM-41 sample shows three peaks for weight loss. The first weight loss (endothermic) below 150 °C corresponds to the loss of physisorbed water molecule. The significant second weight loss that occurred in the region 150 – 380 °C is attributed to the removal of surfactant in the as-synthesized

MCM-41 [11, 29]. Moreover a small weight loss in the range of 600 to 800°C corresponds to the dehydration of the hydroxyl groups inside the pores (Fig. 3.4a).

In the case of calcined MCM-41, we observed only two weight losses corresponding to physisorbed water molecule (below 150 °C) and dehydration of the hydroxyl groups inside the pores (around 650 °C), indicating that all the surfactant molecules are removed during the calcination process (Fig. 3.4b). Along with the above (calcined MCM-41) weight losses, we observed an additional third weight loss in the case of –OH protected Cl-MCM-41 in the range between 250 and 300 °C which could correspond to the removal of 3-CPTMS and methyl trimethoxy silane (Fig. 3.4c). For the neat ligand there is only one weight loss in the range of 250 to 300 °C (Fig. 3.4d) which is shifted to 460 – 600 °C in the case of Ru/Fe-L_2Me-MCM-41 catalysts, indicating that the heterogenised metal complexes are more stable than the pure ligand (Fig. 3.4e & f).

Table 3.1. Summary of the catalyst properties

Sample	Metal (wt%)	a_0 [c] (Å)	Pore diameter (Å)	Pore volume (ccg^{-1})	S_{BET} (m^2g^{-1})
Calcined MCM-41	-	41.6	31.1	0.8	1082
Cl-MCM-41	-	40.4	31.0	0.7	1019
-OH Protected Cl-MCM-41	-	41.1	30.1	0.5	696
Ru-L_2Me-MCM-41[a]	1.71	42.5	31.0	0.5	615
Fe-L_2Me-MCM-41[b]	1.95	41.8	28.6	0.4	585

[a] Ligand grafted Cl-MCM-41; elemental analysis: C = 8.8%, H =2.1 %, N = 1.2%, Ru = 1.71 % (from AAS analysis). Input ligand grafted on Cl-MCM-41 = 10 wt. %; Output of ligand grafted on Cl-MCM-41 = 7 wt. %

[b] Ligand grafted Cl-MCM-41; elemental analysis: C = 9.8%, H =2.3 %, N = 1.3%, Fe = 1.95 % (from AAS analysis).

[c] Unit cell parameter $(a_0) = d_{100} \times 2/\sqrt{3}$.

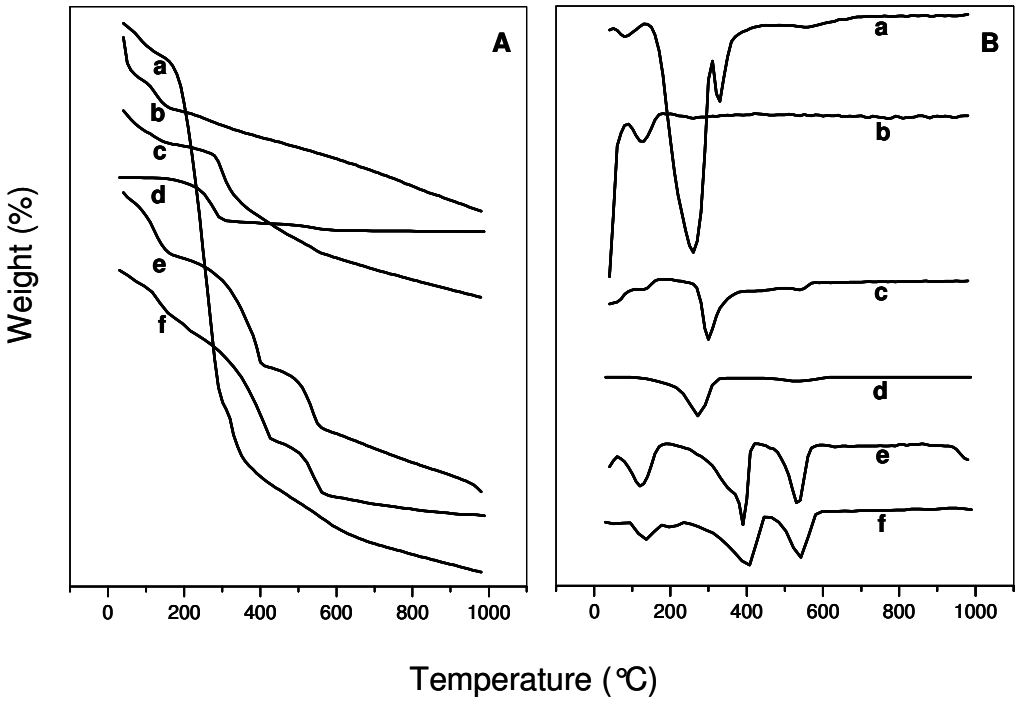

Fig. 3.4. TGA (A) DTG (B) pattern of (a) as synthesized (b) Calcined (c) –OH protected Cl-MCM-41 (d) Neat ligand (L_2Me) (e) Ru-L_2Me-MCM-41 (f) Fe-L_2Me-MCM-41.

These results are confirmed by the comparison of DTG pattern of –OH protected Cl-MCM-41 with that of Ru/Fe-L_2Me-MCM-41 which shows additional weight loss in the range of 460 to 600°C, due to removal of heterogenized metal complex. The DTA pattern further supports the above findings as it shows the strong exothermic peak around 400°C and around 550°C. All these results clearly indicate the successful grafting of organic moieties as well as metal complexes inside the mesoporous channels.

3.4.5. X-ray Photoelectron Spectra (XPS)

Additional support for anchoring of Ru^{II} complexes onto the solid mesoporous material was obtained by the XPS study. From XPS the binding energy values of ruthenium $3d_{5/2}$, $3d_{3/2}$ and $3p_{3/2}$ peaks are observed at 280.6 eV, 284.4 eV and 464.9 eV respectively, which confirm that ruthenium is present in the Ru^{II} state [30]. The N 1s BE

values (400.8eV and 399.8eV) of ligand grafted catalysts (Ru/Fe-L_2Me-MCM-41, respectively) indicate successful grafting of the complex, however shifting in the BE values were observed in each case, which can be attributed to the coordination of N atom to Ru and Fe nuclei and also confirmed the presence of heterogenized ligand in the MCM-41.

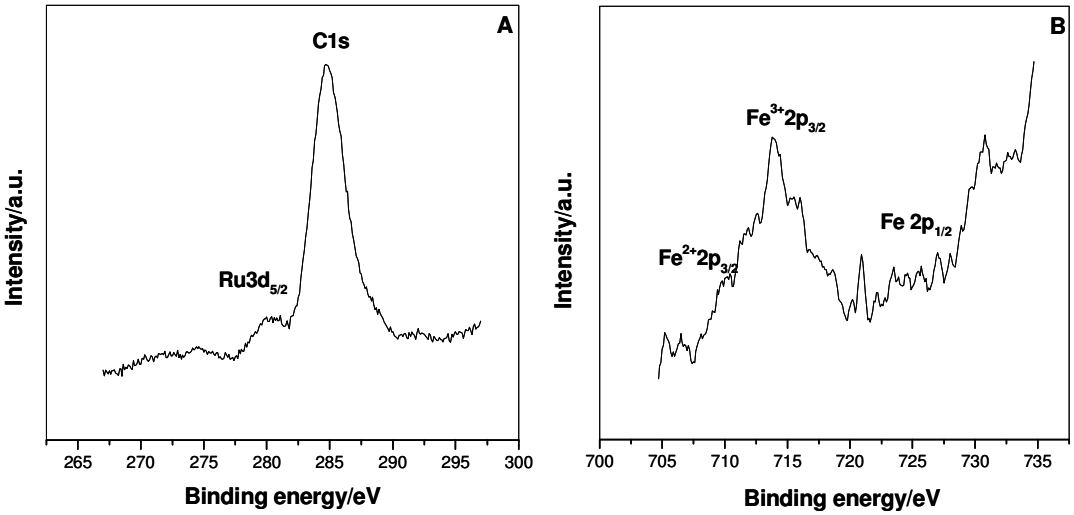

Fig. 3.5. XPS spectrum of (A) Ru-L_2Me-MCM-41 (B) Fe-L_2Me-MCM-41

All these results strongly point towards stable anchoring of the metal complexes onto the mesoporous support. The absence of Ru^{III} was also corroborated by the absence of any signal in the X band EPR signal. The XPS spectrum of Fe-L_2Me-MCM-41 reveals a major binding energy values at 713.8eV and a minor one at 709.8eV, in agreement with the presence of Fe^{III} and Fe^{II} respectively (Fig. 3.5B). The presence of Fe^{III} high spin was confirmed by X band EPR with the presence of a signal at g= 4.3 (Figure not shown).

3.4.6. ^{13}C CP/MAS NMR study

Fig. 3.6. shows liquid state ^{13}C NMR spectrum of 3-CPTMS (spectrum A) and $L_2(Me)_2$ (spectrum B), and the high resolution solid state ^{13}C CP/MAS NMR spectra of Cl-MCM-41(spectrum C) and L_2Me-MCM41 (spectrum D). The liquid state ^{13}C NMR of

3-CPTMS shows four well distinct peaks {C1 (attached with silicon), C2, C3 (attached with chlorine) and methoxy carbon at 6.6, 26.12, 47.17 and 50.39 ppm respectively}.

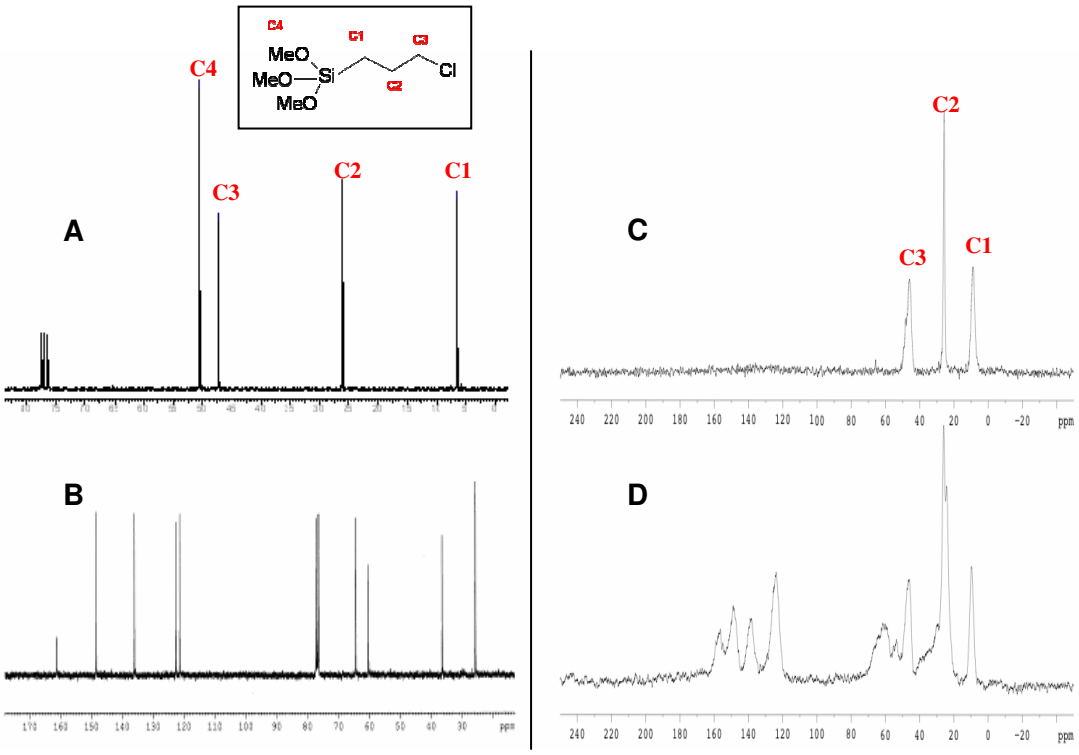

Fig. 3.6. Liquid state (A & B) ^{13}C NMR and solid state (C & D) ^{13}C CP/MAS NMR spectrum of (A) 3-CPTMS (B) Pure ligand $L_2(Me)_2$ (C) Cl-MCM-41 (D) L_2Me-MCM-41

After grafting on MCM-41, the entire peaks broaden and shift to lower field (10.29, 26.34 and 47.99 ppm respectively) corresponding to carbon C1 to C3, respectively, and no peak was observed for methoxy group, which confirms the well grafting of 3-CPTMS onto the support (spectrum C). The grafting of the L_2Me ligand is confirmed by ^{13}C CP / MAS NMR by the presence of new resonances in addition to the ones observed in spectrum C. First, in the 180-120 ppm region, four peaks are observed attributed to ^{13}C resonances of carbons of the pyridyl rings, in a similar range than the ones observed in the liquid spectrum of L_2Me. Moreover, in the region 0-60 ppm, in addition to the resonances of

C1-C3 of the propyl linker, two resonances are attributed to the methylene carbon of the cyclohexane ring (shoulder at 25 and 28) and the broad ones above 50 ppm concerns the resonances of the methylene group and the C-H of the ligand. The attributions were based on Simulation using ACD/CNMR Predictor software (*http://www.acdlabs.com/products/spec_lab/predict_nmr/cnmr/*). Metallation of the ligand with iron was demonstrated by the absence of pyridine resonances and the slight shifts of the propyl resonances, attributed to the paramagnetism of the metal (data not shown).

Then, the ligand was found grafted into the phase and metallated. The absence of any other resonances suggests that most of the chloro propyl groups have reacted with the amino group of the ligands.

3.4.7. Diffuse reflectance UV-vis spectra

The UV-Vis/DRS spectra of the samples were essential for conclusions on the nature of the metal species, especially supporting and complementing previous characterization data of these materials. Fig. 3.7. shows the UV-vis spectra of the pure MCM-41, Ru-L_2Me-MCM-41 and Fe-L_2Me-MCM-41. The absorption above 40000 cm^{-1} corresponds to the siliceous materials [Fig. 3.7a]. The absorption spectrum of Ru-L_2Me-MCM-41 shows at least three metal-to-ligand charge transfer (MLCT) absorption bands in the region at 15917, 20341 and 26517 cm^{-1} [Fig. 3.7b] [31, 32]. The band in the UV region at 32957cm^{-1} is assigned to an intra ligand (π-π^*) transition which is also observed in the case of Fe-L_2Me-MCM-41.

Absorption at 38174 cm^{-1} is typically assigned to Fe^{3+} species, either tetrahedrally coordinated or with higher coordination [Fig. 3.7c] [33, 34]. Because of very low amount, we could not observe peaks corresponding to the Fe^{2+} species (which is supported by XPS and EPR). Generally d-d transitions of Fe^{3+} species are expected in the range of 30000 – 15500 cm^{-1}, but they are symmetry and spin forbidden, and therefore extremely weak [34]. All these results support XPS and EPR studies.

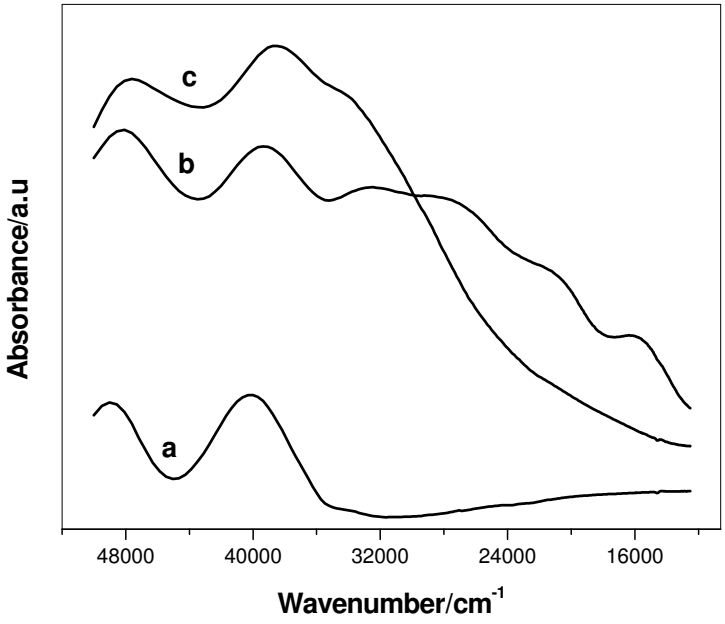

Fig. 3.7. DR UV-vis spectra of (a) pure MCM-41 (b) Ru-L_2Me-MCM-41 (c) Fe-L_2Me-MCM-41

3.4.8. Scanning electron microscopy (SEM)

The scanning electron micrographs show the particle morphology before and after modifications of the MCM-41 samples. The SEM image of calcined, -OH protected Cl-MCM-41; Ru-L_2Me-MCM-41 and Fe-L_2Me-MCM-41 samples are shown in Fig. 3.8. All the four micrographs show considerable differences in the morphology of the mesopore after grafting of each organic moiety. Calcined MCM-41 shows the uniform particle size hexagonal structure. The uniformity of the particle size gets reduced after the grafting of various organic moieties on the inner pore walls of MCM-41 indicates that various treatment conditions can affect the morphology of MCM-41.

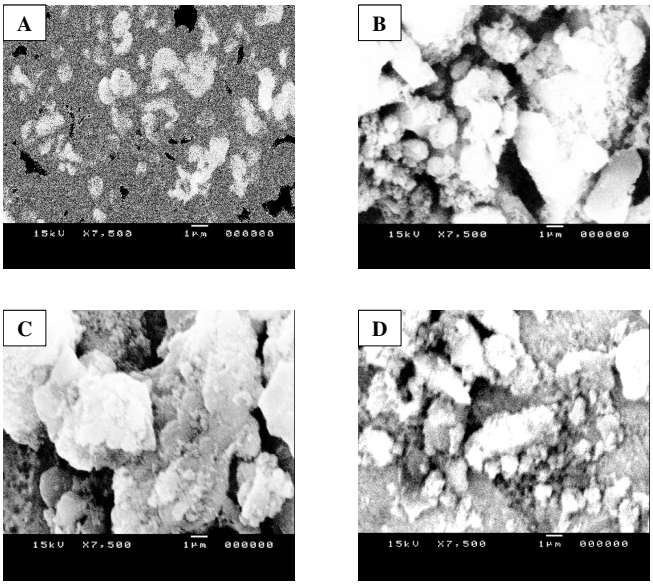

Fig. 3.8. SEM image of (A) Calcined MCM-41 (B) –OH protected Cl-MCM-41 (C) Ru-L_2Me-MCM-41 (D) Fe-L_2Me-MCM-41.

3.4.9. Catalytic activity

Structural characterization results show that the metal complexes are firmly held inside the pore channels of mesoporous MCM-41. Hence the present materials were applied in the liquid phase sulfoxidation of methyl phenyl sulfide with H_2O_2 as the oxidant at room temperature. All the experiments were performed with a ratio catalyst: substrate: oxidant, 1:100:250.

The results obtained after 4.5 h from the sulfoxidation reaction over neat (Fe-$L_2(Me)_2$, Ru$L_2(Me)_2$) complexes as well as immobilized complexes (M-L_2Me-MCM-41) are presented in Table 3.2 and were compared with those obtained from anchored MCM-41 (L_2Me-MCM-41) and without catalyst are also included for comparison. Furthermore, the influence of reaction time, catalyst amount in the case of M-L_2Me-MCM-41 and different oxidizing agents such as H_2O_2, PhIO and TBHP in the case of Ru-L_2Me-MCM-41 are investigated on the conversion of methyl phenyl sulfide, TON, ee and selectivity to the methyl phenyl sulfoxide.

From Table 3.2, it is clear that mesoporous MCM-41 functionalized metal complexes show an enhanced activity (calculated in terms of conversion of methyl phenyl sulfide and turnover number, TON) compared to the L_2Me-MCM-41 solid phase and in the absence of catalyst. Moreover, the selectivity towards the sulfoxide (sulfoxide/sulfone + sulfoxide) over all catalysts was found between 81 and 92 %, a greater value than the one of the uncatalyzed reaction (70 %). To study the effect of catalyst concentration, the conversion of methyl phenyl sulfide was reached 100 % and 90 % over Ru-L_2Me-MCM-41 and Fe-L_2Me-MCM-41 after 1.1 h and 6 h, respectively, when the catalyst amount was used 100 mg instead of 50 mg.

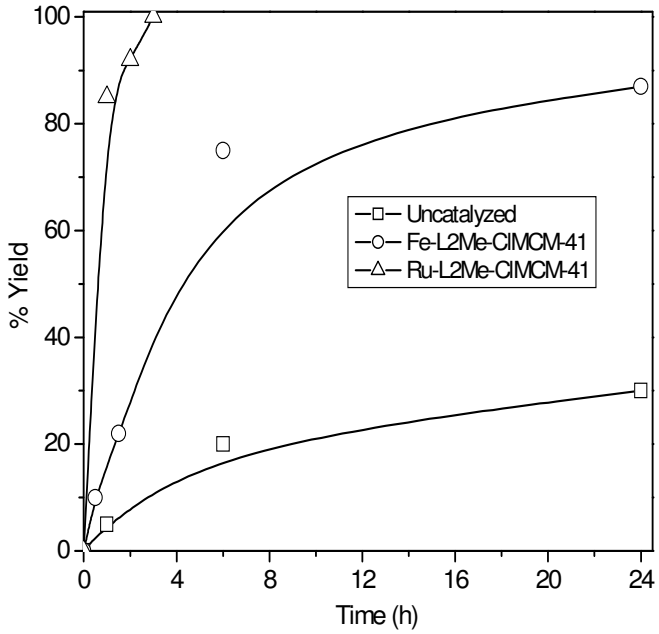

Fig. 3.9. Conversion of methyl phenyl sulfide (%) vs. reaction time over various catalysts. Reaction conditions as in footnote of Table 3.2.

The reaction efficiency of the solid catalysts was found to be metal dependent. The conversion of methyl phenyl sulfide as a function of reaction time over Ru-L_2Me-MCM-41, Fe-L_2Me-MCM-41 and without catalyst are given in Fig. 3.9. Ru-L_2Me-MCM-41 showed considerably superior performance throughout the reaction and it gave about 100

% conversion of methyl phenyl sulfide in 4 h whereas Fe-L_2Me-MCM-41 reached up to 75 % conversion level in 5.5 h of reaction time.

Interestingly, the heterogeneization of metal complex caused some remarkable changes as the reactivity was concerned. First, homogeneous Fe-$L_2(Me)_2(CF_3SO_3)_2$ led to a less selective sulfoxidation than its grafted counterpart. In the homogeneous case, the total conversion was attained in 5 min with only 36% of sulfoxide, but other products coming from a S-dealkylation were formed. Then, the grafting of $FeL_2(Me)$ on MCM-41 led to a different reaction pathway, that led to a neat selective oxygen transfer reaction. Second, the reaction time of the sulfoxidation was greatly increased when the MCM-41 support was present (5 min against 4 to 10 hours). This strongly suggests that the reaction took place into the pores where the presence of oxidant and substrate are regulated by the pore size. Third, the grafting of Ru $(L_2(Me)_2)Cl_2$ initiates an enantioselective reaction whereas only racemic mixture is formed in homogeneous catalysis. It has to be noted that the grafting of FeL_2Me did not alter its asymmetric efficiency. Finally, the influence of various oxidizing agents such as H_2O_2, PhIO and TBHP was also observed in the sulfoxidation of methyl phenyl sulfide using Ru-L_2Me-MCM-41 catalyst. The H_2O_2 gave higher conversion (98 %) compared to the PhIO (35%) and TBHP (20%). However, no significant changes were observed in the selectivity of sulfoxide and ee's (Table 3.2). The catalytic properties of the both heterogeneous catalysts unambiguously support that the chiral L_2Me ligand is inserted into the pores, leading to high selectivity and good efficiency.

Furthermore, the epoxidation of styrene was also carried out over Fe-L_2Me-MCM-41 for 26 h at 70 °C in DMF using H_2O_2 as an oxidant. The ratio of catalyst: substrate: oxidant was kept 1:135:135. The main products of the reaction were benzaldehyde and styrene epoxide. The results were also compared with the homogeneous catalyst, Fe-$L_2(Me)_2$, and in the absence of catalyst under the similar reaction conditions except setting the reaction time at 6 h. The conversion of styrene, selectivity to styrene epoxide and TON over Fe-L_2Me-MCM-41 and Fe-$L_2(Me)_2$ were found to be 42 %, 75 %, 39 and 32 %, 82 % and 33, respectively. In this case, no major

difference was observed regarding the efficiency of the two catalysts. In the absence of catalyst, no epoxide was detected in the epoxidation of styrene.

Table 3.2. Oxidation of methyl phenyl sulfide promoted by supported Ru and Fe catalysts.

Catalysts	Conversion (%) (time h)	Selectivity to Sulfoxide (%)	TON[a]	ee
No catalyst	23 (4.5)	70	-	-
L_2Me-MCM41	16 (4.5)	85	-	-
RuL_2Me-MCM41	98 (4.5)	90	90	7
FeL_2Me-MCM41	75 (4.5)	81	50	2
Fe-$L_2(Me)_2$[b]	100 [f] (5min)	36	42	2
Ru-$L_2(Me)_2$[c]	95 (5 min)	93	82	0
RuL_2Me-MCM41(100mg)	100 (1.1)	88	46	9
FeL_2Me-MCM41(100mg)	90(6)	80	41	5
RuL_2Me-MCM41	35 (4.15)[d]	92	31	2
	20 (4)[e]	86	17	9

Reaction conditions: Catalyst amount = 50 mg; Methyl phenyl sulfide = 1 mmol; H_2O_2 (30%) = 2.5 mmol; methanol = 3 mL; reaction temperature = Room Temperature. [a] TON = (mmol of sulfoxide + mmol of sulfone)/mmol of Ru or ligand grafted; [b] to be changed by amount of Ru/Fe$L_2(Me)_2$ corresponding to concentration of iron complex in supported catalysts (i.e. 1% moles versus substrate); [c] Amount of Ru/$L_2(Me)_2$ taken; [d] Oxidation with PhIO; [e] Oxidation with TBHP; [f] mass balance was under 100% revealing the presence of undefined products.

No color changes have been observed during the reaction, excluding any characterization of transient intermediates. On the other hand, literature reports over the homogeneous catalyst Fe$L_2(Me)_2$ [35] reveal that a high valent iron species was responsible for alkane and alkene oxidation. We may suggest that in the case of

sulfoxidation either a peroxo adduct of the complex or an oxene species is involved in the oxidation process.

3.4.10. Recycling studies

In order to ascertain whether the activity of the immobilized catalysts arise from true heterogeneous catalysts, the stability of the metal complexes over MCM-41 (Ru-L_2Me-MCM-41, Fe-L_2Me-MCM-41) were probed three times (fresh + two cycles) in the sulfoxidation of methyl phenyl sulfide using H_2O_2 as an oxidant. The results are presented in Table 3.3. After workup of reaction mixture, the catalyst was separated by filtration, washed three times with methanol and dried in vacuum before use in the next experiment. The recovered catalyst after each reaction was analyzed for nitrogen content to see the amount of complex leached out from the solid phase. Elemental analysis showed that N_2 content from Ru-L_2Me-MCM-41 and Fe-L_2Me-MCM-41 decreased from 0. 41 to 0.21 % and 1.1 to 0.25 %, respectively, after use from fresh to 2^{nd} recycle, respectively. Similarly, the conversion of methyl phenyl sulfide decreased from 97 to 70 % and 92 to 72 % when Ru-L_2Me-MCM-41 and Fe-L_2Me-MCM-41 were recycled from fresh to the second cycle, respectively. However, the selectivity to the methyl phenyl sulfoxide and ee did not change appreciably after each recycling. The loss of metal complex by leaching from the mesoporous MCM-41 phase is responsible for the decrease in catalytic activity of both catalysts after each recycle.

Table 3.3. Recycling of M-L_2Me-MCM-41 catalysts in phenyl methyl sulfide reaction

Catalyst	Conversion (%)	Selectivity (%)	ee (%)	N content (%)
RuL_2Me-MCM41[a]				
Fresh	97	91	7	0.41
Recycle I	71	70	5	
Recycle II	70	96	4	0.21
FeL_2Me-MCM41[b]				
Fresh	92	87	2	1.10
Recycle I	82	80	2	
Recycle II	72	94	2	0.25

[a]Reaction time = 4.5 h; [b]Reaction time = 23 h; Reaction conditions as in footnote of Table 3.2; Recycling conditions are given in experimental section.

3.5. CONCLUSIONS

In conclusion, iron and ruthenium chiral complexes were successfully grafted on to MCM-41 support which was modified by 3-CPTMS. The resulting materials were subjected to the different characterization techniques, such as XRD, FTIR, TG-DTA, UV-Vis, solid state ^{13}C NMR and EPR which reveal that the metal complexes are firmly attached to the modified MCM-41 support. The screening of the catalysts, Ru/Fe-L_2Me-MCM-41, was done in the sulfoxidation reaction of thioanisole using H_2O_2 as an oxidant. The above results indicate that the heterogenized chiral metal complexes (Ru/Fe-L_2Me-MCM-41) plays an important role in the sulfoxidation of thioanisole, which give higher activity, TON and comparable enantiomeric excess compared to the homogeneous counterpart. Recycling studies show that chiral metal complex only partially leaches out during the reaction which indicates that the grafting procedure of the metal complexes over Cl-MCM-41 is effective in meeting the objectives.

3.6. REFERENCES

[1] D.E. De Vos, M. Dams, B.F. Sels, P. A. Jacobs, *Chem Rev.,* 102, **2002**, 3615.

[2] a) K. Neimann, R. Neumann, A. Rabion, R.M Buchanan, R. H. Fish, *Inorg. Chem.,* 38, **1999**, 3575 ; b) W. A. Carvalho, M. Wallau, U Schchardt, *J. Mol. Catal. A: Chem.,* 144, **1999**, 91.

[3] a) F. Fache, E. Schulz, M. Lorraine Tommasino and M. Lemaire, *Chem. Rev.,* 100, **2000**, 2159 ; b) L. Canali, D.C. Sherrington, *Chem. Soc. Rev.,* 28, **1999**, 85; c) V. Schünemann, A.X. Trautwein, I. M.C. Rietjens, M. G. Boersma, C. Veeger, D. Mandon, R. Weiss, K. Bahl, C. Colapitro, M. Piech, R. N. Austin, *Inorg. Chem.,* 38, **1999**, 4901 and references therein.

[4] a) M. Fontecave, S. Ménage, C. Duboc-Toia, *Coord. Chem. Rev.,* 178-180, **1998**, 1555. b) M. Costas, K. Chen, L. Que. Soc Jr, Coord. *Chem. Rev.*, 200-202, **2000**, 517 and references therein

[5] M. Costas, A.K. Tipton, K. Chen, D-H. Jo L. Que Jr, *J. Am. Chem. Soc.,* 123, **2001**, 6722.

[6] a) J. Legros, C. Bolm, *Angew. Chem. Int. Ed.,* 43, **2004**, 4225. b)Y. Mekmouche, H. Hummel, R.Y.N Ho, L. Que jr. , V. Schuenemann, F. Thomas, A.X. Trautwein, C. Lebrun, K. Gorgy, J.C Lepretre, M-N Collomb, A. Deronzier, M. Fontecave, S. Menage, *Chem Eur J.,* 8, **2002**, 1196.

[7] C.T. Kresge, M.E. Leonowicz, W.J. Roth, J.C. Vartuli, J. S. Beck, *Nature*, 359, **1992**, 710.

[8] J. S. Beck, J. C. Vartuli, W. J. Roth, M. E. Leonowicz, C. T. Kresge, K. D. Schmitt, C. T. W. Chu, D. H. Olson, E. E. Sheppard, S. B. McCullen, J. B. Higgins, J. L. Schlenker, *J. Am. Chem. Soc.,* 114, **1992**, 10834.

[9] A. Corma, M. T. Navarro, J. P. Pariente, *J. Chem. Soc., Chem. Commun.*, **1994**, 147.

[10] P. T. Tanev, M. Chibwe, T. J. Pinnavaia, *Nature,* 368, **1994**, 321.

[11] S. Shylesh, A. P. Singh, *J. Catal.,* 228, **2004**, 333.

[12] D. Brunel, A. Cauvel, F. Fajula, & F. DiRenzo, In Studies in Surface Science and Catalysis 97 (eds Bonneviot, L., et al.) 173 – 180 (Elsevier, Amsterdam, 1995).

[13] J. J. Diaz, K. J. Balkus, F. Jr, Bedioui, V. Kurshev, L. Kevan, *Chem. Mater.,* 9, **1997**, 61.

[14] C. W. jones, K. Tsuji and Mark. E. Davis, *Nature*, 393, **1998**, 52.

[15] T. Asefa, M.J. Maelachlan, N. Coombs, G. A. Ozin, *Nature,* 402, **1999**, 867.

[16] S. Inagaki, S. Guan, Y. Fukushima, T. Ohsuna, O. Terasaki, *J. Am. Chem. Soc.,* 121, **1999**, 9611.

[17] R. J. P. Corriu, D. Leclereq, *Angew. Chem.,* 108, **1996**, 1524.

[18] A. J. A. Cobb, C. M. Marson, *Tetrahedron*, 61, **2005**, 1269.

[19] M. Costas, Jan-Uwe Rohde, A. Stubna, R. Y. N. Ho, L. Quaroni, E. Munck, and L. Que, Jr, *J. Am. Chem. Soc.,* 123, **2001**, 12931.

[20] J-X Gao, T. Ikahira, R. Noyori et al., *Organometallics,* 15, **1996**, 151087.

[21] A. Ghosh, Rajiv Kumar, *J. Catal.,* 228, **2004**, 386.

[22] J. Chen, Q. Li, R. Xu, F. Xiao, *Angew. Chem. Int. Ed. Engl.,* 34, **1995**, 2694.

[23] M. D. Alba, Z. Luan, J. Klinowski, *J. Phys. Chem.,* 100, **1996**, 2178.

[24] The Aldrich Library of Infrared spectra, Charles. J. Pouchert.

[25] A. N. Parvulescu, B. C. Gagea, M. Alifanti, V. Parvulescu, V. I. Parvlescu, S. Nae, A. Razus, G. Poncelet, P. Grange, *J. Catal.,* 202, **2001**, 319.

[26] N. C. Marziano, L. D. Ronchin, C. Tortato, A. Zingales, A. A. Sheikh-Osman, *J. Mol. Catal. A: Chem.,* 174, **2001**, 265.

[27] M. J. Hudson, J. A. Knowles, *J. Mater. Chem.*, 6, **1996**, 89.

[28] M. Schneider, A. Baikar, *J. Mater. Chem.,* 5, **1992**, 587.

[29] S. C. Laha, P. Mukherjee, S. R. Sainkar, R. Kumar, *J. Catal.,* 207, **2002**, 1.

[30] C. Battistoni, C. Furlani, G. Mattogno, G. Tom. *Inorg. Chim. Acta,* 21, **1977**, L25.

[31] T. R. Weaver; T. J. Meyer; S. A. Adeyemi; G. M. Brown; R. P. Eckberg; W. E. Hatfield; E. C. Johnson; R. W. Murray; D. Untereker, *J. Am. Chem. Soc.,* 97,

1975, 3039.

[32] Md. K. Nazeeruddin, S. M. Zakeeruddin, R. Humphry-Baker, S. I. Gorelsky, A. B. P. Lever, M. Gratzel, *Coord. Chem. Rev.,* 208, **2000**, 213.

[33] S. Bordiga, R. Buzzoni, F. Geobaldo, C. Lamberti, E. Giamello, A. Zecchina, G. Leofanti, G. Petrini, G. Tozzolo, G. Vlaic, *J. Catal.,* 158, **1996**, 486.

[34] A. Bruckner, R. Luck, W. Wieker, B. Fahlke, H. Mehner, *Zeolites*, 12, **1992**, 380.

CHAPTER-4

METAL TRIFLATE IMMOBILIZED MESOPOROUS SBA-15

4.1. INTRODUCTION

Metal triflates and other triflate derivatives are known to serve as efficient homogeneous catalysts in the Lewis acid-catalyzed reactions for organic synthesis [1]. In addition to strong Lewis acidity, these compounds are found to exhibit a reasonably good tolerance towards water. A large number of metal triflate catalysts have therefore been reported for the Friedel–Crafts alkylation and acylation reactions. Olah et al. reported that the triflates of boron, aluminium, and gallium serve as very efficient Friedel–Crafts catalysts for the alkylation, isomerization, and acylation reactions [2]. Tsuchimoto et al. found that $Sc(OTf)_3$ was the most efficient catalyst among the rare earth metal triflates screened for the benzylation of benzene with benzyl alcohol [3]. Several studies have been reported in the last few years on the heterogenization of triflic acid, in order to facilitate the separation of the catalyst from reaction medium and also to enhance the catalyst efficiency by providing a higher dispersion [4-8]. Accordingly, certain silica-supported triflates and triflic acid are found to be active and selective catalysts for certain organic synthesis reactions, such as: rearrangement of α-pinene oxide to campholenic aldehyde [6], polymerization and depolymerization of cyclic ethers [5], Friedel–Crafts reactions [7, 8], and alkylation of isobutane with *n*-butene [9]. There are, however, very few reports on the catalytic properties of metal triflates supported on the ordered mesoporous silica. The present study was taken up with an objective to incorporate several metal triflates in the pores of mesoporous SBA-15. The mesoporous molecular sieve SBA-15 was chosen because of its better thermal stability and its unique pore topology comprising of the hexagonally arranged parallel mesopore channels [10, 11]. Such pore structures are known to serve as ideal hosts where the mesopore channels assist in the transport of reactants or products without much diffusional resistance, and at the same time they provide a large surface area to enhance the number of the reaction sites. In this paper, we describe the catalytic properties of different metal triflates, viz. $La(OTf)_3$, $Ce(OTf)_4$, $Y(OTf)_3$, and $Zn(OTf)_2$, supported on SBA-15 for the acylation of naphthalene using *p*-toluoyl chloride as acylating agent to produce naphthalen-2-yl(p-tolyl)methanone (2-acyl naphthalene). These compounds find application as a dye intermediate and also in the photoisomerization of cis- and trans-stilbene. In situ IR study

of pyridine adsorption was taken up to monitor the triflate-induced acid sites responsible for the FC reaction mentioned above.

4.2. EXPERIMENTAL

4.2.1. Materials

The precursor chemicals, i.e. Pluronic 123 (P123, Average Mol.Wt = 5800), *p*-Toluoyl Chloride (Aldrich), Tetraethylorthosilicate (Merck), Metal triflates (Acros Organics) and naphthalene (S. D. fine chemical) were of research grade and were utilized without further purification.

4.2.2. Synthesis of siliceous SBA-15

The synthesis of mesoporous SBA-15 was carried out hydro thermally under the autogeneous pressure of an autoclave. The polymer surfactant P123 was used as a template and hydrochloric acid served as a mineralizer. The following was the gel composition.

0.043 TEOS: 4.4 g P123 M_{avg} = 5800 [EO_{20}-PO_{70}-EO_{20}]: 8.33 H_2O: 0.24 HCl

Typically, 4.4 g of tri block co-polymer dispersed in 30 g distilled water was stirred for 1.5 h. To the resultant solution, 120 g of 2M HCl was added under stirring and the stirring was continued for 2 h. Finally 9 g of TEOS was added drop wise and the mixture was maintained at 40 °C for 24 h with continuous stirring. The mass was submitted to a hydrothermal treatment (100 °C, 48 h) under static condition. The precipitate was filtered, washed with distilled water, dried in an oven (90 °C, 12 h) and then calcined in air (500 °C, 6 h) to remove the template completely.

The catalysts were prepared by soaking of calcined SBA-15 sample in acetonitrile solution of a metal triflate powder, accompanied with continuous stirring for 8-10 h. The excess of acetonitrile was evaporated to dryness under reduced pressure, followed by complete drying at 120 °C. The functionalized samples are designated in the text as Zn-

Tf (30)/SBA, where the number in the parentheses represents the triflate loading in mol%.

4.2.3. Characterization

The powder X-ray diffraction patterns were recorded by using X'Pert Pro (M/s Panalytical) diffractometer using Ni filter, CuKα radiation and proportional counter as detector. A divergent slit of 1/8 ° in the primary optics and an anti scatter slit of 1/4 ° in the secondary optics were employed to measure the data in the low angle region. The XRD patterns were recorded in 2θ range between 0.5 and 5 degrees at a scan rate of 1 °/min. N_2 adsorption experiments were conducted at 77K using a NOVA 1200 (Quanta chrome) apparatus for analyzing the surface area (BET) and pore-size distribution in the synthesized samples. Pore-size distribution was obtained by using the BJH pore analysis applied to the desorption branch of the nitrogen adsorption/desorption isotherms. FT-IR spectra of solid samples were recorded in the range of 4000 – 400 cm^{-1} to monitor the nature of the triflate bonding with host matrix. Thin sample wafers (ca. 20 mol% of catalyst mixed with KBr powder) were used for this purpose after proper drying and the spectra were recorded in transmission mode using a Shimadzu model - 8201 spectrophotometer. Thermo gravimetric analyses (TGA and DTA) were performed using a Diamond TG/DTA instrument at a heating rate of 10 °C/min under airflow. Experiments on the saturation adsorption of ammonia and its subsequent temperature-programmed desorption (TPD-NH_3) were performed on a Micromeritics Autochem 2910 instrument. About 0.1 g of a fresh sample was placed in a U-shaped, flow-through, quartz micro reactor for each experiment. The catalyst was activated at 220 °C for 2 h under helium flow (30 ml/min) and then cooled to 100 °C before being exposed to ammonia. Sample was flushed again in He for 1h to remove any physisorbed ammonia, and desorption profile was then recorded by increasing the sample temperature from 100 to 900 °C at a ramp rate of 10 °C/min.

4.2.4. Pyridine IR studies

The nature of the acid sites in different samples was monitored by recording the transmission - mode IR spectra of adsorbed pyridine vapor. A Thermo Nicolet (model Nexus 870) FTIR equipped with a high-pressure high-temperature stainless steel cell, fitted with water-cooled CaF_2 windows and described previously in detail, was utilized for this purpose [12]. Self-supporting wafers (~50 mg) of 25 mm diameter, placed in a sample holder block, were in direct contact with a chromel-alumel thermocouple. For acidity measurements, the samples were heated in situ for 8-10 h at 550-575 K under vacuum (~1×10^{-3} Torr) and then exposed at 400 K to multiple doses of pyridine (~1.0 μmol each) for a saturation coverage. A gas mixture comprising of nitrogen + pyridine vapor was utilized for this purpose. The gas pressure in the IR cell was monitored with the help of digital capacitance manometer. IR spectra were plotted at 400 K after equilibrating a sample for 15-20 min subsequent to each pulse injection. Spectra were also recorded at room temperature after post-exposure cooling of the sample to room temperature followed by pumping. A total of 300 scans were co-added for plotting of the each spectrum at a resolution of 4 cm^{-1}. The numbers given in the parentheses in some of the IR spectra represent the relative absorbance values for comparison.

4.2.5. Friedel Crafts (FC) acylation reaction of naphthalene with p-toluoyl chloride

Naphthalene and *p*-toluoyl chloride were used without further purification. The catalyst was activated at 100 °C for 2h and the liquid-phase FC reaction was performed in batch mode using a 50 ml round bottom flask fitted with a condenser. The reaction vessel was maintained at the temperatures between 80 -160 ^{o}C by using an oil bath. In a typical run, a mixture of naphthalene (10 mmol), *p*-toluoyl chloride (10 mmol), nitrobenzene (5 ml) and activated catalyst (0.1 gm), was magnetically stirred and heated to attain the desired reaction temperature. The product samples were withdrawn at regular intervals of time and analyzed periodically on a gas chromatograph (Agilent 6890N) equipped with a flame ionization detector and a capillary column (5μm thick cross-linked methyl silicone

gum, 0.2mm × 50m long). The main product, naphthalen-2-yl(p-tolyl)methanone was separated by column chromatography and confirmed by GC-MS, ^{1}H and ^{13}C NMR analysis. ^{1}H NMR ($CDCl_3$, 200MHz) δ 2.42 (s, 3H), 7.23 - 8.25 (m, 11 H) ppm. ^{13}C NMR ($CDCl_3$, 50MHz) δ 21.71, 124.34, 125.7, 126.36, 127.08, 127.31, 128.33, 129.14, 129.17, 130.23, 130.56, 130.92, 144.20, 144.56, 197.75.

4.3. RESULTS

4.3.1. X-ray diffraction (XRD)

Fig. 4.1 shows the representative XRD patterns of calcined SBA-15, without (curve a) and after functionalization with 30 mol% of different metal triflates (curve b-e). The triflate containing samples exhibited a XRD pattern similar to that of SBA-15, where three well-resolved diffraction peaks due to {100}, {110}, and {200} reflections were observed.

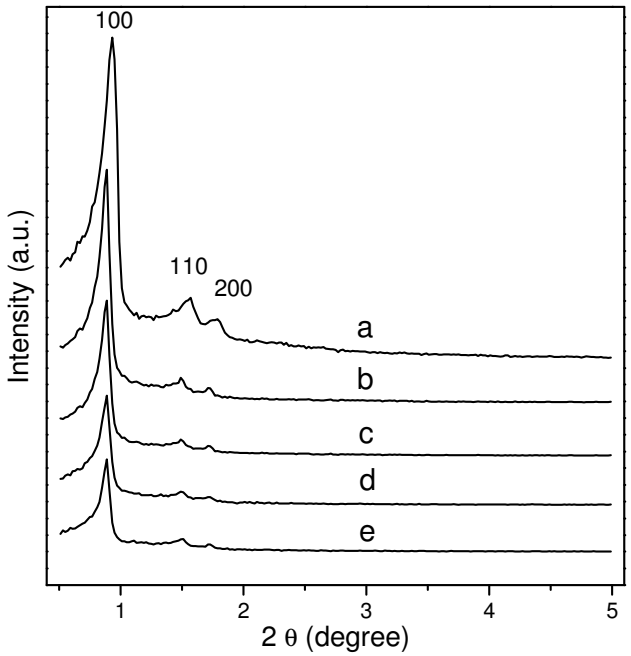

Fig. 4.1. Low angle powder-XRD patterns of metal triflate loaded SBA-15. (b) Zn-Tr(30)/SBA, (c) Y-Tr(30)/SBA, (d) La-Tr(30)/SBA, (e) Ce-Tr(30)/SBA. Curve (a) is a comparative XRD pattern of pure SBA-15.

These reflections correspond to the two dimensional hexagonal *p6mm* symmetry, a characteristic of well defined SBA-15 mesoporous material. The XRD patterns in Figs. 4.1(b-e) thus confirm the integrity of the characteristic hexagonal structure of SBA-15 in the triflate loaded samples. A progressive decrease observed in the intensity of XRD lines, however, reveals a partial loss of long-range order of SBA-15 due to the incorporation of triflate molecules. The values of unit cell parameter (a_0) of SBA-15 and corresponding triflate-modified samples are given in Table 4.1.

4.3.2. Nitrogen sorption studies

The functionalized SBA-15 samples displayed type-IV isotherm with H1 hysteresis, a characteristic feature of the highly ordered mesoporous materials. The BET surface area (S_{BET}) and total pore volume (V_{total}) of SBA-15 was found to decrease progressively with increasing loading of metal triflate, as shown in the data given in Table 1.

Table 4.1. Physico-chemical properties of metal triflate- grafted SBA-15 catalysts

Sample	d_{100} (Å)	a_o (Å)[a]	Total acidity mmol NH_3/g[b]	Pore diameter (Å)	Pore Volume (cm^3g^{-1})	S_{BET} ($m^2\ g^{-1}$)
Calcined SBA-15	93.85	109.5	0.01	84.3	0.94	684.3
Zn-Tr (10)/SBA	100.31	115.2	2.85	81.0	0.90	628.3
Zn-Tr (30)/SBA	101.31	116.4	9.13	75.0	0.74	550.3
Ce-Tr (30)/SBA	101.31	116.4	6.96	-	-	575.3
Y-Tr (30)/SBA	101.31	116.4	6.20	-	-	525.6
La-Tr (30)/SBA	101.31	116.4	7.01	-	-	518.6

[a]Unit cell parameter (a_o) = d_{100} x $2/\sqrt{3}$.
[b]Measured by using TPD-NH_3 method.

Thus, in a representative case, the loading of 30 mol% zinc triflate in SBA-15 resulted in the decrease of surface area from 684.3 to 550.3 $m^2 g^{-1}$. This trend may be attributed to the ingress of triflate molecules in the pore structure and also because of the partial collapse of host structure, as revealed by the XRD results in Fig. 4.1.

4.3.3. Thermal analysis

Curve (a) in Fig. 4.2 presents the differential thermogravimetry (DTG) pattern of pure zinc triflate while curves (b) and (c) are for the SBA-15 samples functionalized (30 mol %) with the triflates of Zn and La, respectively. As seen in Fig. 4.2, whereas pure zinc triflate decomposes at ~540 °C, its decomposition in case of SBA supported samples occurs at a lower temperature (~435 °C). A similar lowering of TG peak temperature was observed in the case of SBA-15 samples containing other metal triflates (Fig. 4.2c).

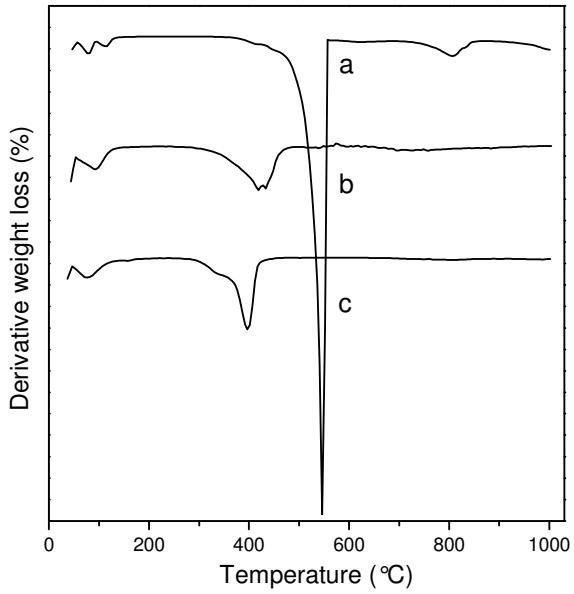

Fig. 4.2. Derivative thermogravimetric patterns of (a) pure zinc triflate, (b) Zn –Tr (30)/SBA and (c) La-Tr (30)/SBA

This may be ascribed to the reaction of highly dispersed $Zn(OTf)_2$ with the surface hydroxyl groups on SBA-15 at elevated temperature to produce ZnF_2 and $ZnSO_4$ [13]. A

similar observation has been reported in the earlier studies on the triflic acid supported over mesoporous materials [4, 6]. The –OH groups on silica are found to promote such thermal reactions of triflic acid [14]. Since no measurable weight loss is observed at the temperatures lower than 400 ^{o}C, besides a small peak at about 100 ^{o}C due to a small amount of adsorbed moisture (Figs. 4.2b, c), it is imperative that the triflate molecules are immobilized firmly in the channels of SBA-15 and are thermally stable at the temperatures up to 400 ^{o}C.

4.3.4. Acidity measurement

Curves (b-e) in Fig. 4.3 exhibit the temperature programmed desorption (TPD) profiles of ammonia, recorded on SBA-15 samples containing different metal triflates at a uniform loading of 30 mol%. The pristine SBA-15 showed negligibly small adsorption of ammonia and the comparative TPD profile is shown in curve (a). The intensity of the TPD profiles in curves b-e was found to vary progressively with triflate loading. The density of acid sites in different catalyst samples, as computed from the area under TPD profile, is included in Table 4.1. As shown in Table 4.1, the density of the acid sites is considerably higher in zinc triflate loaded SBA-15, as compared to the samples containing rare earth triflates.

Furthermore, the TPD results in Fig. 4.3 display the presence of at least three distinct ammonia adsorption sites. The high temperature of the desorption peaks (>325 °C) in this figure is indicative of the strong acidic character of the synthesized catalysts. These results also reveal that the acid strength distribution may depend considerably on the cation associated with a triflate molecule. For instance, the Zn triflate containing sample exhibited a distinct NH_3 TPD peak at a higher temperature of ~450 ^{o}C (curve b), as compared to the samples containing similar loading of rare earth metal triflates (Fig. 4.3, curves c-e).

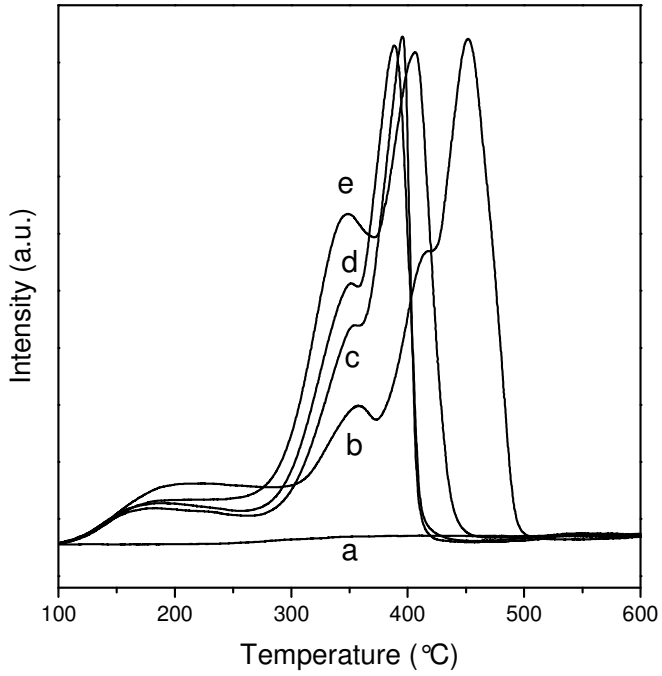

Fig. 4.3. Ammonia TPD profiles of (a) pure SBA-15, (b) Zn-Tr (30)/SBA, (c) Ce-Tr (30)/SBA, (d) La-Tr (30)/SBA and (e) Y-Tr (30)/SBA

These results conform with the pyridine –IR results described below, where the presence of distinct Lewis acid sites in Zn-Tr-SBA is demonstrated

4.3.5. IR spectroscopy results

4.3.5.1. FT-IR Spectra of triflate loaded SBA-15

Curve (a) in Fig. 4.4 presents the mid-IR region difference spectrum of a representative Zn-Tr (30)/SBA catalyst, recorded after compensating for the framework vibrational bands of pure SBA-15 in this region (curve b). Corresponding IR spectrum of pure zinc triflate is shown in curve (c) of this figure for comparison. The assignment of different vibrational bands is given in Table 4.2. A comparison of the IR spectra (a) and

(c) in Fig. 4.4 reveals clearly that the frequency of different vibrational bands of zinc triflate molecules remained mostly unchanged on

Table 4.2. Assignment of IR band frequency (cm^{-1}) of zinc triflate, without and after grafting in SBA-15

IR band frequency (cm^{-1})[a]		Assignment
Zinc triflate	**Zn-Tr (30)/SBA**	
520	519	δ_{as} (SO_3)
576	578	δ_{as} (CF_3)
645	650	δ_s (SO_3)
768	–	δ_s (CF_3) + ν_s (CS)
1033	1035	ν_s (SO_3)
1180	1182	ν_{as} (CF_3)
1245	–	ν_s (CF_3)
1270	1270	ν_{as} (SO_3)
1346	–	ν_{as}(SO_3)

[a] -assignments as per the references [17, 18], Notations: ν = bond stretch; δ = group angle deformation; *s* = symmetric stretch; as = asymmetric stretch

immobilization in mesoporous SBA-15 (see Table 4.2). Significant changes are, however, noticeable in the relative intensity of different stretching and deformation mode vibrational bands arising due to SO_3 and CF_3 groups of the triflate ions. These results are indicative of certain perturbations experienced by the occluded triflate molecules, as discussed later in the text.

4.3.5.2. Effect of triflate and pyridine loading on hydroxyl region bands of SBA-15

The IR spectrum of as-synthesized SBA-15, recorded at 400 K after evacuation of the sample at 525 K for 8h, exhibited a prominent sharp band at 3740 cm^{-1} in addition to a weak and broad absorption band in 3650 - 3450 cm^{-1} region. As is well reported, the 3740 cm^{-1} band arises due to the non-acidic terminal silanols stretching vibrations while the lower frequency absorption band is assigned to the hydrogen bonded internal SiOH groups in mesoporous silicates [15].

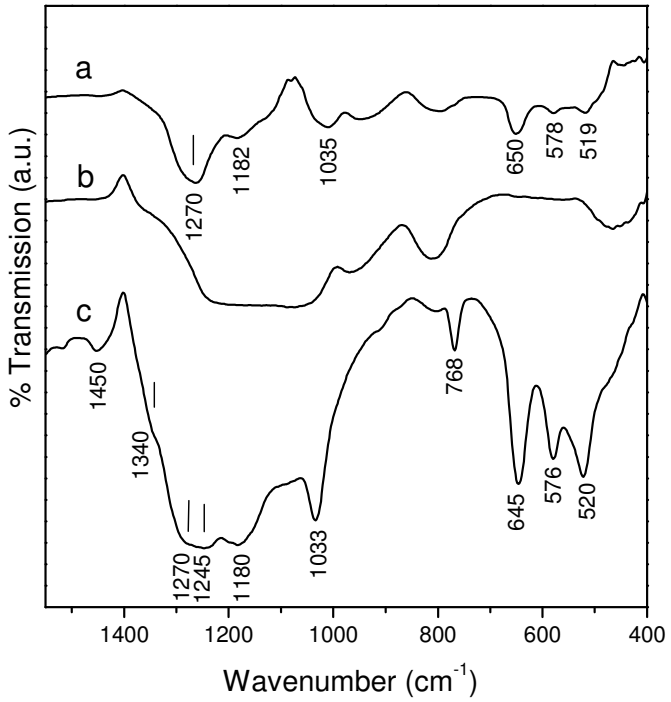

Fig. 4.4. FT-IR spectrum of (a) Zn-Tr (30)/SBA-15 after compensating for theframework vibrations of SBA-15 (b) pure SBA-15 and (c) pure Zn $(OTf)_2$.

The intensity of both these ν(OH) vibrational bands was found to decrease progressively when the increasing amounts of a particular metal triflate were loaded into SBA-15. No measurable shift was observed in the frequency of these ν(OH) bands in all the samples, irrespective of the nature or the amount of triflate introduced. Plot (a) in Fig. 4.5 shows

the progressive variation in the intensity of 3740 cm^{-1} ν(OH) band as a function of zinc triflate loading.

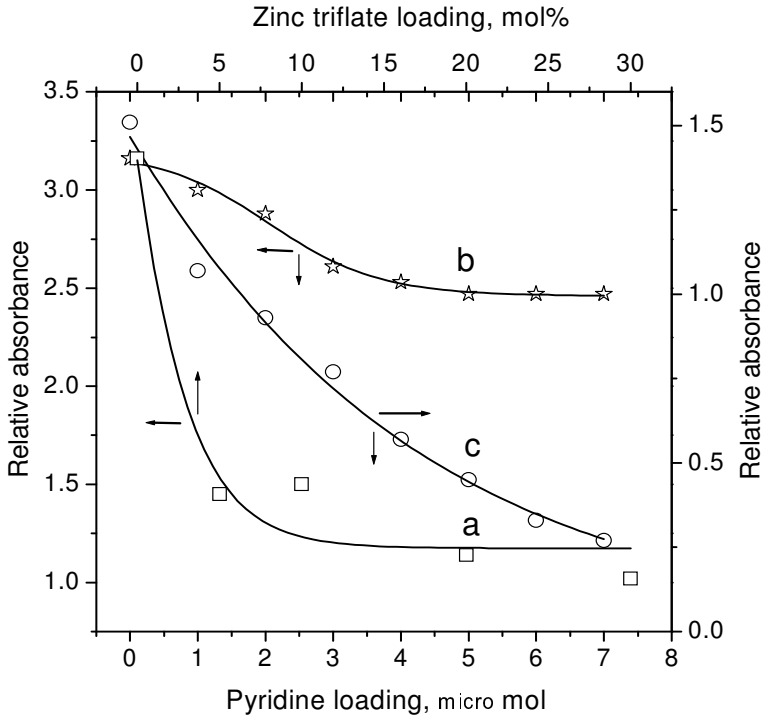

Fig. 4.5. The relative intensity (absorbance) of 3740 cm^{-1} band as a function of: curve (a) loading of zinc triflate in SBA-15, (b) pyridine adsorption over SBA-15, and (c) pyridine adsorption over Zn-Tr (10)/SBA

A decrease by a factor of ~ 70% in the intensity of 3740 cm^{-1} band is noticeable in Fig. 4.5a at the saturation loading of zinc triflate. Much smaller (~25%) decrease in the intensity of this ν(OH) band was observed for adsorption of pyridine vapor in SBA-15, even after saturation coverage. These results are presented in Fig. 4.5b. Again, no shift was observed in the frequency of the ν(OH) bands. Interesting results were observed when the pyridine vapor was dosed over triflate loaded SBA-15 under the identical condition. The representative results on the relative intensity of 3740 cm^{-1} band for different loadings of pyridine in Zn-Tr (10)/SBA sample are shown in curve c of Fig. 4.5.

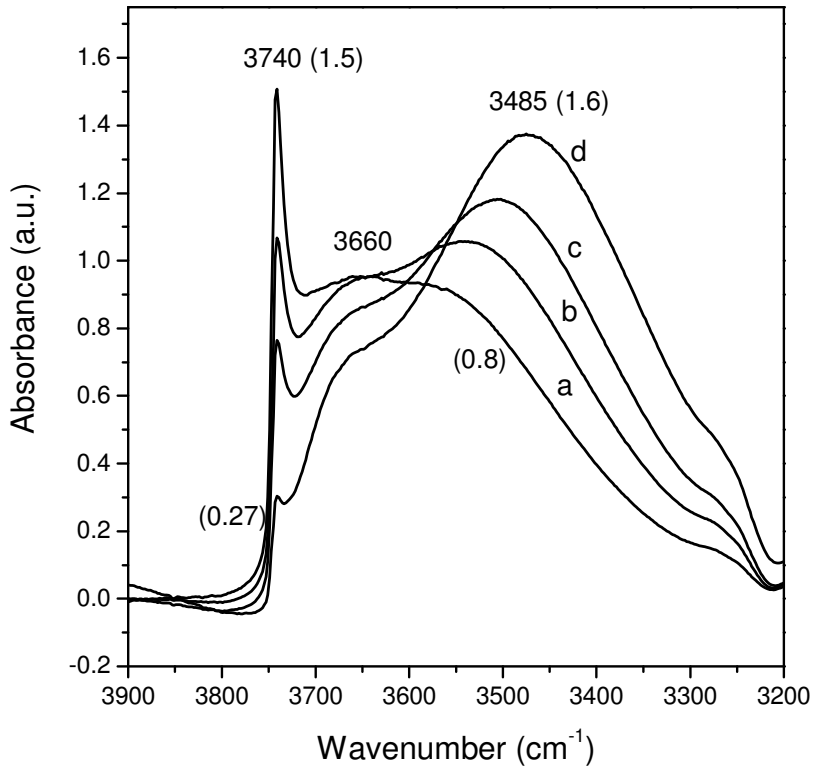

Fig. 4.6. The relative intensity of O–H stretching bands of Zn-Tr (10)/SBA on exposure to different amounts of pyridine. Amount of pyridine in micromol: Curve (a) nil, (b) 1, (c) 3 and (d) 7. The numbers given in the parentheses represent the relative absorbance values.

We observe in this case that even though the intensity of ν(OH) band has attained a saturation after the loading of triflate alone (cf. Fig. 4.5a), a considerably further decrease in the intensity took place as a result of subsequent pyridine loading (Fig. 4.5c). At the same time, the adsorption of pyridine over Zn-Tr/SBA gave rise to a strong band at ~3480 cm^{-1}, the intensity increasing systematically with the increase in the amount of adsorbed pyridine. A similar trend has been reported earlier for the adsorption of pyridine over MCM-41 [15]. Fig. 4.6 displays the IR spectra of Zn-Tr (10)/SBA sample for the dosing of 0- to 7 μmol of pyridine vapor. We observed here that the growth of 3480 cm^{-1} band matches well with the decrease in the intensity of 3740 cm^{-1} band. The intensity of

this new band at ~3480 cm^{-1} was however quite low in case of the pyridine adsorption over triflate-free SBA-15 and it was found to merge with the broad IR band in 3700-3600 cm^{-1} region. These results indicate that the perturbation of –OH groups in SBA-15 is more severe on occlusion of triflate molecules alone as compared to when pyridine vapor was adsorbed. The data presented in Fig. 4.5c further reveal that the mode of pyridine binding in the pores of SBA-15 is influenced considerably by the presence of the triflate molecules. These aspects are discussed later in more detail.

4.3.5.3. IR bands of adsorbed pyridine

Exposure of SBA-15 to pyridine vapor gave rise to two symmetrical broad IR bands at 1596 and 1446 cm^{-1}. Curve (c) in Fig. 4.7 exhibits a typical IR spectrum of calcined SBA-15 sample, recorded at 400 K after an exposure to 5 μmol pyridine. For comparison, curves (a) and (b) in Fig. 4.7 show the IR bands of vapor and liquid phase pyridine in this region. Whereas spectrum (a) was recorded by introducing pyridine vapor + nitrogen in the gas cell without placing a catalyst sample, spectrum (b) was plotted by placing a drop of pyridine in between the two KBr pellets.

The intensity of both the IR bands at 1596 and 1446 cm^{-1} in Fig. 4.7c followed a linear relationship with the increase in the amount of pyridine adsorbed and no saturation was observed. A plot showing typical loading dependent variation in the intensity of 1596 cm^{-1} band is given in curve (a) of Fig. 4.8.

The progressive growth of pyridine IR band in Fig. 4.8a is in contrast to the decrease observed in the intensity of 3740 cm^{-1} OH band, which showed a saturation effect even at 4 μmol pyridine loading (Fig. 4.5b). This indicates clearly that the decrease in the intensity of ν(OH) bands, as seen in Fig. 4.5b, may not arise due to any direct bonding of pyridine molecules to hydroxy groups.

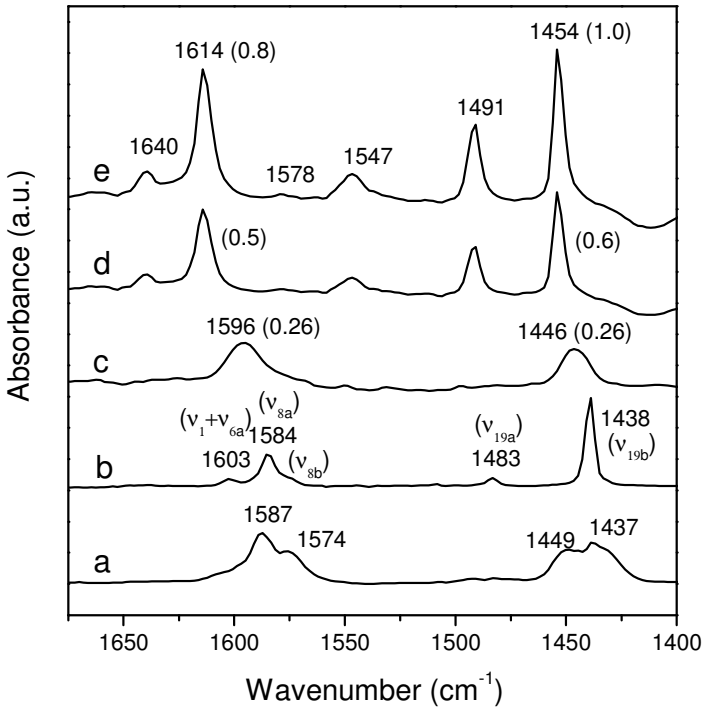

Fig. 4.7. Comparative IR Spectra of pyridine (5 μmol) adsorbed at 125 °C over (c) pure SBA-15, (d) Zn-Tr (5)/SBA and (e) Zn-Tr (10)/SBA catalysts. Curves (a) and (b) show the characteristic IR spectra of vapor and liquid states of pyridine, respectively.

Several new vibrational bands were detected when a triflate containing SBA-15 was exposed to pyridine vapor. Curve (d) in Fig. 4.7 presents the IR spectrum of Zn-Tr (5)/SBA sample, recorded on exposure to 5 μmol pyridine. We find in this figure three prominent vibrational bands at 1614, 1491 and 1454 cm^{-1}, in addition to some low intensity IR bands with the frequency maximum at 1640, 1578 and 1547 cm^{-1}. The intensity of these bands was found to increase considerably for the samples containing higher amount of zinc triflate.

For instance, curve (e) in Fig. 4.7 shows the IR spectrum of Zn-Tr (10)/SBA on exposure to 5 μmol pyridine. The numbers given in the parentheses in this figure represent the comparative absorbance of different IR bands.

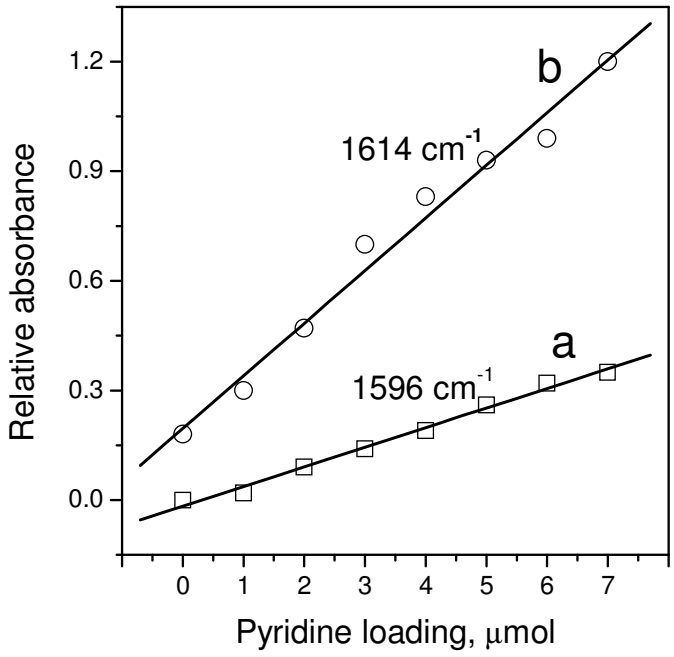

Fig. 4.8. Dose dependent variation in the intensity of IR signals of pyridine on adsorption over (a) pure SBA-15 (1596 cm^{-1} band) and (b) Zn-Tr (10)/SBA (1614 cm^{-1} band)

The intensity of these IR bands, however, reached saturation for the triflate loadings of 20 mol% and above. At the same time, in case of each of the zinc triflate containing samples, the intensity of the individual bands was found to increase progressively with the increasing amount of pyridine adsorbed. Curve (b) in Fig. 4.8 shows the typical variation in the intensity of 1614 cm^{-1} band as a function of pyridine loading in Zn-Tr (10)/ SBA.

Furthermore, the frequency and the intensity of various IR bands shown in Fig. 4.7e were found to vary considerably when different metal triflates were dispersed in SBA-15. Curves (b-e) in Fig. 4.9 exhibit IR spectra of SBA-15 samples, loaded with 30 mol% of different metal triflates and exposed uniformly to 5 μmol pyridine.

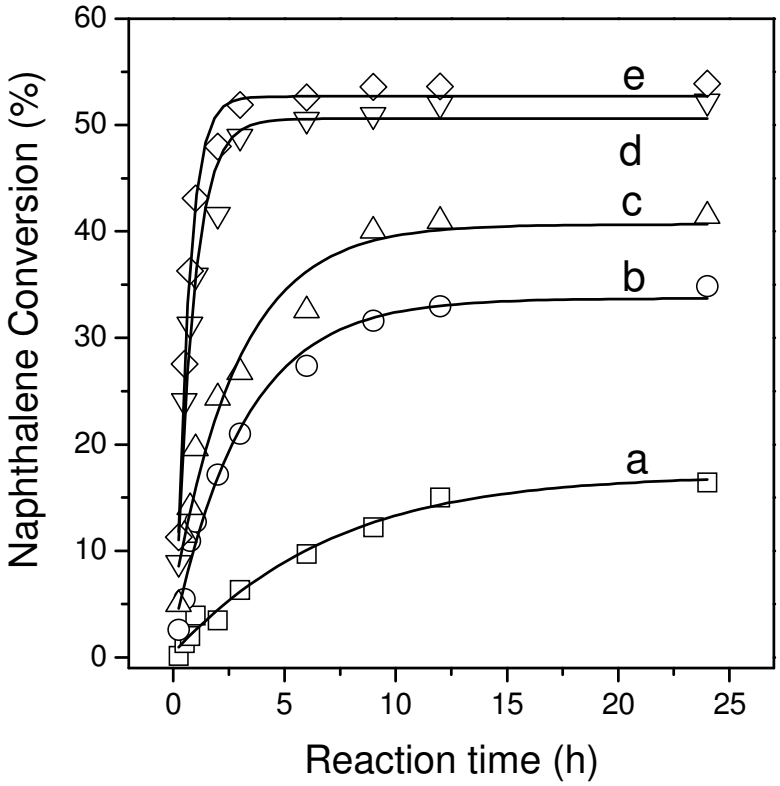

Fig. 4.9. Comparative FTIR spectra of pyridine (5 µmol) adsorbed at 125 ^{o}C over (a) pure SBA-15, (b) La-Tr (30)/SBA, (c) Ce-Tr (30)/SBA, (d) Y-Tr (30)/SBA, and (e) Zn-Tr (30)/SBA.

Curve (a) is again a comparative IR spectrum of pyridine adsorbed over pure SBA-15. It is important to notice that instead of a pair of weak bands at 1596 and 1446 cm^{-1} in Figs. 4.9 (b-d), a new pair of IR bands is observed at 1614 and 1454 cm^{-1} in the case of pyridine adsorption over zinc triflate containing SBA-15 (Fig. 4.9e). Moreover, the intensity of the 1546 cm^{-1} band is found to be much smaller in the IR spectrum in Fig. 4.9e as compared to that in Figs. 4.9(b-d). A weak and overlapping IR band at ~1618 cm^{-1} is also noticeable in Figs. 4.4 (b-d). The IR bands shown in Fig. 4.9 were found to be fairly stable when the samples exposed to pyridine vapor at 425 K were cooled to room temperature followed by 15 min pumping.

4.3.6. Catalytic reactions

4.3.6.1. Effect of triflate loading and reaction temperature

The host material SBA-15, with no triflate loading, showed no measurable catalytic activity for acylation of naphthalene under the reaction conditions of this study. In the case of triflate-functionalized SBA-15, the conversion of naphthalene was found to increase progressively with the increase in the triflate loading. Also, the best results were obtained by using the equi-molar mixture of the reactants, i.e. naphthalene + *p*-toluoyl chloride (*p*-TC). The conversion of naphthalene was found to decrease drastically for smaller amounts of *p*-TC taken for a reaction. In the representative experiments conducted at 140 ^{o}C over zinc triflate loaded SBA-15 and using an equi-molar mixture of naphthalene + *p*-toluoyl chloride (*p*-TC), the overall conversion of naphthalene was found to increase progressively from ~35 to 55 % for the increase in the triflate loading from 5 to 30 mol%. The 2-acyl naphthalene was the major reaction product (~92% yield), the minor product being 1-acyl naphthalene. However, similar product selectivity was obtained by using the catalyst samples containing different loadings of a particular triflate.

The increase in the reaction temperature gave rise to higher conversions and also in the increase in the rate of FC reaction of naphthalene with *p*-toluoyl chloride. Taking Zn-Trif (30)/SBA-15 as a model catalyst again, the effect of the rise in reaction temperature on the time-dependent conversion of naphthalene is depicted in Fig. 4.10. These results show that the equilibrium conversion of naphthalene increases from 12.2 to 53.6 wt% with the increase in reaction temperature from 80 to 160 °C. At the same time, the rate of the reaction also increased considerably with the increase in reaction temperature. Thus, while an equilibrium conversion was achieved in ~24 h at 80 °C (curve a), the reaction was complete in about 3 h time at the temperatures above 120 °C (curves d, e). However, the selectivity for 2-acyl naphthalene remained nearly unchanged with the increase in reaction temperature.

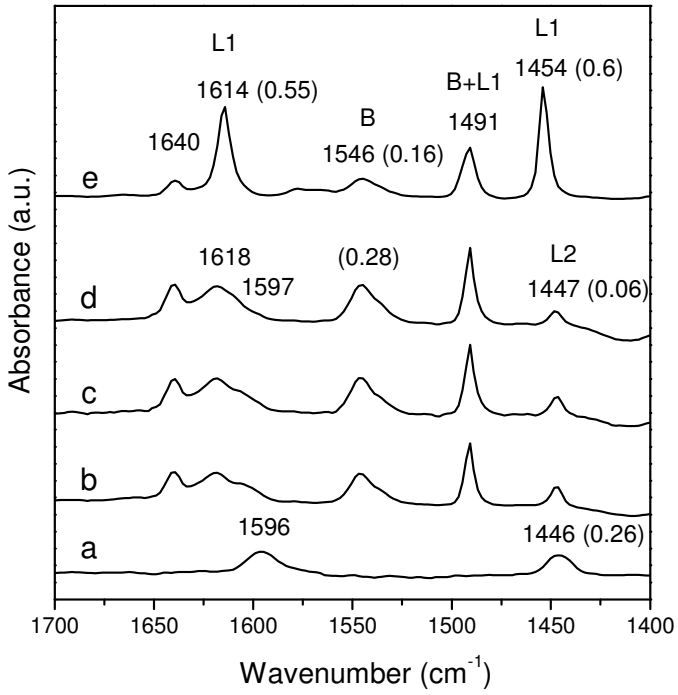

Fig. 4.10. Conversion of naphthalene over Zn-Tr (30)/SBA catalyst as a function of time and at different reaction temperatures: curve (a) 80, (b) 100, (c) 120, (d) 140 and (e) 160 °C. Reaction parameters: catalyst amount 0.1 g; Naphthalene = 10 mmol; *p*-TC = 10 mmol; Nitrobenzene = 5 ml.

4.3.6.2. Acylation of naphthalene over SBA-15 loaded with different metal triflates

The comparative catalytic activity of different metal triflates (Ce, La, Y and Zn, loaded at 30 mol% on SBA-15) for FC reaction of naphthalene with *p*-toluoyl chloride is shown in Fig. 4.11. The results reported in this figure are for the reaction conducted at 140 ^{o}C over a period of ca. 9 h, using the reactants in an equi-molar ratio. As mentioned above, the main reaction product was naphthalen-2-yl(p-tolyl)methanone. Also, the product distribution was almost independent of the catalyst used. As seen in Fig. 4.11, the Zn-Trif-SBA-15 catalyst showed much higher catalytic activity as compared to the catalysts containing rare earth triflates, even though the selectivity for 2-acyl naphthalene production was almost similar (94-98%). In order to demonstrate a relationship between

the activity and the acidic strength, the number of acid sites in different catalysts (TPD results) is plotted in curve d of Fig. 4.11. We may add that all the triflate based catalysts showed remarkable stability and reproducibility in catalytic activity when utilized for 5-6 consecutive test runs, the activity loss in the process being ca. 5%.

4.4. DISCUSSION

The results presented in Fig. 4.11 exhibit a direct relationship between the naphthalene conversion (curve a) and the density of the acid sites in a particular catalyst sample (curve d). Thus, almost 5- times higher conversion obtained by using Zn-Tr (30)/SBA, as compared to the rare earth triflate containing samples, is reflected in the considerably higher acidity of this catalyst (Table 4.1). On the other hand, almost similar activity of the three rare earth based catalysts is in consonance with the number of the acid sites present in these samples. The higher activity of zinc containing samples can be explained by visualizing the mode in which triflate molecules are bonded in the channels of the SBA host. The IR spectra in Fig. 4.4 and the corresponding assignments in Table 4.2 help us in establishing the binding states of a grafted triflate molecule. As is well known, the non-coordinated triflate ion (i.e. $CF_3SO_3^-$) has a point-symmetry C_{3v}, where the antisymmetric stretching mode, $\nu_{as}(SO_3)$, with E- symmetry is doubly degenerate while the A1 symmetric mode, $\nu_s(SO_3)$, is non-degenerate [16]. Both these modes are IR active. The coordination of triflate ion causes the lowering of the symmetry and hence in the splitting of the antisymmetric SO_3^- stretching mode into two components [17]. The extent of this splitting will depend upon the physical state of the molecules. The overlapping IR bands at 1270 and 1340 cm^{-1} are thus assigned to the antisymmetric SO_3 stretching, following the assignments reported in the previous studies [16-18]. Based on the studies conducted on ^{18}O–labeled triflates [18], the strong IR bands appearing at 1245 and 1180 cm^{-1} in Fig. 4.4c for pure zinc triflate are assigned to the symmetric and antisymmetric stretching modes of (CF_3) groups. Corresponding asymmetric deformation band appears at 576 cm^{-1}. No appreciable shift in these frequencies is observed when the zinc triflate molecules are grafted on to SBA -15 (Fig. 4.4a Table 4.2). No significant electronic interaction is therefore envisaged between the guest molecules and the surface

of the host silicate. At the same time the relative intensities of the IR bands due to (SO_3) and (CF_3) groups undergo considerable changes. Thus, the comparison of spectra (a) and (c) in Fig. 4.4 reveal a drastic decrease in the intensity of the IR bands, both symmetric and antisymmetric modes, related mainly to the CF_3 groups. These observations point to a significant perturbation of triflate molecules as a result of their occlusion in the channels of SBA-15. The nature of this perturbation becomes clear when we take onto account the changes occurring in the stretching vibrations of the hydroxyl groups. Fig. 4.5a shows that the intensity of the 3740 cm^{-1} band, arising due to the O–H stretching of the isolated silanols in SBA-15, decreases progressively with the increasing loading of the zinc triflate. No shift was, however, observed in the frequency of this band as a result of triflate loading (not shown). This behavior has been attributed earlier to the interaction of triflate molecules with surface OH groups and both the (SO_3) and (CF_3) groups are shown to participate individually in such interactions [19-22]. Various possible binding modes of triflate ion ($CF_3SO_3^-$) at the surface silanols, viz. monodentate, bidentate, tridentate and tetradentate, have also been postulated in an earlier publication [4]. We may, however, point out that an electronic interaction between the triflate ion with the surface sites of SBA-15 is likely to change the frequency of the bonded guest molecules, as has been discussed in our earlier publication [23]. Similarly, the ν(OH) frequency is expected to increase because of the increased electron density along the hydroxyl group. Therefore, the spectroscopy results of our study can not be ascribed to any electronic interaction between the triflate ions and the surface hydroxyl groups. On the other hand, the results reported here are akin to the findings of our previous studies on the occlusion of small molecules, such as methanol, benzene and cyclohexane, in the channels of micro- and mesoporous silicates [23, 24]. Based on the detailed discussion presented in these references, the removal of 3740 cm^{-1} band on triflate or pyridine loading can be attributed to the physical perturbation or the displacement of the –OH groups. This may facilitate a weak van der Waals type interaction between the two displaced hydroxyl groups, leading to the progressive removal of 3740 cm^{-1} band and the development of a new lower frequency band at ~3485 cm^{-1} (Fig. 4.6). This is shown graphically in Fig. 4.12. This mode of triflate occlusion in SBA-15 would thus enable a metal cation to serve as a

distinct Lewis acid site for the activation of a reactant molecule, as shown in Fig. 4.12. The reaction mechanism for the acylation of naphthalene can thus be expressed by the reaction steps given in Scheme 4.1. In this scheme, the first step consists of an interaction of toluoyl chloride with the metal triflate to form an acyl cation-zinc triflate activated complex. This transient complex may promote the formation of some highly active species, e.g. acylium ion. In the second step the acylium ion may react with the naphthalene, giving rise to the formation of 2-acyl naphthalene and eventual regeneration of the catalyst (scheme 4.1).

IR results in Figs. 4.7, 4.8 confirm that the acid density in a catalyst was directly related to the loading of a metal triflate. Moreover, the nature of the acid sites in a catalyst sample may depend considerably on the cation associated with a metal triflate, as seen clearly in Fig. 4.9. A pair of strong IR bands observed at 1614 and 1454 cm^{-1} in the case of pyridine adsorption over zinc triflate loaded SBA-15 (Fig. 4.9e) arises due to well reported 8a ν(C–C) and 19b ν(C–C) vibrations of pyridine adsorbed at the Lewis acid (designated as L1) sites [15, 25]. Another pair of bands observed at 1640 and 1546 cm^{-1} in this figure is known to arise due to the vibrations of pyridine molecules bound at bridge-bonded Brönsted (B) sites. The band appearing at 1491 cm^{-1} is attributed to the adsorption of pyridine at both the Lewis and Brönsted acid sites. In the case of SBA-15 samples containing the triflates of Y, La and Ce, instead of a pair of bands at 1614 and 1454 cm^{-1} we observe two low intensity bands at 1597 and 1447 cm^{-1} (Figs. 4.9, b-d), similar to the IR bands observed for pure SBA-15 (Fig. 4.9a). As discussed in our earlier paper in detail [25], these bands are attributable to weak Lewis acid sites (designated as L2), a characteristic feature of the siliceous mesoporous silicates having a weak acid character. The higher intensity of 1546 cm^{-1} band in curves b, c, and d of Fig. 4.9 indicates that the samples loaded with the triflates of La, Ce and Y exhibit much higher Brönsted acidity and at the same time a lower Lewis acidity, as compared to the zinc triflate containing sample. The ratio B/L (L1 or L2) follows a trend La (9.5) > Y (4.7) > Ce (3.0) > Zn (0.3), and this matches well with the catalytic activity results of Fig. 4.11.

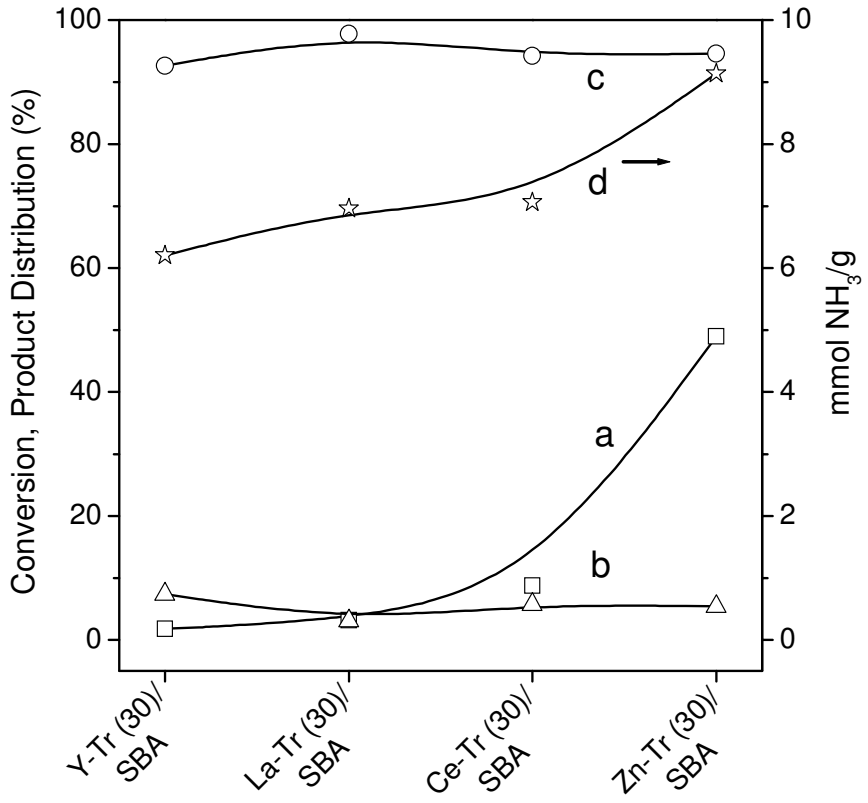

Fig. 4.11. Comparative catalytic activity and product selectivity for the naphthalene acylation reaction carried out using different metal triflate loaded (30 mol %) SBA-15 catalysts. Curve (a) conversion of naphthalene, (b) selectivity for 1-acyl naphthalene, (c) selectivity or 2-acyl naphthalene and (d) acid density of different catalysts
Reaction parameters: catalyst amount 0.1 g; naphthalene = 10 mmol; *p*-TC = 10 mmol; nitrobenzene = 5 ml; reaction temperature = 140 °C; reaction time = 9 h.

The important role played by the metal cation in an occluded triflate molecule becomes apparent when we compare the IR bands in spectra (c-e) in Fig. 4.7 with the corresponding spectra of pyridine in its vapor (curve a) and liquid (curve b) forms. In the case of pyridine adsorption over pure SBA-15 (Fig. 4.7c), the two observed bands are quite broad and at the same time they lack in the splitting of the bands, a characteristic feature of the IR spectrum of pyridine vapor (cf. Fig. 4.7a). Further, the full width at half

maximum (FWHM) of the IR bands seen in Fig. 4.7c is ~15 cm^{-1}, and this lies in between the FWHM values for IR bands of vapor (~28 cm^{-1}) and liquid (~ 4 cm^{-1}) phases of pyridine.

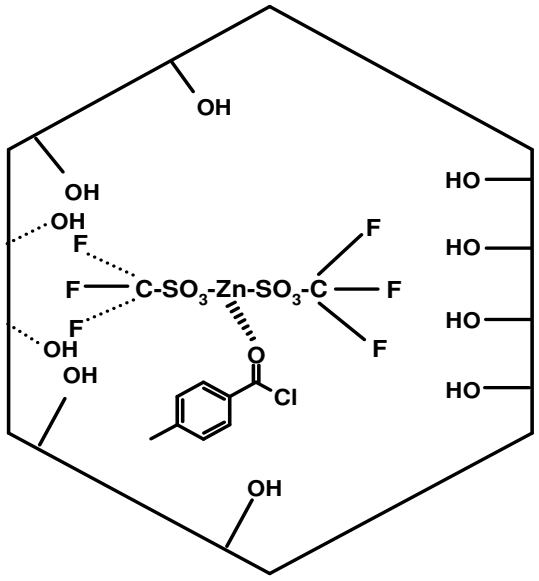

Fig. 4.12. Schematic presentation of the perturbation of −OH groups caused by the confinement of a metal triflate molecule in silicate channel, and the postulated binding mode of a reactant molecule.

This indicates that the pyridine molecules entrapped in SBA-15 may exist in a non-equilibrium state, in between the vapor and the liquid form. In this adsorbed state, the pyridine molecules are likely to retain their rotational motion without any strong bonding at the SBA sites. On the other hand, a considerable shift is observed in the frequency of ν8a and ν19b C–C bands for the adsorption of pyridine molecules in Zn-Tr/SBA samples (Fig. 4.7d, e). In addition, significant narrowing of the peaks (FWHM ~6 cm^{-1}) is noticeable in spectra (d) and (e) of Fig. 4.7, as compared to the IR bands of pyridine vapor (Fig. 4.7a). This represents an immobile state of pyridine molecules having no rotational motion. It can thus be concluded that the triflate metal cations may

participate in the direct binding of a guest molecule, a situation similar to that presented schematically in Fig. 4.12.

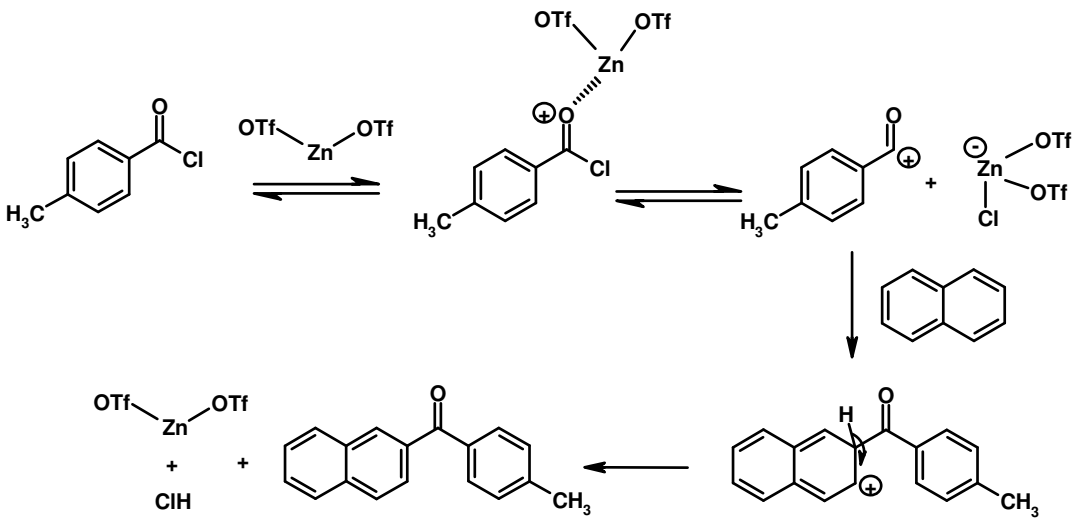

Scheme 4.1. Reaction steps in the zinc triflate - assisted activation of p-toluoyl chloride molecules giving rise to the acylation of naphthalene.

Further, the systematic increase in the intensity of pyridine bands as a function of increasing triflate loading in SBA-15 (Fig. 4.7, 4.8) and the dependence of Lewis acidity in the functionalized silicate samples on the nature of the occluded metal cation (Fig. 4.9) also serve as evidence for the direct participation of the triflate cation in binding of the pyridine molecules. Logically, other reactant molecules are likely to undergo similar binding at the cation sites, as depicted in Fig. 4.12. The binding of the pyridine molecules at triflate metal cations may eventually lead to further perturbation of the surface hydroxyl groups in host matrix, thus giving rise to some synergistic changes in the intensity of ν(OH) band, as shown in Fig. 4.5c. We surmise that the perturbed –OH groups may give rise to certain bridge bonded hydroxyl species with the participation of a triflate metal cation, and these species may be associated with a broad IR band observed at 3485 cm^{-1} in Fig. 4.6. These bridge bonded hydroxyl groups may in turn serve as new Brönsted acid sites, the presence of which is seen clearly in IR spectra in Figs. 4.7d, e.

The very small intensity of 3485 cm^{-1} band in case of pyridine adsorption over triflate-free SBA-15, as mentioned above, and the near absence of the Brönsted acid sites in Fig. 4.7c are in conformity with our ideas.

The distinctive acid character exhibited by zinc as compared to other metal triflates may find relationship with various factors, such as electronic configuration of the cation, coordination number and cationic radius. It is surmised that these factors may influence the overall configuration of the particular triflate molecules entrapped in the silicate pores, thus deciding the acidic character of a functionalized silicate. Further studies are now underway to further understand these important observations

4.5. CONCLUSIONS

The zinc triflate molecules entrapped in the pores of mesoporous SBA-15 exhibit considerably high acid strength and also a high catalytic activity for acylation of naphthalene, as compared to the samples containing triflates of Y, La or Ce. The results of our IR studies reveal that while large triflate groups may assist in the geometric confinement within the pores of the mesoporous SBA-15, the metal cations are basically responsible for the direct binding of the reactant molecules and hence for the catalytic properties. We surmise that the confinement of a large molecule such as metal triflate may cause significant physical perturbation to the surface hydroxyl groups of the host matrix and this in turn may give rise to the formation of certain Brönsted type surface acid sites.

4.6. REFERNECES

[1] F. Sainte, B. Serckx-Poncin, A.-M. Hesbain-Frisque, L. Ghosez, *J. Am. Chem. Soc.,* 104, **1982**, 1428.

[2] G.A. Olah, O. Farooq, S. Morteza, F. Farmina, J.A. Olah, *J. Am. Chem. Soc.,* 110, **1998**, 2560.

[3] T. Tsuchimoto, K. Tobita, T. Hiyama, S. Fukuzawa, *Synlett*, **1996**, 557.

[4] M. Chidambaram, D. Curulla-Ferre, A.P. Singh and B.G. Anderson, *J. Catal.,* 220, **2003**, 442.

[5] N.E. Drysdale, N. Herron, WO Patent 9502625, **1994**.

[6] K. Wilson, A. Renson, J.H. Clark, *Catal. Lett.,* 61, **1999**, 51.

[7] S. Kobayashi, S. Nagayama, *J. Am. Chem. Soc.,* 120, **1998**, 2985.

[8] F. Schager, W. Bonrath, *Appl. Catal. A: Gen.,* 202, **2000**, 117.

[9] M.G. Clerici, C. Perego, A. De Angelis, L. Montanari, European Patent 638363, **1995**.

[10] A. Sakthivel, S.-J. Huang, W.-H. Chen, W.-H. Chen, Z.-H. Lan, K.-H. Chen, T.-W. Kim, R. Ryoo, A.S.T. Chiang, S.-B. Liu, *Chem. Mater.*, 16, **2004**, 3168.

[11] Z. Yang, Y. Xia, R. Mokaya, *Adv. Mater.,* 16, **2004**, 727.

[12] N.M. Gupta in "Catalysis: Principles and Applications", B. Viswanathan, S. Sivasanker, A.V. Ramaswamy (Eds.), Narosa, New Delhi, **2002**, pp. 127-144.

[13] C.N. Trung, J.C. Bryan, D.A. Palmer, *Structural Chemistry,* 15, **2004**, 89.

[14] K. Wilson, J.H. Clark, *Chem. Commun.,* **1998**, 2135.

[15] A. Jentys, N.H. Pham, H. Vinek, *J. Chem. Soc. Faraday Trans.,* 92 (17), **1996**, 3287.

[16] H. Burger, H. Burezyk, A. Blaschette, *Monatshefte fur cheie,* 101, **1970**, 102.

[17] A. Wendsjo, J. Lindgren, J.O.Thomas, G.C. Farrington, *Solid State ionics,* 53-56, **1992**, 1077.

[18] D.H. Johnston, D.F. Shriver, *Inorg. Chem.,* 32, **1993**, 1045.

[19] S.M. Coman, M. Florea, V.I. Parvulescu, V. David, A. Medvedovici, D.D. Vos, P.A. Jacobs, G. Poncelel, P. Grange, *J. Catal.,* 249, **2007**, 359.

[20] C. Paze, G.T. Palomino, A. Zecchina, *Catal. lett.,* 60, **1999**, 139.

[21] A. de Angelis, C. Flego, P. Ingallina, L. Montanari, M.G. Clerici, C. Carati, C. Perego, *Catal. Today,* 65, **2001**, 363.

[22] O. Mouhtady, H.G. Iloughmane, N. Rogues, C.L. Roux, *Tetrahedron Lett.,* 44, **2003**, 6379.

[23] M.D. Kadgaonkar, M.W. Kasture, V.B. Kartha, R. Kumar, N.M. Gupta, *J. Phys.Chem. C,* 111, **2007**, 9927.

[24] A. Sahasrabudhe, S. Mitra, A. K. Tripathi, R. Mukhopadhyay, N.M. Gupta, *Phys.Chem. Chem. Phys.,* 5, **2003**, 3066.

[25] P. Kalita, N. M. Gupta, R. Kumar, *J. Catal.,* 245, **2007**, 338.

CHAPTER-5

BENZYLSULFONIC ACID FUNCTIONALIZED Zr-TMS CATALYSTS (Zr-TMS-BSA)

5.1. INTRODUCTION

The Mobil researchers opened a new area in the synthesis of mesoporous materials through the discovery of M41S family of silicate mesoporous molecular sieves, particularly, MCM-41 by liquid-crystal templating mechanism [1]. Because of thermal stability, high surface area (around 1000 m^2/g) and narrow pore-size distribution, these materials have invited a great deal of attention for the synthesis of wide range of bulky organic molecules. However, the MCM-41 type materials showed weak acid sites [2]. The synthesis of transition metal oxide based mesoporous materials such as Titanium [3, 4], zirconium [5-7], niobium [8], tantalum [9], aluminum [10], hafnium [11], tin [12] and manganese [13] have been synthesized using ionic or neutral templates as structure directing agents, although most of them were comprise of mainly non-porous framework walls, which would limit their thermal and hydrothermal stability and greatly negotiation their usefulness in catalytic application. Among these materials, zirconia [14] and alumina [10], only maintain the mesoporous arrangement upon the removal of template from the material by calcination or solvent extraction methods. Transition metal oxides are widely used as industrial catalysts and as catalysts supports. Unfortunately they usually have poorly defined pore structures. Further, among the mesoporous materials, zirconia is of particular interest due to the high thermal stability and ease of synthesis [15, 16]. In the recent years SO_4^{2-}/ZrO_2 has attracted attention as it catalyzes various industrially important reactions such as: isomerization; condensation; Friedel-Crafts acylation reactions; etc [17]. However, its non-uniform pore size, low porosity, and small surface area limit its potential application for catalyzing reactions of bulky molecules. Because of the various oxidation states of zirconia, in addition to the high surface area, moderate acidity and the attractive porous nature have advantages over aluminosilicate materials for use in electromagnetic, photoelectronics and as a good support in catalysis [18].

The bifunctional nature of mesoporous zirconia has an unusual interest in the field of acidic catalysis. However, many attempts have been made to increase the acidity of these materials by using dopants or functional groups. Doping phosphates [19] or sulfates [20-22] result not only in an increase in the acidity but also a relative increase in thermal

stability. These attempts result the preparation of mesoporous sulfated zirconia having partially tetragonal wall structure and narrow distribution of pore sizes by controlled hydrolysis of zirconium propoxide [23]. Moreover, the addition of the sulfate ion stabilizes the mesoporous morphology and delays crystallization. MCM-41 analogous materials have been synthesized together with zirconium oxide-sulfate and zirconium oxo phosphate [6] and a special post synthetic treatment has been developed in the later case. There has been considerable interest in the development of heterogeneous solid acid catalysts to avoid the use of traditional homogeneous acid catalytic systems (H_2SO_4, HF, $AlCl_3$, BF_3, etc.) which present serious drawbacks including hazards in handling, corrosiveness, production of toxic waste, and difficulties in separation. In this context, as an alternative, the covalent attachment of alkylsulfonic acid groups to the surface of molecular sieves has been proposed by several authors and successfully tested in several acid catalyzed reactions, including esterification [24-28] and condensations [28-31]. Sulphonic acid functionalized MCM-41 [27], SBA-2 [26] and SBA-15 [26, 31] were prepared through a thiol oxidation route. As a result, one-pot sol-gel route has been employed to achieve high levels of (3-mercaptopropyl) trimethoxysilane (3-MPTS) incorporation into mesoporous silica with >90 % efficiency and characterized by XPS and Raman spectroscopy [30].

In resent years, further, ordered mesoporous organosilica hybrid material is extended to the surfactant-mediated synthesis of benzene-silica hybrid material, phenylene-biphenylene materials, and benzene-silica hybrids with molecular-scale periodicity, large-pore phenylene-bridged mesoporous organosilica using triblock copolymer surfactant [32-35]. Among the functionalized MCM-41 type materials, phenyl sulphonic acid functionalized MCM-41 exhibits better performance than the alkyl sulphonic acid functionalized MCM-41 in the esterification reactions. Using both catalysts, the esterification of glycerol with lauric acid and oleic acid were studied by Sastre and co-workers [24, 27]. Sohn et al. [36] reported a modified silica catalyst with derivatives of benzene-sulfonate groups and studied the catalytic activity in dehydration reactions. In order to establish novel environmentally benign materials, in the present chapter, we report the functionalization of benzyl group loaded mesoporous zirconium

hydroxide with various amounts of chlorosulphonic acid without damaging the mesostructure of Zr-TMS. The functionalized materials were characterized by various physico-chemical techniques. The objective of the study is to replace the conventional, homogenous and Lewis acid catalyst by the shape selective and active Zr-TMS-BSA catalyst, to enhance the conversion of resorcinol, 2-methoxy phenol and 1-naphthal and product selectivity of 7-hydroxy-4-methylcoumarin, 7-methoxy-4-methylcoumarin and 7, 8-benzo-4-methylcoumarin and consequently to minimize the formation of consecutive products which is obtained using other homogeneous catalysts. Our fresh and recycle reaction studied proved that this catalyst can be used as an alternative.

5.2. EXPERIMENTAL

5.2.1. Materials

The syntheses of Zr-TMS-BSA catalysts were carried out using zirconium (IV) butoxide (80 wt% solution in 1-butanol, Aldrich, USA), a 25 wt% aqueous solution of tetramethyl ammonium hydroxide (TMAOH, Loba Chemie, India), a 25 wt% aqueous solution of N-cetyl-N, N, N trimethyl ammonium bromide (CTMABr, Loba Chemie, India), acetyl acetone (acac, 98%, Merck, India), benzyl alcohol (99%, Lancaster, UK) ethoxytrimethylsilane (ETMS, 98%, Sigma-Aldrich, USA) and chlorosulphonic acid (CSA, 98%, Spectrochem, India).

5.2.2. Synthesis of Zr-TMS material

The Zr-TMS was synthesized by adopting the following molar composition,

0.1 $Zr(OC_4H_9)_4$:1.4 BuOH:0.025 CTMABr:0.02 TMAOH:4 H_2O:0.05 Acac:0.5 EtOH

Mesoporous zirconium hydroxide (Zr-TMS) was synthesized by sol-gel route using zirconium (IV) butoxide as the zirconia source and N-cetyl-N, N, N-trimethyl ammonium bromide (CTMABr) as surfactant at a pH of 11.5, which was maintained by tetramethyl ammonium hydroxide (TMAOH) solution. Acetyl acetone (Acac) and ethanol controlled the rate of hydrolysis of zirconium butoxide in water. In a mixture of

water (4 mol) and TMAOH (0.03 mol), CTMABr (0.025 mol) was dissolved and stirred for 1 h. Then a mixture of zirconium butoxide (0.1 mol), acetyl acetone (0.05 mol) and ethanol (0.5 mol) were added to the template solution slowly and allowed to stir for 3 h. Further, the mixture was refluxed under stirring for 48 h at 90 °C. The resulting solid was filtered, washed with acetone and dried for 10 h at 100 °C (Equation 1 of Scheme 5.1).

5.2.3. Surfactant removal

The solvent extraction method was employed to remove the template from the pores of the mesostructure without destroying the structure of the molecular sieves using ethanol and HCl mixture. The efficiency of the process was confirmed by elemental analysis and powder x-ray diffraction studies. 1 g as-synthesized Zr-TMS was taken and refluxed with a mixture of 100 g of distilled ethanol and 1 g of conc. HCl (36 wt.%) for 6 h, 8 h and 10 h at 80 °C. Fresh samples were used for each extraction. The extracted samples were washed several times with pure distilled ethanol and acetone. The resulting solid was dried at 100 °C for 10 h.

5.2.4. Synthesis of Zr-TMS-BSA catalysts

In the first step, the functionalization of benzyl alcohol (0.1 mol) over Zr-TMS (1g) was carried out by etherification reaction using cyclohexane (0.35 mol) as solvent at 80 °C for 10 h (Step 2 of Scheme 5.1). The sample was filtered and washed with cyclohexane, benzene and finally with acetone and dried for 6 h at 50 °C. To protect the unloaded hydroxyl groups, after modification with benzyl alcohol, desired amount of Zr-TMS-BS was degassed at 80 °C for 2 h and dry toluene was added. Then an excess of ethoxytrimethylsilane was added and the suspension was refluxed at 70 °C under nitrogen atmosphere for 12 h (Step 3 of Scheme 5.1). The solid was filtered and soxhlet extraction was done with dichloromethane for 12 h and dried at 50 °C for 5 h. Further, sulphonation of the resulting material, Zr-TMS-BS was done with the appropriate amount of chlorosulphonic acid (Spectrochem, India) using chloroform (0.12 mol) as solvent at 70 °C for 3 h (Step 4 of Scheme 5.1).

The chlorosulphonic acid was added slowly by a syringe to the mixture of Zr-TMS-BS and chloroform.

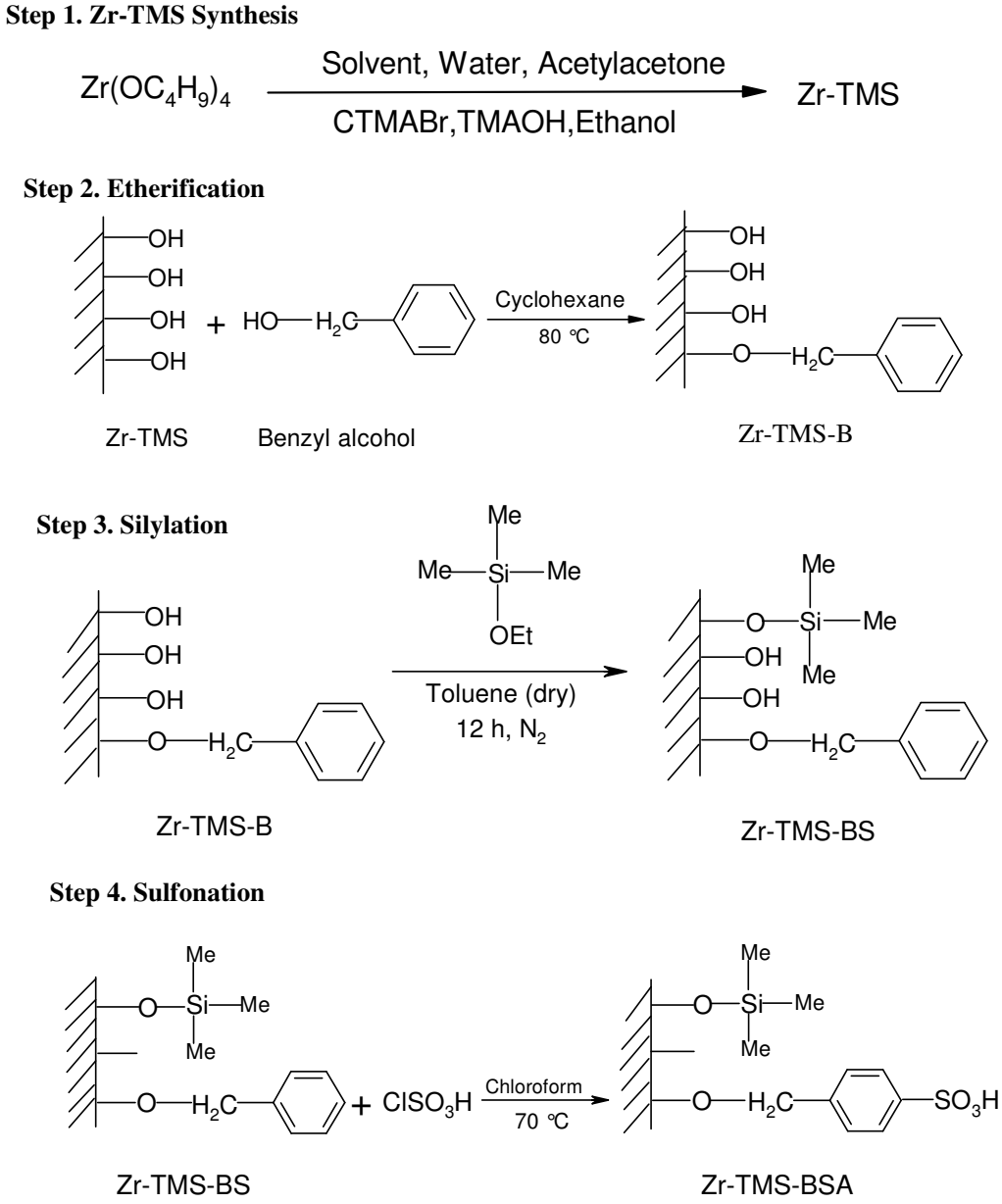

Scheme 5.1. Synthesis of benzylsulfonic acid functionalized Zr-TMS catalysts: 1. Synthesis of Zr-TMS; 2. Etherification of Zr-TMS (Zr-TMS-B); 3. Silylation of Zr-TMS-B (Zr-TMS-BS); 4. Sulfonation of Zr-TMS-BS (Zr-TMS-BSA)

Thus the material obtained was washed with chloroform and soxhlet extraction was done with a mixture of 1:1 diethyl ether and dichloromethane and dried at 50 °C for 6 h. Benzyl alcohol, ethoxytrimethylsilane and sulphonic acid functionalized Zr-TMS are designated as, Zr-TMS-B, Zr-TMS-BS and Zr-TMS-BSA, respectively.

5.2.5. Catalyst characterization

The synthesized materials were mainly characterized by powder X-ray diffraction (XRD) for phase purity and crystallinity, N_2 adsorption-desorption techniques for specific surface area, total pore volume and average pore diameter, Fourier transform infrared (FTIR) spectroscopy for functional group confirmation,
elemental analysis for C and S to measure the triflic acid loading in the material, solid state ^{13}C CP/MAS (cross polarisation/magic angle spinning), temperature programmed desorption (TPD) of NH_3 measurement for total acidity, scanning electron microscopy (SEM) for the particle size and morphology, transmission electron microscopy (TEM) to view the crystalline structure and thermo gravimetric-differential thermal analysis (TG-DTA and DTG) to study the decomposition and thermal stability of the catalysts.

The powder X-ray diffraction patterns of synthesized Zr-TMS, and Zr-TMS-BSA were recorded on a Rigaku Miniflex instrument using Cu K_α radiation (30 kV, 15 mA), λ=1.5404 Å between 1.5 to 60° (2θ) with a scan rate of 4°/min. The BET surface area, total pore volume, and average pore diameter were measured by N_2 adsorption-desorption method by NOVA 1200 (Quantachrome) at –196 °C. For this particular measurement, the samples were activated at 180 °C for 3 h under vacuum and then the adsorption-desorption was conducted by passing nitrogen onto the sample, which was kept under liquid nitrogen. The FT-IR spectra were obtained in a range of 400 to 4000 cm^{-1} on a Shimadzu FTIR 8201 PC using a Diffuse Reflectance scanning disc technique. Elemental analysis for C and S were done by EA1108 Elemental Analyzer (Carlo Erba Instruments).

^{13}C CP/MAS solid-state NMR studies were carried out on a Bruker DRX-500 NMR spectrometer. The resonance frequency was 125.757 MHz. The finely powdered sample Zr-TMS-BSA-10 was placed in 4.0 mm zirconia rotors and spun at 810 kHz. A relaxation delay of 4 sec was used for CP/MAS spectrum. The chemical shift was

referred to an external adamantane CH_2 peak reference taken as 28.7 ppm with respect to TMS.

Temperature programmed desorption (TPD) were carried out to determine the total acidity and strength of acid sites on the catalysts using ammonia as an adsorbate [38]. In a typical run, 1.0 g of activated sample was placed in a silica tubular reactor and heated at 200 °C under nitrogen flow of 50 ml/min for 6 h. The reactor was then cooled at 30 °C and adsorption conducted at that temperature by exposing the sample to ammonia (10 ml /min) for 30 min. Physically adsorbed ammonia was removed by purging the sample with a nitrogen stream flowing at 50 ml/min for 15 h at 30 °C. The acid strength distribution was obtained by raising the catalyst temperature (10 K/min) from 30 to 300 °C in a number of steps with the flow of nitrogen (50 ml/min). The NH_3 evolved was trapped in the HCl solution and titrated with a standard NaOH solution.

The SEM micrographs of Zr-TMS and Zr-TMS-BSA-10 materials were taken by JEOL-JSM-5200 scanning microscopy. TEM was performed on a JEOL JEM-1200EX instrument with 100 kV of acceleration voltage to probe the mesoporosity of the materials. The TG-DTA and DTG analysis of the Zr-TMS and Zr-TMS-BSA-10 catalysts were carried out with Mettler Toledo 851equipment using an alumina pan under a nitrogen (80 ml/min) atmosphere from ambient to 1000 °C with the increasing rate of 20 °C/min.

5.2.6. Catalytic activity

The catalytic activity of the synthesized materials was examined in the Pechmann condensation of aromatic alcohols. High purity resorcinol, 3-methoxyphenol, 1-naphthol and ethyl acetoacetate were used without further purification. The catalyst was activated at 100 °C for at least 4 h prior to experiments, so as to maintain the dry conditions.

The solvent free liquid phase catalytic condensation of aromatic alcohols were performed in a 25 ml round bottom flask separately fitted with a condenser, N_2 gas supply tube and a septum. The temperature of the reaction vessel was maintained using an oil bath. In a typical run, a mixture of aromatic alcohol (resorcinol, 3-methoxyphenol,

1-naphthol) (0.01 mol), ethyl acetoacetate (0.01 mol) and activated catalyst (0.1 g), were magnetically stirred and heated to attain the reaction temperature (150 °C). The product samples were withdrawn after 20 h of reaction time and analyzed on a gas-chromatograph (Agilent 6890N) equipped with a flame ionization detector and a capillary column (5µm thick cross-linked methyl silicone gum, 0.2 mm · 50 m long). The product sample was also identified by GCMS (Shimadzu 2000 A) analysis. Further, catalyst recycle study (fresh and three recycles) were also performed in all the reactions to prove the catalyst stability. The main products, 7-hydroxy-4-methylcoumarin, 7-methoxy-4-methylcoumarin and 7, 8-benzo-4-methylcoumarin is separated by column chromatography and confirmed by ^{1}H and ^{13}C NMR analysis. The elemental analysis and melting points of all the three products have also been measured for main products. Conversions of aromatic alcohols are defined as the weight percentage of aromatic alcohols consumed. The rates of the reactions (turn over frequency, TOF, h^{-1}) of aromatic alcohols were calculated as the moles of aromatic alcohols converted per mol of sulfur per hour. The product selectivity is expressed as the amount of a particular product divided by the amount of total products and multiplied by 100.

5.3. RESULTS AND DISCUSSION

5.3.1. Synthesis of catalysts

In order to immobilize the catalytically active species on a heterogeneous solid surface, an organic linker group is needed. Organic functionalization of the internal surfaces of any mesoporous materials can be achieved, either by covalently grafting of various organic species onto the surface or by incorporation of functionalities during the synthesis. Zr-TMS material has been synthesized by the procedure given in experimental part and obtained dry material before functionalization. For functionalization of BSA over Zr-TMS, two different methods were adopted and based on our preliminary instrumental techniques; the procedure given in experimental part was found suitable for the preparation of proposed Zr-TMS-BSA catalysts.

Five samples of BSA functionalized Zr-TMS (denoted as Zr-TMS-BSA-5, -10, -15, -20, and -25 wt %) were prepared and their compositions are listed in Table 5.1 and the generalized synthesis scheme of Zr-TMS-BSA is given in Scheme 5.1. Zr-TMS material (Equation 1 of Scheme 5.1.) was treated with benzyl alcohol to get Zr-TMS-BS material having the Equation II of Scheme 5.1. Further, Zr-TMS-B was treated with ethoxytrimethylsilane to get Zr-TMS-BS having the Equation III of Scheme 5.1 and sulfonation was done by chlorosulfonic acid to get benzylsulfonic acid functionalized Zr-TMS catalyst having the Equation IV of Scheme 5.1. Five different loading of BSA, such as 5, 10, 20, and 25 wt % over Zr-TMS was done and designated as Zr-TMS-BSA-5, Zr-TMS-BSA-10, Zr-TMS-BSA-15, Zr-TMS-BSA-20, and Zr-TMS-BSA-25, respectively; where as the effective loading is tabulated in Table 5.1, based on the sulfur concentration by elemental analysis of sulfur.

Table 5.1. Physico-chemical properties of synthesized Zr-TMS, Zr-TMS-BS, and Zr-TMS-BSA catalysts and sulfated zirconia.

Catalyst	Elemental Analysis (Output) [a] (Wt %)		Loading of sulphonic acid (Wt %)		BET surface area (m^2g^{-1})[b]	NH_3 desorbed (mmol/g)				NH_3 Chemisorbed at 30 °C (mmol/g)[c]
	C	S	input	output		30-70°C	70-110°C	110-150°C	150-200°C	
Zr-TMS[d]	--	--	--	--	370	0.06	0.15	0.19	0.10	0.50
Zr-TMS-BS	--	--	--	--	308	--	--	--	--	--
Zr-TMS-BSA-5[e]	2.9	2.0	5	4.7	229	0.11	0.26	0.31	0.04	0.72
Zr-TMS-BSA-10[f]	1.6	2.5	10	9.1	198	0.23	0.38	0.41	0.17	1.19
Zr-TMS-BSA-15	1.1	2.8	15	10.3	179	0.22	0.39	0.43	0.18	1.22
Zr-TMS-BSA-20	0.9	3.2	20	11.6	158	0.25	0.40	0.46	0.20	1.31
Zr-TMS-BSA-25	0.7	3.3	25	12.0	98	0.25	0.41	0.48	0.20	1.34
SO_4^{2-}/ZrO_2[g]	--	2.6	10	7.9	101	--	--	--	--	1.45

[a]Measured by EA 1108 CHN/S Elemental analyzer to measure the acid loading.
[b]Measured by N_2 adsorption-desorption at –196 °C.
[c]Total acid sites determined in the solid catalyst by NH_3 adsorption-desorption from 30 to 200 °C
[d]Total pore volume is 0.31 cm^3g^{-1}, average pore diameter is 30.9 Å for Zr-TMS.
[e]Numbers denote wt% (input) of sulphonic acid loading over Zr-TMS-BS.
[f]Total pore volume is 0.18 cm^3g^{-1}, average pore diameter is 18.2 Å for Zr-TMS-BSA-10.
[g]Total pore volume is 0.09 cm^3g^{-1}, average pore diameter is 9 Å for SO_4^{2-}/ZrO_2.

5.3.2. Template extraction optimization by XRD

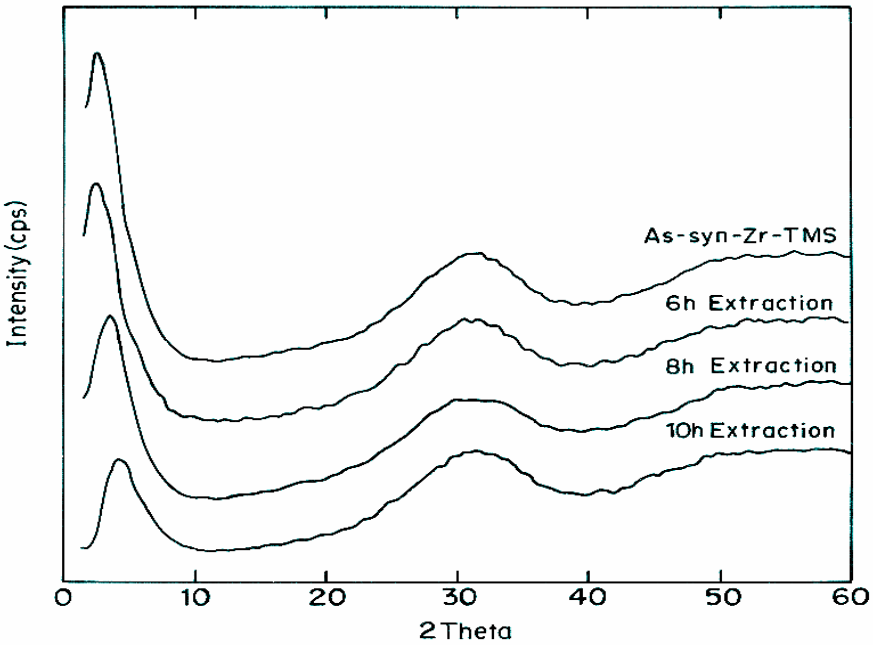

Figure 5.1. Powder X-ray diffraction pattern of Zr-TMS with respect to template extraction time As-syn-Zr-TMS, 6 h, 8 h, and 10 h.

Figure 5.1 shows the powder XRD pattern of as-synthesized Zr-TMS and different time of extraction (such as 6 h, 8 h and 10 h) to remove the template from the synthesized Zr-TMS for establishing the time of extraction without destroying the mesoporous structure. All spectra show a sharp peak at low 2θ (2°- 4°) range, which is characteristic of ordered porous structure of Zr-TMS [38-42], and two broad peaks at 30° (broad) and 50° (small), which are attributed to the amorphous nature of $Zr(OH)_4$ which can also be detected in the siliceous MCM-41 material [43]. Further, when it is calcined above 600 °C it may give sharp and intense peaks characteristic of tetragonal, monoclinic and cubic phases of ZrO_2, which are not shown here. The intensity of mesophase decreases with the increase in time of extraction. The decrease in intensity of Zr-TMS with the increase in time of extraction is attributed to the partial structure damage of Zr-TMS. The surface area of these samples, 6 h, 8 h and 10 h (Figure 5.1) was found to be

341, 370 and 364 m^2/g, respectively. The surface area measurement revealed that after 6 h of extraction, the sample was partially extracted. Though the 8 h and 10 h samples did not show much difference in surface area but the XRD intensity of 10 h sample decreased a lot (Figure 5.1) indicating that there is structure damage to some extent and hence it is clear that 8 h extraction is the optimum time for removal of template from the synthesized material.

5.3.3. Influence of time of $ClSO_3H$ loading by XRD

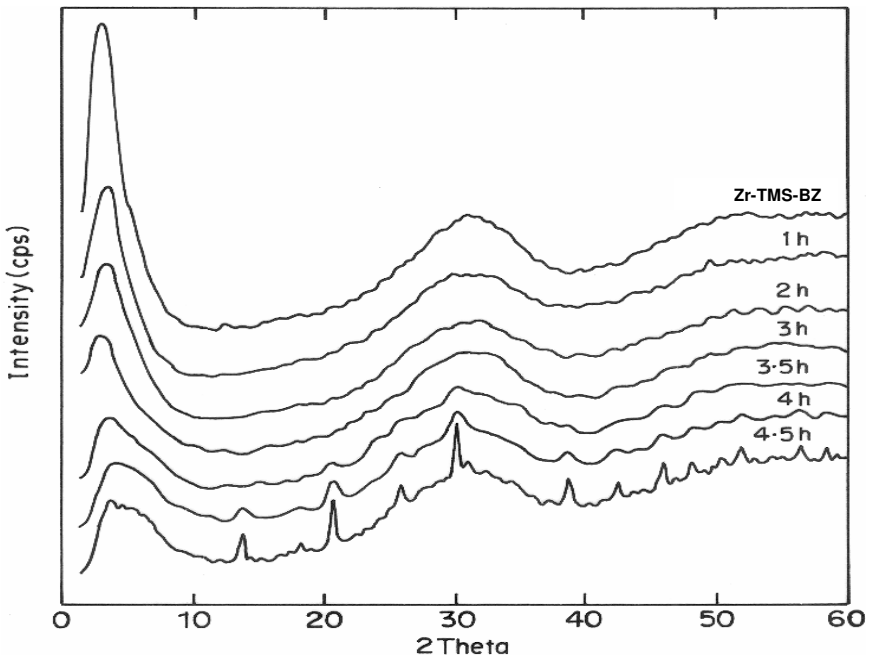

Figure 5.2. Powder XRD pattern of standardization of $ClSO_3H$ functionalization over Zr-TMS-BS with respect to time.

The influence of time of chlorosulphonic acid functionalization on the mesoporous nature of Zr-TMS-BSA catalyst is shown in Figure 5.2 (Zr-TMS-BS, 1 h, 2 h, 3 h, 3.5 h, 4 h and 4.5 h). 10 wt% chlorosulphonic acid was used over Zr-TMS-BS to optimize the time without the structure collapse. The intensity of the mesophase in all the samples at low 2θ range (characteristic for mesoporous material) decreases with the

increase in functionalization time, which showed that there was slow decay of mesoporous nature. Further, XRD pattern shows that after 3 h of reflux time extra peaks were noticed, which may be the prominent phases of zirconia, such as tetragonal, monoclinic and cubic. The intensity of these peaks increased with the increase in reflux time (Figure 5.2, 4 and 4.5 h), which revealed that there was fast crystallization and consequently severe structure damage of the material. The surface area of Zr-TMS-BSA, 1 h, 2 h, 3 h, 3.5 h, 4 h and 4.5 h samples were found to be 308, 287, 229, 215, 201, 181 and 172 m^2/g, respectively. The decrease in surface area may be attributed to the loading of $–SO_3H$ group over Zr-TMS-BS and a decrease in meso-phase of Zr-TMS-BSA may be due to the formation of HCl as by product during functionalization, which destroys the mesoporous structure to some extent. It is clear from these data that time of functionalization cannot be extended beyond 3 h at our experimental condition to get optimum concentration of sulphonic acid over Zr-TMS-BS.

5.3.4. Influence of concentration of sulphonic acid by XRD

Figure 5.3 illustrates Zr-TMS, Zr-TMS-BS and the influence of $ClSO_3H$ concentration over Zr-TMS-BS (Zr-TMS-BSA-5, -10, -15, -20 and –25). The functionalization of Zr-TMS-BS by $ClSO_3H$ was done by varying the concentration of $ClSO_3H$ and keeping the functionalization time at 3 h. Various loading of sulphonic acid over Zr-TMS-BS such as 5, 10, 15, 20 and 25 wt% (input) was done and found to be 4.7, 9.1, 10.3, 11.6 and 12 wt% (output) of SO_3H over Zr-TMS-BS, respectively (see Table 5.1, elemental analysis). The crystallinity of the sulphonic acid containing Zr-TMS-BS materials decreased as the chlorosulphonic acid loading increased.

Moreover, once the concentration of chlorosulphonic acid was increased >15 wt% (see Figure 5.3) the mesophase started to vanish and it was observed that at higher loading (25 wt%, Zr-TMS-BSA-25) the structure was completely destroyed. The surface areas of Zr-TMS, Zr-TMS-BS, Zr-TMS-BSA-5, Zr-TMS-BSA-10, Zr-TMS-BSA-15, Zr-TMS-BSA-20, and Zr-TMS-BSA-25 were found to be 370, 308, 229, 198, 179, 158 and 98 m^2/g, respectively (Table 5.1). A decrease in surface area of Zr-TMS-BSA may be attributed to the sulphonic acid loading and due to the formation of HCl as by product

during functionalization. The above results demonstrate that the Zr-TMS-BS can accommodate a maximum of 9.1 wt% of sulphonic acid at our experimental condition without destroying the mesostructure.

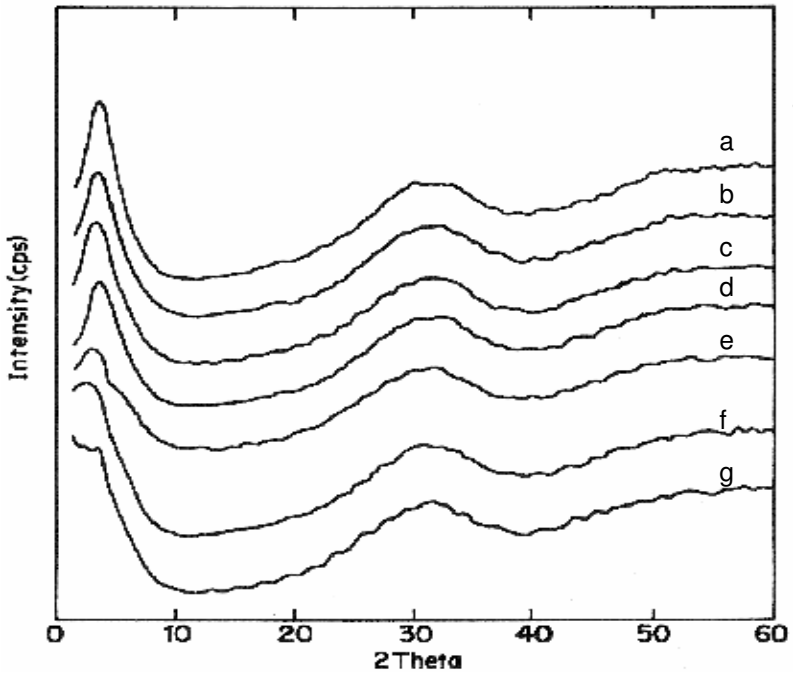

Figure 5.3. Powder XRD pattern of Zr-TMS, Zr-TMS-BS and different loadings of sulphonic acid over Zr-TMS-BS catalyst. a. Zr-TMS, b. Zr-TMS-BS, c. Zr-TMS-BSA-5, d. Zr-TMS-BSA-10, e. Zr-TMS-BSA-15, f. Zr-TMS-BSA-20, and g. Zr-TMS-BSA-25 catalysts.

5.3.5. Nitrogen adsorption-desorption study

Incorporation or anchoring of any medium (acid or base) or metal in the framework positions and/or into the walls of the supporting medium leads to a progressive decrease in surface area [44, 45]. The BET surface areas of the Zr-TMS, Zr-TMS-BS, Zr-TMS-BSA, and SO_4^{2-}/ZrO_2 are given in Table 5.1. The surface area for the Zr-TMS was 370 m^2 g^{-1}, which is comparable to that measured previously for a Zr-TMS

synthesized using a surfactant with C_{16} carbon chain [44]. The surface area gradually decreased with increasing sulphonic acid loading.

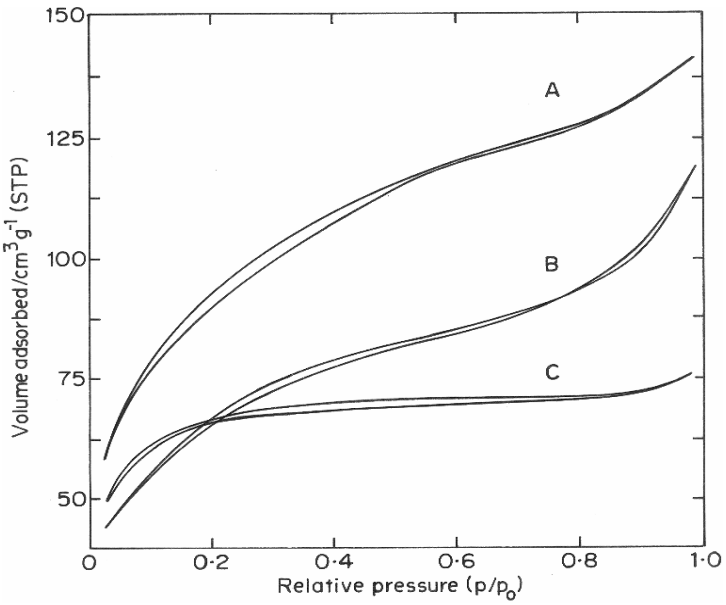

Figure 5.4. N_2 adsorption-desorption isotherms of (A) Zr-TMS, (B) Zr-TMS-BS and (C) Zr-TMS-BSA-10 samples.

Figure 5.4 A, B and C show the nitrogen adsorption-desorption isotherm of Zr-TMS, Zr-TMS-BS and Zr-TMS-BSA-10 (10 represents the input concentration of sulphonic acid over Zr-TMS-BS), respectively. All the three isotherms are of type IV characteristic of mesoporous materials. Position of inflection of Zr-TMS-BSA-10 shows that there is structure damage in the materials. However, pore size distribution analysis indicates that mesoporosity was not lost.

Figure 5.5 A, B and C shows the BJH pore size distribution curves of Zr-TMS, Zr-TMS-BS and Zr-TMS-BSA-10. The surface area, total pore volume and average pore diameter of the Zr-TMS, Zr-TMS-BS and Zr-TMS-BSA-10 were found to be 370 m^2g^{-1}, 0.31cm^3 g^{-1}, 30.9 Å; 308 cm^2g^{-1}, 0.28 cm^3g^{-1}, 26.4 Å and 198 m^2g^{-1}, 0.18cm^3 g^{-1} 18.2 Å, respectively (Table 5.1).

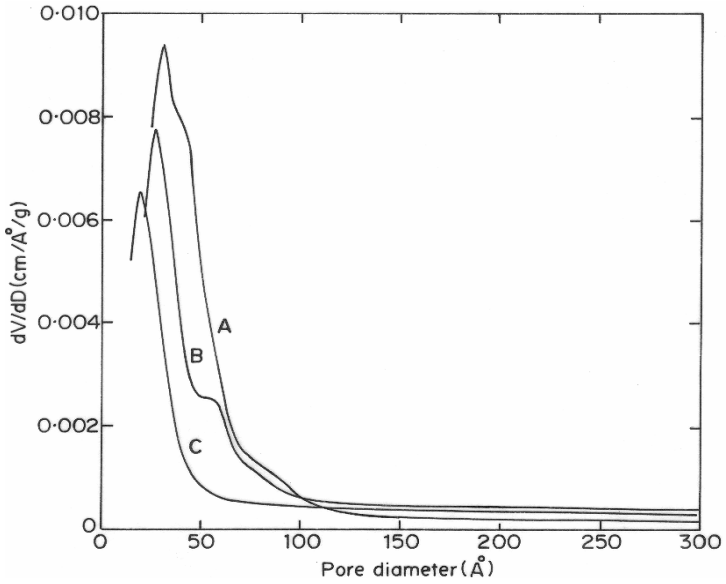

Figure 5.5. *BJH* pore size distributions of (A) Zr-TMS, (B) Zr-TMS-BS and (C) Zr-TMS-BSA-10 samples.

These results demonstrate that the surface area, pore volume and pore diameter of the functionalized materials decrease [44, 45] due to the anchoring of benzyl group over Zr-TMS and further functionalization of Zr-TMS-BS with $ClSO_3H$. The surface area, pore volume and average pore diameter of SO_4^{2-}/ZrO_2 are found to be 101 m^2g^{-1}, 0.09 cm^3g^{-1} and 9Å (Table 5.1), respectively.

5.3.6. FT-Infrared spectroscopy study

The infrared spectra of as-synthesized Zr-TMS, surfactant extracted Zr-TMS and Zr-TMS-BS is shown in Figure 5.6. In all the spectra a weak unresolved band between 900-750 cm^{-1} is attributed to Zr-O stretching vibrations [38]. A broad band between 3400 to 3650 cm^{-1} corresponds to the O-H stretching vibration in $Zr(OH)_4$ and a sharp band between 1650-1600 cm^{-1} is due to the bending vibrations of surface O-H groups and water molecules occluded in the pores [38].

In addition to the above bands, the as-synthesized Zr-TMS shows the additional weak bands at around 3200-2800 cm^{-1} and 1500-1300 cm^{-1} which are due to the C-H stretching

and bending vibrations [46] of methylene group of template material. These bands are absent in the template extracted Zr-TMS, which shows that the template removal by ethanol and HCl mixture is complete and successful. After loading of benzyl alcohol over Zr-TMS (Zr-TMS-BS or ≡ Zr-O-CH_2-Φ), the weak bands at around 3200-2800 cm^{-1} and 1500-1300 cm^{-1} are due to the C-H stretching and bending vibrations [46] of methylene group as discussed earlier and a medium band at 1423 cm^{-1} indicates the C=C stretching [46] in-plane vibration of benzene framework. A band at 707cm^{-1} represents the C-H bending vibration of methylene group of benzene [46]. A small and weak band at around 1000-1200 cm^{-1} is the characteristic band of C-O group in the catalyst.

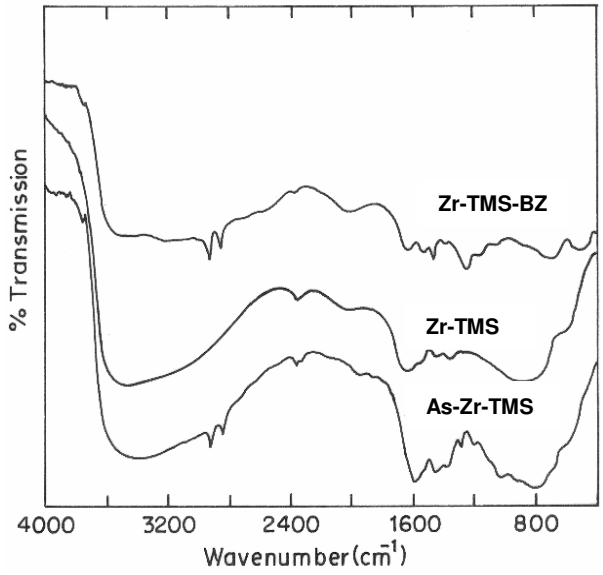

Figure 5.6. Fourier transform infrared spectrum of As-syn-Zr-TMS, surfactant extracted Zr-TMS and Zr-TMS-BS catalysts.

The FT-IR spectra of two loadings (5 and 10 wt% $ClSO_3H$) of sulphonic acid functionalized Zr-TMS-BS (Zr-TMS-BSA-5 and Zr-TMS-BSA-10) are shown in Figure 5.7. A small and intense band at 1298 cm^{-1} and the medium band at 1185 cm^{-1}, are due to S=O stretching mode of incorporated sulphonic acid [47]. The C-S link also gives a medium band between 600-700 cm^{-1} and the intensity is increased with the increase in acid loading. Further, it is noticed that the intensity of the stretching and bending modes

of –C-H group remained unchanged in Zr-TMS-BS, Zr-TMS-BSA-5 and Zr-TMS-BSA-10 with the increase in sulphonic acid loading, which shows that the attachment of $–SO_3H$ is on the benzene ring. These observations confirm the successful anchoring of benzyl group over Zr-TMS to Zr-TMS-BS and its functionalization with $ClSO_3H$ to Zr-TMS-BSA.

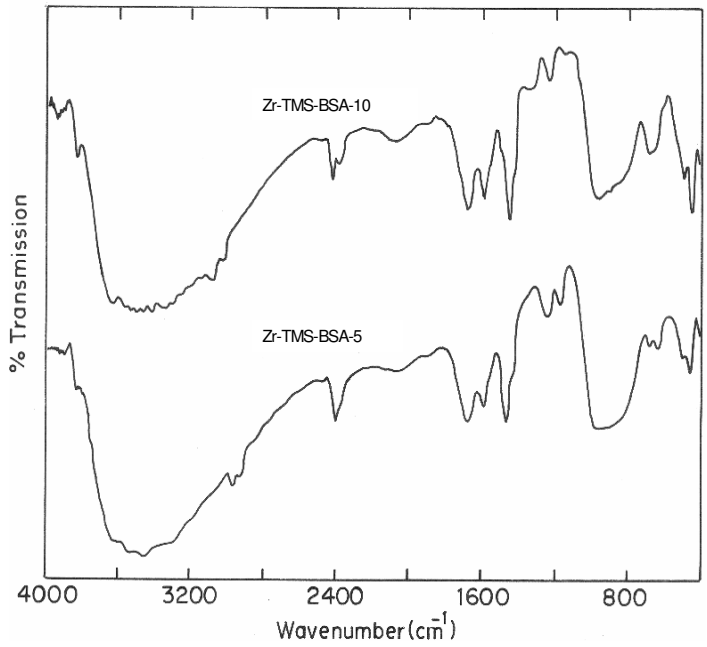

Figure 5.7. Fourier transform-infrared spectrum of Zr-TMS-BSA-5 and Zr-TMS-BSA-10 samples.

5.3.7. Ammonia adsorption-desorption study

Temperature programmed desorption (TPD) of ammonia was performed for measuring the total acidity (acid sites) of the synthesized materials [37 and references therein]. The results of the step wise desorption of ammonia of Zr-TMS, Zr-TMS-BSA, and SO_4^{2-}/ZrO_2 are presented in Table 5.1. The values of acidity for Zr-TMS and functionalized Zr-TMS were obtained by desorbing ammonia in four stages from 30 to 200 °C (between 30 – 70 °C, 70 –110 °C, 110 –150 °C and 150 – 200 °C). Since the functionalized material is covalently bonded to the solid support, it could not be treated

above 200 °C, which is evidenced by thermal analysis. Above this temperature benzyl sulphonic acid is lost from the solid support. Whereas, the adsorbed ammonia from SO_4^{2-}/ZrO_2 was desorbed in six stages between 30 and 500 °C.

The results reveal that the total acidity and the acid site distribution are dependent on the type of catalyst and are strongly influenced by the amount of sulphonic acid loading over Zr-TMS-BS. The total acidity of Zr-TMS, Zr-TMS-BSA-5, Zr-TMS-BSA-10, Zr-TMS-BSA-15, Zr-TMS-BSA-20 and Zr-TMS-BSA-25 are found to be 0.50, 0.72, 1.19, 1.22, 1.31 and 1.34 mmol g^{-1}, respectively (Table 5.1). These values are in agreement with the output of the elemental analysis result shown in Table 5.1, where the total acidity of the material is increased with respect to the loading of sulphonic acid over Zr-TMS-BS. Further, the total acidity of SO_4^{2-}/ZrO_2 was measured in six stages and found to be 1.45 mmol g^{-1}. These results demonstrate that the functionalization of benzyl group loaded Zr-TMS with sulphonic acid enhances the acidity of the material and consequently the conversion.

5.3.8. Scanning electron microscopic study

The particle size and morphology of Zr-TMS, and Zr-TMS-BSA-10 were studied by scanning electron microscopy technique. Support materials and the hydrolysis products associated with the support materials can control the morphology of mesoporous materials. The SEM micrograph of Zr-TMS (Figure 5.8A) shows clear ordered material with relatively uniform particle size (0.37μm). It is also observed that distorted hexagonal structure in the materials. Distorted, hard hexagonal and square like structure of Zr-TMS can be synthesized by using the cationic surfactant CTMABr under basic condition. The explanations are in well agreement with the earlier report for SBA-15 material [48]. It is noteworthy that previous authors have reported mesoporous zirconia to be very disordered [49], which is the case with our material also. It appears that functionalization alters the morphology and particle size of the material to a greater extent (Figure 5.8B). This decrease in ordering and crystallinity was also observed and clearly explained by XRD technique.

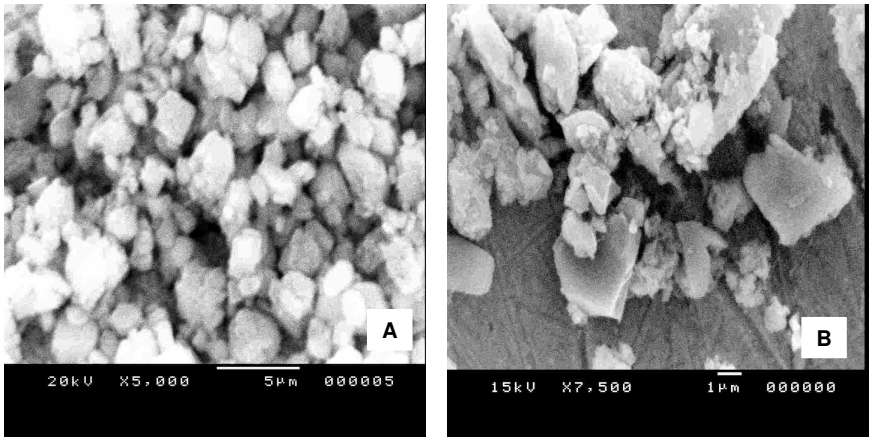

Figure 5.8. Scanning electron micrograph of (A) Zr-TMS, and (B) Zr-TMS-BSA-10 samples.

5.3.9. Transmission electron microscopic study

The samples were prepared for TEM analysis by dispersing the powder products as slurry in iso-propanol and subsequently deposited and dried on a honey carbon film on a copper grid. Transmission electron micrographs of Zr-TMS (Figure 5.9A), and Zr-TMS-BSA-10 (Figure 5.9B) reveal that these materials have a either disordered hexagonal and square planar structures.

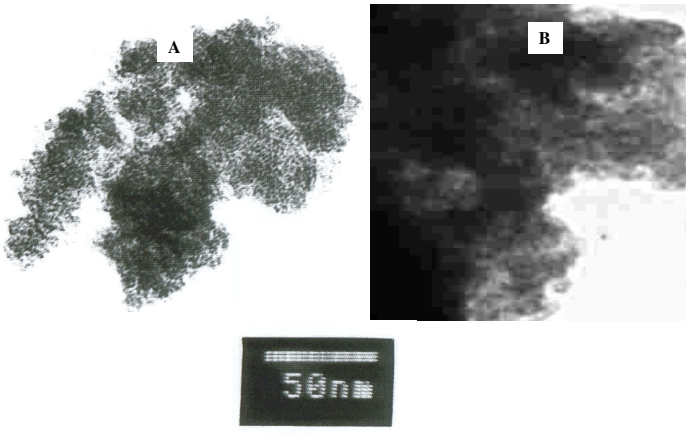

Figure 5.9. Transmission electron micrographs of (A) Zr-TMS, and (B) Zr-TMS-BSA-10 samples.

On the whole, the pores seemed to be packed together with no visible long-range order, consistent with the absence of low-angle XRD peaks. Its square like (or sponge like) pore morphology is characteristic of zirconia aerogels [14, 50]. Both Zr-TMS, and Zr-TMS-BSA-10 mesostructure contained a mixture of highly distorted hexagonal and square like regions and only the visibility of square like regions goes dark after functionalization (Figure. 5.9B).

5.4. CATALYTIC ACTIVITY

5.4.1. Pechmann condensation of resorcinol with ethyl acetoacetate

The Pechmann condensation of resorcinol (Scheme 5.2) was done with ethyl acetoacetate to 7-hydroxy-4-methylcoumarin under liquid phase condition keeping the temperature of 150 °C for 20 h of reaction time using 10 wt% benzylsulfonic acid loaded mesoporous zirconia (Zr-TMS-BSA-10) catalyst and the results are shown in Table 5.2 as fresh cycle. The conversion of resorcinol was found to be 86.2 % with product selectivity of 94.4 % to 7-hydroxy-4-methylcoumarin, which shows that the catalyst is highly protonated with mesoporosity. The rate of the resorcinol conversion (TOF, Turn Over Frequency) was calculated as the number of moles of resorcinol converted per mole of sulfur per hour and found to be 55.2×10^{-1} h^{-1}. Then the main product, 7-hydroxy-4-methylcoumarin was separated by column chromatography and analyzed by ^{1}H and ^{13}C NMR techniques. Further, the melting point and elemental analysis of the product were also measured and reported in Table 5.3 which confirms the identification of product.

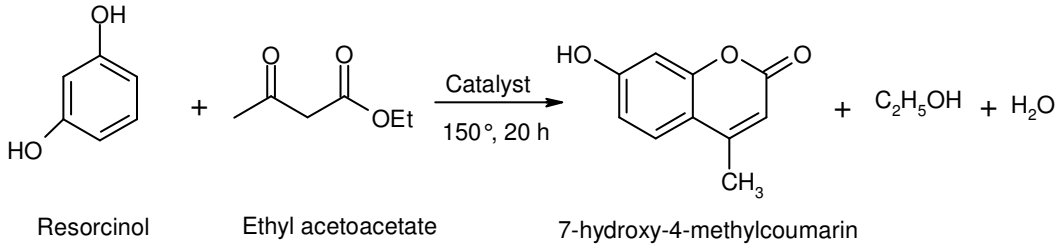

Scheme 5.2. Pechmann condensation of resorcinol with ethyl acetoacetate to 7-hydroxy-4-methylcoumarin.

5.4.2. Pechmann condensation of 3-methoxy phenol with ethyl acetoacetate

The Pechmann condensation of 3-methoxy phenol (Scheme 5.3) was done with ethyl acetoacetate to 7-methoxy-4-methylcoumarin under liquid phase condition keeping the temperature of 150 °C for 20 h of reaction time using 10 wt% benzylsulfonic acid loaded mesoporous zirconia (Zr-TMS-BSA-10) catalyst and the results are shown in Table 5.1 as fresh cycle. The conversion of 3-methoxy phenol was found to be 52.4 % with product selectivity of 90.5 % to 7-methoxy-4-methylcoumarin. The rate of the 3-methoxy phenol conversion (TOF) was found to be 33.5×10^{-1} h^{-1}. Then the main product, 7-methoxy-4-methylcoumarin was separated by column chromatography and analyzed by ^{1}H and ^{13}C NMR techniques. Further, the melting point and elemental analysis of the product were also measured and reported in Table 5.3.

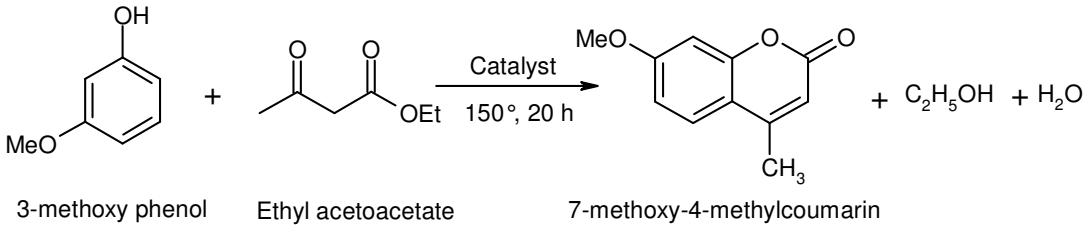

Scheme 5.3. Pechmann condensation of 2-methoxy phenol with ethyl acetoacetate to 7-methoxy-4-methylcoumarin.

5.4.3. Pechmann condensation of 1- naphthol with ethyl acetoacetate

The Pechmann condensation of 1-naphthol (Scheme 5.4) was done with ethyl acetoacetate to 7-hydroxy-4-methylcoumarin under liquid phase condition keeping the temperature of 150 °C for 20 h of reaction time using 10 wt% benzylsulfonic acid loaded mesoporous zirconia (Zr-TMS-BSA-10) catalyst and the results are shown in Table 5.2 as fresh cycle. The conversion of 1-naphthol was found to be 50.7 % with product selectivity of 96.7 % (7, 8-benzo-4-methylcoumarin). The rate of the 1-naphthol conversion (TOF) was found to be 32.5×10^{-1} h^{-1}. Then the main product, 7, 8-benzo-4-

methylcoumarin was separated by column chromatography and analyzed by ^{1}H and ^{13}C NMR techniques. Further, the melting point and elemental analysis of the product were also measured and reported in Table 5.3.

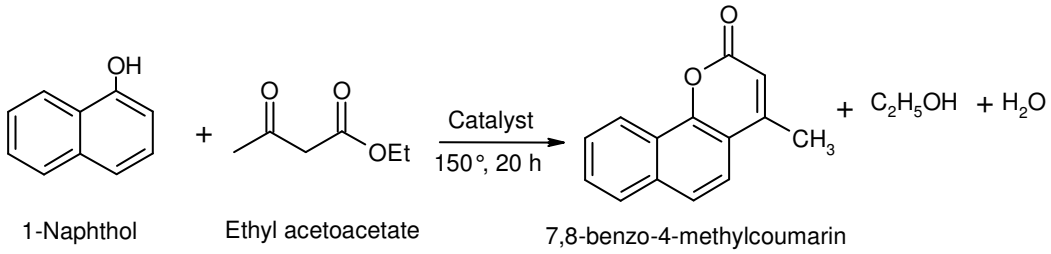

Scheme 5.4. Pechmann condensation of 1-naphthol with ethyl acetoacetate to 7, 8-benzo-4-methylcoumarin.

5.4.4. Effect of reaction temperature and reaction time

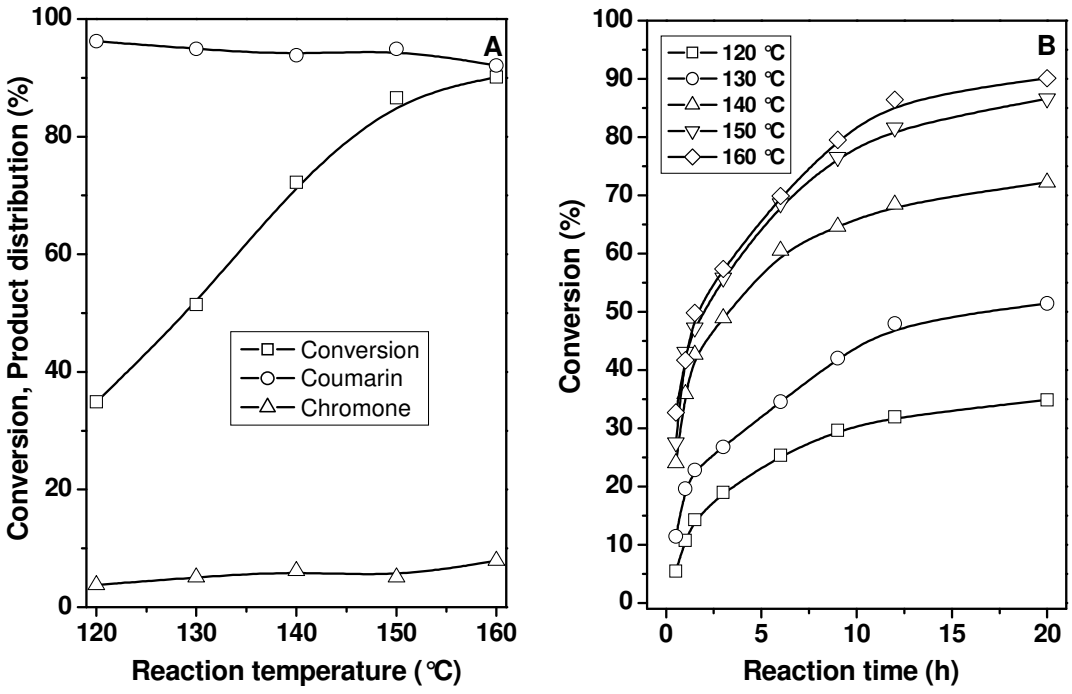

Figure 5.10. Conversion and product distribution of resorcinol over Zr-TMS-BSA-10 catalysts as a function of time and at different reaction temperatures.

The benzylsulphonic acid (BSA) functionalized Zr-TMS-BSA-10 catalyst was used to study the effect of temperature in Pechmann condensation of resorcinol to hydroxy Coumarin under solvent free condition. From Figure 5.10, it is seen that the temperature has remarkable effect for conversion of resorcinol. The conversion of resorcinol was increased with increasing temperature from 393 to 433 K, as expected. The conversion increases with increasing temperature up to 423 K, upto 12 h and then remained almost unchanged.

5.4.5. Catalyst recycles study

In order to check the stability of the catalyst the catalyst was recycled (fresh + three cycles) by using Zr-TMS-BSA-10 in the Pechmann condensation of all three aromatics. The results are presented in Table 5.2. After workup of the reaction mixture, the catalyst was separated by filtration, washed with acetone and activated for 10 h at 100 °C in the presence of air before use in the next experiment. Thus, the recovered catalyst after each reaction was characterized for its chemical composition by elemental analysis (sulfur content only given in Table 5.2, by which we calculate the total content of benzylsulfonic acid over Zr-TMS) and crystallinity by X-ray diffraction. Sulfur measured by elemental analysis showed a downward trend in the content of anchored benzylsulfonic acid of Zr-TMS-BSA-10 catalyst. Declines were observed in the conversions of resorcinol, 2-methoxy phenol and 1-naphthol from 86.2 to 57.6, 52.4 to 34.5 and 50.7 to 32.3, respectively, when the cycles goes from fresh to third recycle. However, the selectivities of all the products remained almost similar. The leaching of the benzylsulfonic acid from the Zr-TMS catalysts by side products may be attributed for the decrease in catalytic activity after every cycle.

Table 5.2. Catalytic reaction and recycle study in Pechmann condensation of aromatics.

Cycles	Condensation of resorcinol[a]				Condensation of 3-methoxy phenol[a]				Condensation of 1-naphthol[a]			
	Sulfur content (%)	**Conv. (%)**	**Selectivity (%)**	**TOF[b] (10^{-1} h^{-1})**	**Sulfur content (%)**	**Conv. (%)**	**Selectivity (%)**	**TOF[b] (10^{-1} h^{-1})**	**Sulfur content (%)**	**Conv. (%)**	**Selectivity (%)**	**TOF[b] (10^{-1} h^{-1})**
Fresh	2.5	86.2	94.9	55.2	2.5	52.4	90.5	33.5	2.5	50.7	96.7	32.5
First	2.2	69.6	96.6	50.6	2.3	47.4	92.6	32.9	2.4	48.6	93.6	32.4
Second	2.0	55.4	94.0	44.3	2.1	39.1	91.5	29.8	2.0	37.5	90.2	30.0
Third	1.9	47.6	94.3	40.1	2.0	34.5	91.7	27.6	1.9	32.3	91.5	27.2

Reaction Condition: Temperature (°C) = 150; Reaction time (h) = 20; phenol derivative (mol) = 0.01; Ethyl acetoacetate (mol) = 0.01; TOF based on

[a]Sulfur analysis was done by EA1108 Elemental Analyzer (Carlo Erba Instruments).

[b]moles of phenolic compounds converted per hour over per mol of sulfur.

Table 5.3. Identification of products by NMR[a], elemental analysis[b] and melting point[c] measurements.

Product	Chemical shift		Elemental analysis (%)			Melting Point (°C)
	^{1}H NMR	^{13}C NMR	C	H	O	
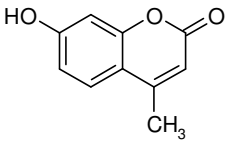 7-hydroxy-4-methylcoumarin	($CDCl_3$, 200 MHz) δ 2.39 (s, 3H), 3.28 (bs, 1H), 6.06 (s, 1H), 6.8 (s, 1H), 6.82 (d, 1H, J=8Hz), 7.44 (d, 1H, J=8Hz)	($CDCl_3$, 50 MHz) 18.5, 102.56, 110.28, 111.2, 112.79, 125.30, 152.80, 154.73, 160.84, 161.29.	68.10	4.71	26.95	185-187
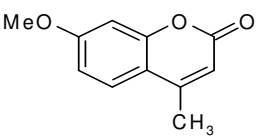 7-methoxy-4-methylcoumarin	($CDCl_3$, 200 MHz) δ 2.39 (s, 3H), 3.86 (s, 3H), 6.14 (s, 1H), 6.48 (s, 1H), 6.82 (d, 1H, J=10Hz), 7.49 (d, 1H, J=10Hz)	($CDCl_3$, 50 MHz) 18.65, 55.65, 100.73, 111.57, 112.38, 113.45, 125.49, 153.10, 155.07, 161.77, 162.66.	69.35	5.18	24.98	161-163
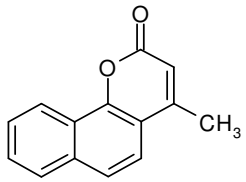 7,8-benzo-4-methylcoumarin	($CDCl_3$, 200 MHz) δ 2.49 (s, 3H), 6.34 (dd, 1H, J=2Hz), 7.53-7.69 (m, 4H), 7.8-7.89 (m, 2H)	($CDCl_3$, 50 MHz) 19.04, 114.14, 114.99, 120.14, 122.43, 123.1, 123.97, 126.94, 127.51, 128.43, 134.61, 150.36, 153.27, 160.70.	79.81	4.79	15.01	154-156

[a]Nuclear magnetic resonance analysis was done using Bruker AC200 machine.
[b]Elemental analysis of all the three products was analyzed by EA1108 Elemental Analyzer (Carlo Erba Instruments).
[c]Melting point of the products was measured by Buchi (B540) melting

5.5. CONCLUSIONS

Benzylsulfonic acid functionalized mesoporous zirconia (Zr-TMS-BSA-10) catalyst was synthesized by the previously reported literature and used in the preparation of 7-hydroxy-4-methylcoumarin, 7-methoxy-4-methylcoumarin and 7,8-benzo-4-methylcoumarin using resorcinol, 2-methoxy phenol and 1-naphthol, respectively, and found to be an efficient catalyst in the acid catalyzed condensation reactions. Further, catalyst recycle studies in all the three reactions were also proved the efficiency of the catalysts and minimum decrease in conversion can be correlated with the decrease in sulfur loading.

5.6. REFERENCES

[1] C.T. Kresge, M.E. Leonowicz, W.J. Roth, J.C. Vartuli, J.S. Beck, *Nature,* 359, **1992**, 710.

[2] F. Marlow, D. Demuth, G.D. Stucky, F, Schuth, *J. Phys. Chem.,* 99, **1995**, 1306.

[3] D.M. Antonelli, J.Y. Ying, *Angew. Chem., Int. Ed. Engl.,* 34, **1995**, 2014.

[4] H. Yoshitake, T. Sugihara, T. Tatsumi, *Chem. Mater.,* 14, **2002**, 1023.

[5] J.A. Knowles, M.J. Hudson, *J. Chem. Soc., Chem. Commun.,* **1995**, 2083.

[6] U. Ciesla, M. Froba, G.D. Stucky, K.K. Unger, F. Schuth, *Chem. Mater.,* 11, **1999,** 227.

[7] N. Ulagappan, V.N. Raju, C.N.R. Rao, *Chem. Commun.,* **1996**, 2243.

[8] B. Lee, D.L. Lu, J.N. Kondo, K. Domen, *J. Am. Chem. Soc.,* 124, **2002**, 11256.

[9] D.M. Antonelli, J.Y. Ying, *Chem. Mater.,* 8, **1996**, 874.

[10] S.A. Bagshaw, T.J. Pinnavaia, *Angew. Chem. Int. Ed. Engl.,* 35, **1996**, 1102.

[11] P. Liu, J. Liu. A. Sayari, *Chem. Commun.,* **1997**, 577.

[12] K.G. Servin, T.M. AbdeFattah, T.J. Pinnavaia, *Chem. Commun.,* **1998**, 1471.

[13] Z. Tian, W. Tong, J. Wang, N. Duan, V.V. Krishnan, S.L. Suib, *Science,* 276, **1997**, 926.

[14] M.S. Wong, J.Y. Ying, *Chem. Mater.,* 10, **1998**, 2067.

[15] Y. Inoue, H. Yamazaki, *Bull. Chem. Soc. Jpn.*, 60, **1987**, 891.

[16] A. Clearfield, *Inorg. Chem.,* 3, **1964**, 146.

[17] G.D. Yadav, J.J. Nair, *Micropor. Mesopor. Mater.,* 33, **1999**, 1.

[18] Z.R. Tian, W. Tong, J.Y. Ying, N.G. Duan, V.V. Krishnan, S. L. Suib, *Science*, 276, **1997**, 926.

[19] R.A. Boyse, E.I. Ko, *Catal. Lett.,* 38, **1996**, 225.

[20] T. Jin, T. Yamaguchi, K. Tanabe, *J. Phys. Chem.*, 90, **1986**, 4794.

[21] B.H. Davis, R.A. Keogh, R. Srinivasan, *Catal. Today,* 20, **1994**, 219.

[22] X. Song, A. Sayari, *Catal. Rev.-Sci. Eng.,* 38, **1996**, 329.

[23] Y.Y. Huang, T. J. McCarthy, W. M.H. Sachtler. *Appl. Catal. A: Gen.*, 148 **1996**, 135.

[24] F. Mohino, I. Díaz, J. P. Pariente, E. Sastre, *Stud. Surf. Sci. Catal.*, 142, **2002**, 1275.

[25] I. Díaz, F. Mohino, J. P. Pariente, E. Sastre, *Appl. Catal. A: Gen.*, 205, **2001**, 19.

[26] I. Díaz, F. Mohino, J. P. Pariente, E. Sastre, P.A. Wright, W. Zhou, *Stud. Surf. Sci. Catal.,* 135, **2001**, 1248.

[27] I. Díaz, C. M. Alvarez, F. Mohino, J. P. Pariente, E. Sastre, *J. Catal.*, 193, **2000**, 295.

[28] W.M. Van Rhijin, D.E.De Vos, B.F. Sels, W.D. Bossaert, P.A. Jacobs, *J. Chem. Soc., Chem. Commun.,* **1998**, 317.

[29] W.D. Bossaert, D.E.De Vos, W.M. Van Rhijin, J. Bullen, P.J. Grobet, P. A. Jacobs, *J. Catal.,* 182, **1999**, 156.

[30] K. Wilson, A. F. Lee, D. J. Macquarrie, J. H. Clark, *Appl. Catal A: Gen.*, 228, **2002**, 127.

[31] D. Margolese, J. A. Melero, S.C. Christiansen, B.F. Chmelka, G.D. Stucky, *Chem. Mater.,* 12, **2000**, 2448.

[32] S. Inagaki, S. Guan, T. Ohsuna, O. Terasaki, *Nature,* 416, **2002**, 304.

[33] Y. Goto, S. Inagaki. *Chem. Commun.,* **2002**, 2410.

[34] N. Bion, P. Ferreira, A. Valente, I.S. Goncalves, J. Rocha. *J. Mater. Chem.,* 13, **2003**, 1910.

[35] K. Okamoto, M.P. Kapoor, S. Inagaki, *Chem. Commun.,* **2005**, 1423.

[36] J. R. Sohn, S. G. Ryu, Y. I. Pae, S. J. Chol, *Bull. Korean Chem. Soc.*, 11 **1990**, 403.

[37] M. Chamumi, D. Brunel, F. Fajula, P. Geneste, P. Moreau, J. Solof, *Zeolites,* 14, **1994**, 283.

[38] M.J. Hudson, J.A. Knowles, *J. Mater. Chem.,* 6, **1996**, 89.

[39] G. Pacheco, E. Zhao, E.D. Valdes, A. Garcia, J.J. Fripiat, *Micropor. Mesopor. Mater.,* 32, **1999**, 175.

[40] J.L. Blin, R. Flamant, B.L. Su, *Int. J. Inorg. Mater.,* 3, **2001**, 959.

[41] G. Larsen, E. Lotero, M. Nabity, L.M. Petkovic, D.S. Shobe, *J. Catal.,* 164, **1996**, 246.

[42] E. Zhao, S.E. Hardcastle, G. Pacheco, A. Garcia, A.L. Blumenfeld, J.J. Fripiat, *Micropor. Mesopor. Mater.,* 31, **1999**, 9.

[43] U. Ciesla, S. Schacht, G.D. Stucky, K.K. Unger, F. Schuth, *Angew. Chem. Int. Ed. Engl.,* 35, **1996**, 541.

[44] A.N. Parvulescu, B.C. Gagea, M. Alifanti, V. Parvulescu, V.I. Parvulescu, S. Nae, A. Razus, G. Poncelet, P. Grange, *J. Catal.,* 202, **2001**, 319.

[45] N.C. Marziano, L.D. Ronchin, C. Tortato, A. Zingales, A.A. Sheikh-Osman, *J. Mol. Catal. A: Chem.,* 174, **2001**, 265.

[46] M. Suzuki, S. Ito, T. Kuwahara, *Bull. Chem. Soc. Jpn.,* 56, **1983**, 957.

[47] L.J. Bellamy, *Infrared spectra of complex molecules*, Chapman and Hall, **1975**.

[48] Zhao, D.; Sun, J.; Li, Q.; Stucky, G. D. *Chem. Mater,* 12, **2000**, 275.

[49] Parvulescu, V.I.; Bonnemann, H.; Parvulescu, V.; Endruschar, B.; Rufinska, A.Ch.W.; Tesche, B.; Poncelet, G. *Appl. Catal. A: Gen.,* 214, **2001**, 273.

[50] Ward, D.A.; Ko, E.I. *Chem. Mater,* 5, **1993**, 956.

CHAPTER-6

SUMMARY AND CONCLUSIONS

6.1. SUMMARY

The present thesis gives an account of (i) the syntheses of inorganic–organic hybrid mesoporous materials by immobilization of several metal complexes on organically modified M41S type molecular sieves, (ii) characterization of these composite materials, and (iii) application of these materials as catalysts in selective oxidation and condensation reactions.

The present thesis is divided into six chapters including the present one as follows:

Chapter 1 presents a general introduction about various aspects of mesoporous materials and organic-inorganic hybrid mesoporous materials. Different factors influencing their formation, synthesis mechanism, approaches for surface functionalization and commonly used characterization techniques are briefly presented. The applications of these materials for different carbon-carbon bond formation reactions are also discussed. A detailed review of the work done on the above aspect is also presented here in this chapter. Finally the scope and objectives of the present work have been outlined at the end of this chapter.

Chapter 2 provides the synthesis methodologies and characterization techniques utilized in this work.

Chapter 3 describes the synthesis of BISPICEN type chiral metal complex and their heterogenization over mesoporous MCM-41 which was modified by reactive functional group such as 3-chloropropyl trimethoxy silane. The synthesized catalysts were completely characterized by various physico-chemical techniques and the activities of the catalysts were analyzed for the sulfoxidation of thioanisole and epoxidation of styrene. The reactions were studied with different reaction parameters such as different oxidants, different reaction time and different solvents etc.

Chapter 4 deals with the synthesis of different types of metal triflate immobilized mesoporous SBA-15 materials and its characterization by various physico chemical

techniques such as PXRD, N_2-adsorption desorption, XPS, NH_3-TPD etc. The natures of acid sites present in the metal triflate immobilized SBA-15 catalysts were identified by *in situ* FT-IR spectroscopy of pyridine adsorption. The catalytic activity of the synthesized catalyst was analyzed for Friedel Crafts acylation of naphthalene with *p*-toluoyl chloride.

Chapter 5 describes the synthesis of non siliceous mesoporous Zr-TMS and its functionalization with benzyl sulphonic acid. The synthesized catalysts were characterized by various characterization techniques and activity of the catalysts was checked for Pechmann condensation reaction of ethyl acetoacetate with phenolic compounds. The reaction was studied with different reaction parameters such as different type of phenolic compounds, different reaction temperature and different time interval etc.

6.2. CONCLUSIONS

6.2.1. Metal complex immobilized MCM-41

- Highly ordered Si-MCM-41 was synthesized by hydrothermal method and the cationic surfactant was removed by calcination at 500 °C.

- Iron and ruthenium chiral metal complexes were successfully synthesized and grafted on to MCM-41 support which was modified by 3-ClPTMS.

- The powder XRD pattern of the synthesized catalysts shows the mesoporous nature of the material. The lack of higher order reflection peak indicates the reduction in the ordering of the mesoporous channels. This result was further supported by N_2 sorption isotherm analysis results of the catalyst.

- Solid state ^{13}C CP MAS NMR spectra and FT-IR spectra of the catalysts confirm proper grafting of the metal complex inside the mesoporous material.

- The UV-Vis and XPS spectrum of the synthesized catalysts shows +2 oxidation state for Ru and +2 as well as +3 oxidation state for Fe complex.

- The screening of the catalysts, Ru/Fe-L_2Me-MCM-41, was done in the sulfoxidation reaction of thioanisole and epoxidation of styrene using different oxidants such as H_2O_2, TBHP, PhIO.

- The catalytic results indicate that the heterogenised chiral metal complexes (Ru/Fe-L_2Me-MCM-41) play an important role in the sulfoxidation of thioanisole, which give higher activity, TON and comparable enantiomeric excess compared to the homogeneous catalyst.

- Recycling studies show that chiral metal complex only partially leaches out during the reaction which indicates that the grafting procedure of the metal complexes over Cl-MCM-41 is effective in meeting the objectives.

6.2.2. Metal triflate immobilized SBA-15

- Metal triflate loaded SBA-15 was synthesized by wet impregnation method and maximum loading of triflate groups was optimized to be 30 mol % without destroying the mesophases.

- The powder XRD pattern of the synthesized catalyst shows a progressive decrease in the intensity which reveals partial loss of long-range order of SBA-15 due to the incorporation of triflate molecules. This result was further supported by the N_2 adsorption desorption isotherm.

- The NH_3-TPD of the catalyst shows at least three distinct ammonia adsorption sites for these catalysts. Further the acid strength distribution depends strongly on the cation associated with triflate molecules.

- The *insitu pyridine* IR results reveal that large triflate groups may assist in the geometric confinement within the pores of the mesoporous SBA-15, the metal cations are basically responsible for the direct binding of the reactant molecules and hence for the catalytic properties.
- We surmise from *pyridine* IR results that the confinement of a large molecule such as metal triflate may cause significant physical perturbation to the surface hydroxyl groups of the host matrix and this in turn may give rise to the formation of certain Bronsted type surface acid sites.

- The screening of the catalysts was done in the Friedel Crafts acylation of naphthalene with *p*-toluoyl chloride. The increase in the conversion was observed with increase in triflate loading (up to 30 mol %). More conversion of naphthalene was observed with zinc triflate catalyst and this may be because of more Lewis acid sites. The B/L ratio follows a trend La (9.5) > Y (4.7) > Ce (3.0) > Zn (0.3) and this matches well with the catalytic activity results.

6.2.3. Benzyl sulphonic acid functionalized Zr-TMS

- Zr-TMS has been synthesized with high surface area and functionalized with benzyl sulphonic acid using post synthetic route by applying the etherification and subsequent sulfonation reactions to get covalently bonded Zr-TMS-BSA catalyst.

- Different amounts of sulphonic acid (5, 10, 15, 20 and 25 wt %) were loaded over Zr-TMS-BS and the maximum amount of sulphonic acid loading was optimized to 9.1 wt % (input 10 wt %) without destroying the mesoporous structure.

- The powder XRD patterns and the N_2 adsorption-desorption confirm the mesoporous nature of the material with high surface area and considerable pore size distributions in agreement with conventional mesoporous ZrO_2.

- The FT-IR study revealed the successful anchoring of benzyl group and the subsequent functionalization of $–SO_3H$ group and the NH_3 TPD measurements showed that the catalysts are acidic in nature.

- The catalysts optimization study for different reaction parameters was done on the liquid phase Pechmann condensation of phenol with ethyl acetoacetate to Coumarin at 150 °C. Pure mesoporous Zr-TMS support is poorly active for this reaction because of the lower acidic nature.

- Zr-TMS-BSA-10 was recycled two times and minimum decrease in conversion of phenolic compound can be correlated to a minor leaching of benzyl sulphonic acid from the catalyst. The higher activity and selectivity of the synthesized catalysts may be attributed to its higher acidity and mesoporous characteristics.

LIST OF PUBLICATIONS

[1] Liquid phase condensation of anisole with p-formaldehyde over benzylsulfonic acid functionalized mesoporous Zr-TMS catalyst.

M. Chidambaram, **S. Selvakumar,** T. Tamil Selvi and A.P. Singh.

J. Molecular Catalysis A: Chemical, 245 (**2006**) 69-77.

[2] Ru- and Fe-based N, N'-bis(2-pyridylmethyl)-N-methyl-(1S, 2S)-1,2-cyclohexanediamine complexes immobilized on mesoporous MCM-41: Synthesis, characterization and catalytic applications.

T. Soundiressane, **S. Selvakumar**, S. Menage, O.Hamelin, M. Fontecave and A. P. Singh.

J. Molecular Catalysis A: Chemical, 270 (**2007**) 132-143.

[3] Benzylsulfonic acid functionalized mesoporous Zr-TMS catalysts: Yet another efficient and recyclable catalyst for the preparation of Coumarin derivatives by Pechmann condensation reaction.

S. Selvakumar, M. Chidambaram and A.P. Singh.

Catalysis Communications, 8 (**2007**) 777-783.

[4] Benzoylation of anisole over silicotungstic acid modified mesoporous alumina.

S. Selvakumar and A. P. Singh.

Catalysis Letters, 128 (**2009**) 363–372.

[5] Nature of the acid sites in the metal triflates immobilized in SBA-15 and their role in the Friedel–Crafts acylation of naphthalene.

S. Selvakumar, N.M. Gupta and A. P. Singh.

Applied Catalysis A: General, 372 (**2010**) 130-137.

[6] Vice to Virtue: Intracellular Biogenic Nanoparticles for the Generation of Carbon Supported Catalysts.

P. S. Vijayakumar, **S. Selvakumar,** R. S. Gholap, A.P. Singh, and B. L. V. Prasad. Journal of Nanoscience and *Nanotechnology,* 10 (**2010**) 905-911.

CONTRIBUTIONS TO NATIONAL/INTERNATIONAL SYMPOSIA/CONFERENCES

[1] *Benzoylation of toluene with p-toluoyl chloride over triflic acid functionalized mesoporous Zr-TMS catalyst.*

M. Chidambaram, S. Parambadath, **S. Selvakumar** and A.P. Singh.

17th National symposium on catalysis held on January 2005 at CSMCRI, Bhavnagar, India. *(Oral presentation)*

[2] *Synthesis, characterization and catalytic applications of amine based chiral complexes immobilised mesoporous MCM-41.*

T. Soundiressane, **S. Selvakumar,** S. Ménage, O. Hamelin, M. Fontecave and A.P. Singh.

18th National Symposium & Indo-US Seminar on Catalysis held on April 16-18, 2007 at IIP, Dehradun, India. (Oral Presentation).

[3] *Metal triflate modified mesoporous catalysts for Friedel Crafts acylation reaction.*

S. Selvakumar, N.M. Gupta and A.P. Singh.

19th National symposium on catalysis held on January 2009 at NCL, Pune, India. (Poster presentation).